

AD A117672

AFWAL-TR-82-2029

RESEARCH ON SOURCES OF GAS PHASE
METASTABLE ATOMS AND MOLECULES

R. C. Slater, H. A. Hyman, D. Trainor, and A. Flusberg
AVCO EVERETT RESEARCH LABORATORY, INC.
a Subsidiary of Avco Corporation
Everett, MA 02149



May 1982

Final Technical Report for Period 15 August 1979 - 15 February 1982

APPROVED FOR PUBLIC RELEASE; DISTRIBUTION UNLIMITED.

DTIC FILE COPY

AERO PROPULSION LABORATORY
AIR FORCE SYSTEMS COMMAND
UNITED STATES AIR FORCE
WRIGHT-PATTERSON AIR FORCE BASE, OHIO 45433

BEST
AVAILABLE COPY

DTIC
ELECTE
AUG 03 1982
S E D

82 08 02 160

ASD 82 1391

NOTICE

When Government drawings, specifications, or other data are used for any purpose other than in connection with a definitely related Government procurement operation, the United States Government thereby incurs no responsibility nor any obligation whatsoever; and the fact that the government may have formulated, furnished, or in any way supplied the said drawings, specifications, or other data, is not to be regarded by implication or otherwise as in any manner licensing the holder or any other person or corporation, or conveying any rights or permission to manufacture use, or sell any patented invention that may in any way be related thereto.

This report has been reviewed by the Office of Public Affairs (ASD/PA) and is releasable to the National Technical Information Service (NTIS). At NTIS, it will be available to the general public, including foreign nations.

This technical report has been reviewed and is approved for publication.

PROJECT ENGINEER

DONALD P. MORTEL
Chief, Energy Conversion Branch
Aerospace Power Division
Aero Propulsion Laboratory

FOR THE COMMANDER

JAMES D. REAMS
Chief, Aerospace Power Division
Aero Propulsion Laboratory

"If your address has changed, if you wish to be removed from our mailing list, or if the addressee is no longer employed by your organization please notify AFWAL/POOC-3, W-PAFB, OH 45433 to help us maintain a current mailing list".

Copies of this report should not be returned unless return is required by security considerations, contractual obligations, or notice on a specific document.

UNCLASSIFIED

SECURITY CLASSIFICATION OF THIS PAGE (When Data Entered)

REPORT DOCUMENTATION PAGE		READ INSTRUCTIONS BEFORE COMPLETING FORM
1. REPORT NUMBER AFWAL-TR-82-2029	2. GOVT ACCESSION NO. AD-A117672	3. RECIPIENT'S CATALOG NUMBER
4. TITLE (and Subtitle) RESEARCH ON SOURCES OF GAS PHASE METASTABLE ATOMS AND MOLECULES		5. TYPE OF REPORT & PERIOD COVERED Final Technical Report 8/15/79 - 2/15/82
7. AUTHOR(s) R.C. Slater, H.A. Hyman, D. Trainor, and A. Flusberg		6. PERFORMING ORG. REPORT NUMBER
9. PERFORMING ORGANIZATION NAME AND ADDRESS Avco Everett Research Laboratory, Inc. 2385 Revere Beach Parkway Everett, MA 02149		8. CONTRACT OR GRANT NUMBER(s) F33615-79-C-2051
11. CONTROLLING OFFICE NAME AND ADDRESS Aero Propulsion Laboratory (AFWAL/Pooc) AF Wright Aeronautical Laboratories, AFSC Wright-Patterson AFB, Ohio 45433		10. PROGRAM ELEMENT, PROJECT, TASK AREA & WORK UNIT NUMBERS
14. MONITORING AGENCY NAME & ADDRESS (if different from Controlling Office)		12. REPORT DATE May 1982
		13. NUMBER OF PAGES 132
		15. SECURITY CLASS. (of this report) Unclassified
		15a. DECLASSIFICATION/DOWNGRADING SCHEDULE
16. DISTRIBUTION STATEMENT (of this Report) Approved for public release; distribution unlimited.		
17. DISTRIBUTION STATEMENT (of the abstract entered in Block 20, if different from Report)		
18. SUPPLEMENTARY NOTES		
19. KEY WORDS (Continue on reverse side if necessary and identify by block number) rare gas metastable atoms discharges metastable molecules optical excitation metastable sources optical storage		
20. ABSTRACT (Continue on reverse side if necessary and identify by block number) This study is concerned with the development of new types of sources for the production of metastable atoms and molecules. In the context of the present study, the term metastable means any excited atomic or molecular species with a relatively long radiative lifetime ($\tau \geq 1 \mu\text{sec}$). Several separate tasks were undertaken under this program. The literature was searched, and a review of radiative lifetimes and radiative decay mechanisms was compiled for a representative number of atomic and molecular		

DD FORM 1473

JAN 73

EDITION OF 1 NOV 65 IS OBSOLETE

UNCLASSIFIED

SECURITY CLASSIFICATION OF THIS PAGE (When Data Entered)

UNCLASSIFIED


SECURITY CLASSIFICATION OF THIS PAGE(When Data Entered)

systems of interest to such diverse areas as gas discharge physics, chemical physics, flame chemistry and plasma physics.

A second task involved a literature review of prior basic research metastable sources followed by the development and experimental testing of appropriate candidate sources for the production of rare gas atomic and molecular metastable species. The results of this literature review suggested that a low pressure, high current discharge technique previously investigated for the production of alkaline earth metastable atoms would also be appropriate for this phase of the program. The operation of this type of metastable source was investigated and tested for the production of metastable argon, krypton and nitrogen. Quantitative results for argon indicate generation of $10^{15} - 10^{16}$ metastables $\text{cm}^{-2} \text{sec}^{-1} \text{steradian}^{-1}$.

Four methods for producing high fluxes of metastable atoms and molecules were investigated theoretically and modeled. The methods included: excitation of H_2 vibrational states by stimulated Raman scattering, two-color optical excitation of $\text{Xe}(^3\text{P}_2)$ and $\text{Kr}(^3\text{P}_2)$, $\text{N}_2(\text{A})$ state production by e-beam sustained discharge excitation of N_2 and production of helium metastable atoms via electron-ion recombination in the afterglow of a magnetic annular arc is also described.

Methods for the storage of metastables for times up to the radiative lifetime were also investigated. A preliminary discussion of an optical trap technique is described.



UNCLASSIFIED

SECURITY CLASSIFICATION OF THIS PAGE(When Data Entered)

PREFACE

This study was performed by the Avco Everett Research Laboratory, Inc. under contract F33615-79-C-2051 and funded by the Air Force Wright Aeronautical Laboratory. The Air Force program manager was Dr. Alan Garscadden, Energy Conversion Branch, Aero Propulsion Laboratory, Wright-Patterson AFB.

Accession For		
NTIS GRA&I	<input checked="" type="checkbox"/>	
DTIC TAB	<input type="checkbox"/>	
Unannounced	<input type="checkbox"/>	
Justification		
By		
Distribution/		
Availability Codes		
Avail and/or		
Dist	Special	
A		



TABLE OF CONTENTS

<u>Section</u>	<u>Page</u>
Preface	iii
List of Illustrations	vii
I. INTRODUCTION	1
II. LITERATURE SURVEY OF RADIATIVE LIFETIMES	2
III. DEVELOPMENT OF A BASIC RESEARCH SOURCE OF METASTABLE ATOMS AND MOLECULES	8
A. INTRODUCTION	8
B. METASTABLE SOURCES REVIEW	9
1. Atomic Metastable Production via Ion Impact on Surfaces	9
2. Charge Exchange Method	10
3. Optical Pumping of Metastable Calcium Atoms	14
4. Production of $O_2(^1\Delta_g)$ via Chemical and Photo-lytic Methods	15
5. Low Pressure, High Current Discharge	16
C. APPARATUS	18
D. DIAGNOSTICS AND RESULTS	27
1. Discharge Diagnostics	27
2. Detector Diagnostics	27
3. Results	30
E. RECAP OF SOURCE AND DETECTOR OPERATING CONDITIONS	37
F. PROPOSAL FOR MEASUREMENT OF ABSOLUTE METASTABLE DENSITY	38
IV. METHODS FOR PRODUCING HIGH THROUGHPUT SOURCES OF METASTABLE ATOMS AND MOLECULES	40
A. STIMULATED RAMAN SCATTERING PRODUCTION OF $H_2(v=1)$ AND $N_2(v=1)$	42
1. Introduction and Background	42
2. Proposed Experimental Setup and Predicted Yields	48
3. System Parameters (Using H_2 as an Example)	54
4. Limiting Assumptions	57
5. Other Applications	59

<u>Section</u>	<u>Page</u>
B. OPTICAL PUMPING METHODS FOR THE PRODUCTION OF HIGH DENSITY, HIGH-SELECTIVITY METASTABLE SOURCES	60
1. Introduction	60
2. Results and Discussion	62
3. Conclusions	69
4. Other Methods for Generating Vacuum Ultraviolet (VUV) Radiation	70
5. Calculation of Required VUV Fluence and IR Flux	76
C. E-BEAM-SUSTAINED DISCHARGE EXCITATION OF METASTABLE $N_2(A^3\Sigma_u^+)$	78
1. Overview of Modeling Calculation	79
2. Boltzmann Code Calculation	79
3. Kinetic Model	87
4. Results	96
5. Effects on N_2 Gas Density, Initial Gas Temperature and Added Species	107
6. Extraction of Metastable $N_2(A)$ from the Discharge Zone	108
D. METASTABLE PRODUCTION FROM A MAGNETIC ANNULAR ARC	111
V. STORAGE OF METASTABLES	120

LIST OF ILLUSTRATIONS

<u>Figure</u>		<u>Page</u>
1	Energy Level Diagram for Charge Exchange into Excited States	11
2	Conceptual Design for a Charge Exchange Metastable Source	13
3	Photograph of Pumping System and Vacuum Chamber	19
4	Schematic of Pumping System and Vacuum Chamber	20
5	Photograph of Discharge Source	21
6	Schematic Layout of Discharge Source and Detector	22
7	Photograph of Detectors	24
8	Schematic of Auger Detector and Operating Circuit	25
9	Schulz-Phelps Calibration Curve	26
10	I-V Characteristic of Discharge Source in the Absence of Ionization	28
11	Discharge Current as a Function of Nozzle Source Pressure	29
12	Auger Current as a Function of Attractor Grid Bias	31
13	Auger Current as a Function of Nozzle Source Pressure	32
14	Auger Current as a Function of Discharge Voltage	35
15	Kr, Ar and N ₂ Metastable Signals as a Function of Discharge Current	36
16	Stimulated Raman Scattering (SRS)	43
17	Pressure Effect of H ₂ Raman Linewidth	44
18	First Stokes Gain for Forward SRS in H ₂	46
19	Experimental Setup for H ₂ SRS	50
20	H ₂ [*] and N ₂ [*] Production as a Function of Laser Beam Waist	52

<u>Figure</u>		<u>Page</u>
21	Experimentally Derived Rate Constants, $k_{10}(M)$ as a Function of Temperature T for Deactivation of H_2 by Various Collision Partners M	56
22	Energy Level Diagram and Processes Relevant to Model Calculation of $Xe(^3P_2^0)$ Generation	61
23	Schematic Layout of Optical Excitation Source	63
24	Model Calculation of $Xe(^3P_2^0)$ Production as a Function of Laser Intensity	68
25	Generation of a Pulsed Beam of Metastable Xe Atoms Using Four-Wave Mixing in Mg Vapor	71
26	Energy Levels of Atomic Mg Relevant to Four-Wave Mixing VUV Generation	72
27	Energy Levels of Atomic Xe Relevant to Metastable (State M) Generation	74
28	Dotted Curves are Electron Energy Distributions as Calculated by the Boltzmann Code: $E/N = 4.1 \times 10^{-16} \text{ V-cm}^2$ (Curve A); $E/N = 1.02 \times 10^{-15} \text{ V-cm}^2$ (Curve B)	83
29	Fractional Energy Deposition in N_2 at 1 atm and 298°K vs E/N	85
30	The ratio, R , vs E/N for N_2 at 1 atm and 298°K	86
31	The results of the $N_2(A)$ kinetics code at $J_{eb} = 10^{-5} \text{ A/cm}^2$, $E/N = 4.1 \times 10^{-16} \text{ V-cm}^2$, $T = 298^\circ\text{K}$ and 1 atm N_2	98
32	The results of the $N_2(A)$ Kinetics Code at $J_{eb} = 10^{-3} \text{ A/cm}^2$, $E/N = 1.02 \times 10^{-15} \text{ V-cm}^2$, $T = 298^\circ\text{K}$ at 1 atm N_2	99
33	The results of the $N_2(A)$ Kinetics Code at $J_{eb} = 10^{-3} \text{ A/cm}^2$, $E/N = 4.1 \times 10^{-16} \text{ V-cm}^2$, $T = 298^\circ\text{K}$ and 1 atm N_2	100
34	The results of the $N_2(A)$ kinetics code at $J_{eb} = 10^{-3} \text{ A/cm}^2$, $E/N = 1.02 \times 10^{-15} \text{ V-cm}^2$, $T = 298^\circ\text{K}$ and 1 atm N_2	101
35	The results of the $N_2(A)$ Kinetics Code at $J_{eb} = 10^{-1} \text{ A/cm}^2$, $E/N = 4.13 \times 10^{-16} \text{ V-cm}^2$, $T = 298^\circ\text{K}$ and 1 atm N_2	102
36	The results of the $N_2(A)$ Kinetics Code at $J_{eb} = 10^{-1} \text{ A/cm}^2$, $E/N = 1.02 \times 10^{-15} \text{ V-cm}^2$, $T = 298^\circ\text{K}$ and 1 atm N_2	103

<u>Figure</u>		<u>Page</u>
37	Schematic Diagram of E-Beam Sustained Discharge Flow System for $N_2(A)$ Production	109
38	Schematic Diagram of Electron-Ion Recombination Source	114
39	Geometry of Ashkin's Optical Trap (Ref. 126)	121
40	Energy Levels of an Atom Confined to an Optical Trap	122
41	(a) An Atom Moves to the Right at Velocity v Along the Direction of Propagation of One of a Pair of Counter-Propagating Light Beams of Frequency ω . (b) Viewed in the Atomic Rest Frame, the Right-Going Beam Appears Downshifted, and the Left-Going Upshifted in Frequency	123
42	(a) Energy Levels of an Atom of Interest, Showing the Ground State g , Metastable State m , and Excited State e (b) Energy Levels of He Corresponding to those of (a)	125

I. INTRODUCTION

This report describes both theoretical and experimental studies into methods for producing and storing metastable atoms and molecules, i.e., species with relatively long radiative (usually dipole forbidden) lifetimes. The motivation for the present study is due, in part, to the need to improve the state of the art in metastable production techniques. Specifically, there is a desire to increase both the absolute density and metastable fractional composition of these sources. To date, there has been little effort specifically directed towards these particular goals. Any method which accomplishes one and/or both of these goals will provide an important experimental tool that can be used to improve the data base of the fundamental properties of metastable atoms and molecules, e.g., rate constants, collisional and excitation cross sections, and lifetimes. The accurate evaluation of these quantities is needed to understand the detailed behavior of a diversity of plasma, discharge, flame and other equilibrium and nonequilibrium situations in which processes involving metastable atoms and molecules play an important role.

This report is composed of several separate parts. Section II is a literature search and compilation of radiative lifetimes of some representative metastable atoms and molecules. Dominant radiative decay mechanisms for these states are also reported in Section II. Section III is devoted to a brief review of some metastable production techniques, and an experimental study of a simple, basic research source that can be used to produce metastable rare gas atoms and metastable nitrogen molecules. Section IV describes novel techniques for producing a high flux and/or high purity source of metastable species. As far as we know, none of these techniques have been experimentally verified although the calculations contained herein suggest improvements in flux and purity of (for some cases) many orders of magnitude. Finally, some initial thoughts on the difficult problem of metastable storage techniques are described in Section V.

II. LITERATURE SURVEY OF RADIATIVE LIFETIMES

A literature search was undertaken to compile radiative lifetimes and, in many cases, radiative decay mechanisms (electric dipole, etc.) for metastable states (i.e., states with radiative lifetimes $\geq 1 \mu\text{s}$) in a number of atomic and molecular systems. The candidate species were chosen solely on the basis of their being representative of systems that are extensively studied in atomic and molecular physics. The results of this phase of the program are reported in Table 1. The first column in the table identifies the species of interest, the second column designates the particular metastable level, the third column designates the energy of that level, the fourth column indicates the range of measured or calculated lifetimes for that level, the fifth column indicates the principal radiative decay mechanism (not necessarily to the ground state) and the last column is the literature citation.

No attempt has been made here at either a complete or critical review of all lifetime data. Only a limited number of the known metastable states for each species was included although we obtained as much data as possible for each candidate state. In some cases we have taken the liberty of deleting lifetime values when it is apparent that the literature suggests this value is in error. In a number of other cases, unresolved controversies still exist. In those cases, we have listed all the reported lifetime values in order to give an estimate of the precision of each lifetime value.

TABLE 1

RADIATIVE LIFETIMES AND DECAY MECHANISMS FOR A NUMBER OF METASTABLE ATOMS AND MOLECULES

SPECIES	METASTABLE STATE	EXCITATION ENERGY (eV)	τ (sec)	PRINCIPAL DECAY MECHANISM	REFS.
He	$1s2s\ ^3S_1$	19.82	7.9×10^3	M1	1
	$1s2s\ ^1S_0$	20.61	2.0×10^{-2}	2-PHOTON	2
Ne	$2p^5 3s\ ^3P_2^0$	16.62	2.4×10^1	M2	3
	$3p^0$	16.71	4.3×10^2	M1	3
			$(> 8 \times 10^{-1})(a)$		4
Ar	$3p^5 4s\ ^3P_2^0$	11.55	5.6×10^1	M2	3
	$3p^0$	11.72	4.5×10^1	M1	3
			$(> 1.3)(a)$		4
Kr	$4p^5 5s\ ^3P_2^0$	9.913	8.5×10^1	M2	3
	$3p^0$	10.56	4.9×10^{-1}	M1	3
			$(> 1.0)(a)$		4
Xe	$5p^5 6s\ ^3P_2^0$	8.314	1.5×10^2	M2	3
	$3p^0$	9.446	7.8×10^{-2}	M1	3

TABLE 1 (Continued)

SPECIES	METASTABLE STATE	EXCITATION ENERGY (eV)	τ (sec)	PRINCIPAL DECAY MECHANISM	REFS.
Mg	$3s3p \ ^3p_0^0$	2.709	2.4×10^4	E1(NP) (b)	5
	$3p_1^0$	2.711	4.5×10^{-3}	E1(SO)	6
	$3p_2^0$	2.716	5.6×10^3	M2	7
Hg	$6s6p \ ^3p_0^0$	4.667	5.6	E1(NP) (b)	5
	$3p_2^0$	5.460	6.9×10^{-1}	M1, E1(NP) (b)	8,5
Pb	$6p^2 \ ^3p_1$	0.9693	1.4×10^{-1}	M1	9
	$3p_2$	1.320	2.6	M1, E2	9
	$1d_2$	2.660	3.7×10^{-2}	M1	9
	$1s_0$	3.653	1.1×10^{-2}	M1	9
N ₂	$A^3\Sigma_u^+$	6.17	1.3, 2.7	E1(SO)	10
N ₂	$a'^1\Sigma_u^-$	8.4	$\sim 0.7, 0.013$ (c)	E1(RM) (d)	11,19
N ₂	$a^1\Pi_g$	8.55	$(80-170) \times 10^{-6}$	M1, E2	12-17
N ₂	$E^3\Sigma_g^+$	11.87	$(160-370) \times 10^{-6}$		15,18
O ₂	$a^1\Delta_g$	0.98	$2.7 \times 10^3, 6 \times 10^3$	M1(SO)	20,21,21a,29
O ₂	$b^1\Sigma_g^+$	1.63	7 - 12	M1(SO)	22-26

TABLE 1 (Continued)

<u>SPECIES</u>	<u>METASTABLE STATE</u>	<u>EXCITATION ENERGY (eV)</u>	<u>τ(sec)</u>	<u>PRINCIPAL DECAY MECHANISM</u>	<u>REFS.</u>
O ₂	A ³ Σ_u^+	4.39	0.03	E1(S0)(e)	27
H ₂	1 ¹ $\Sigma_g^+(v=1)$	0.52	(3.8-12.5) $\times 10^6$	E2	28
NO	a ⁴ Π	4.7	≥ 0.16		29
NO	A ² Σ^+	5.5	1.96-4.5 $\times 10^{-7}$; 2 $\times 10^{-6}$ (g)		29,29a-29d
NO	B ² Π	5.6	3.6 $\times 10^{-6}$; 1.2 $\times 10^{-5}$ (g)		29,29b
CO	a ³ Π	6.3	(3-450) $\times 10^{-3}$ (f)	E1(S0)	30,31

NOTES:

- (a) ³P_{2,0} composite state
 (b) natural isotopic abundance ratios
 (c) v=0 lifetime
 (d) RM = rotational mixing with ¹ Π_u state
 (e) likely, but not definitive
 (f) rotational state dependent

SYMBOLS:

- E1 electric dipole
 E2 electric quadrupole
 M1 magnetic dipole
 M2 magnetic quadrupole
 S0 induced by spin-orbit interaction
 NP induced by nuclear perturbation
 (hyperfine interaction) in the
 odd isotopes

TABLE 1.

1. Drake, G.W.F., Phys. Rev. A3, 908 (1971).
2. Rundel, R.D. and Stebbings, R.F., Case Studies in At. Coll. Phys. 2 ed. E.W. McDaniel and M.R.C. McDowell (North-Holland Publishing Co., Amsterdam, 1972), p. 550.
3. Small-Warren, N.E. and Chiu, L.Y.C., Phys. Rev. A11, 1777 (1975).
4. van Dyck, Jr., R.S., Johnson, C.E. and Shugart, H.A., Phys. Rev. A5, 991 (1972).
5. Garstang, R.H., J. Opt. Soc. Amer. 52, 845 (1962).
6. Furcinitti, P.S., Wright, J.J. and Balling, L.C., Phys. Rev. A12, 1123 (1975).
7. Garstang, R.H., Astrophys. J. 148, 579 (1967).
8. Hyman, H.A. (unpublished).
9. Garstang, R.H., J. Res. NBS 68A, 61 (1964).
10. Shemansky, D., J. Chem. Phys. 51, 689 (1969); Zipf, E.C., Can. J. Chem. 47, 1863 (1969); Shemansky, D., and Carleton, N.P., J. Chem. Phys. 51, 682 (1969).
11. Tilford, S.G., Wilkinson, P.G. and Vanderslice, J.T., Astrophys. J. 141, 427 (1965).
12. Shemansky, D.E., J. Chem. Phys. 51, 5487 (1969).
13. Lichten, W., J. Chem. Phys. 26, 306 (1957).
14. Olmstead III, J., Newton, A.S. and Street, Jr., K., J. Chem. Phys. 42, 2321 (1965).
15. Borst, W.L. and Zipf, E.C., Phys. Rev. A3, 979 (1971).
16. Kaslow, D.E., Ph.D. Thesis, Univ. of Michigan, Ann Arbor, Mich. (1971).
17. Holland, R.F., J. Chem. Phys. 51, 3940 (1969).
18. Freund, R.S., J. Chem. Phys. 50, 3734 (1969).

19. Tilford, S.G. and Benesch, W.M., J. Chem. Phys. 64, 3371 (1976).
20. Badger, R.M., Wright, A.C., Whitlock, R.F., J. Chem. Phys. 43, 4345 (1965).
21. Nicholls, R.W., Can. J. Chem. 47, 1847 (1969).
- 21a. Vallance-Jones, A. and Gattinger, R.L., Planet. Space Sci. 11, 961 (1963).
22. Wallace, L. and Huntten, D.M., J. Geophys. Res. 73, 4813 (1968).
23. Allen, C.W., Astrophys. J. 85, 156 (1937).
24. van de Hulst, H.C., Ann. Astrophys. 8, 12 (1945).
25. Childs, W.H.J. and Mecke, R., Z. Physik 68, 344 (1931).
26. de Jager, C., Bull. Astron. Inst. Neth. 13, 9 (1956).
27. Jarmain, W.R. and Nicholls, R.W., Proc. Phys. Soc. 90, 545 (1967).
28. James, H.M. and Coolidge A.S., Astrophys. J. 87, 438 (1938).
29. Nicholls, R.W., Ann. Geophys. 20, 144 (1964).
- 29a. Bubert, H. and Froben, F.W., Chem. Phys. Lett. 8, 242 (1971).
- 29b. Jeunehomme, M., J. Chem. Phys. 45, 4433 (1966).
- 29c. Jeunehomme, M. and Duncan, A.B.F., J. Chem. Phys. 41, 1692 (1964).
- 29d. Fink, E.H. and Welge, K.H., Z. Naturforsch 23a, 358 (1968).
30. Johnson, C.E. and van Dyck, Jr., R.S., J. Chem. Phys. 56, 1506 (1972).
31. James, T.C., J. Chem. Phys. 55, 4118 (1971).

III. DEVELOPMENT OF A BASIC RESEARCH SOURCE OF METASTABLE ATOMS AND MOLECULES

A. INTRODUCTION

The objective of this experimental phase of the program is the development of techniques for producing sources of metastable atomic and molecular beams that can generate metastable species at densities $\geq 10^8 \text{ cm}^{-3}$. In particular, there is an interest in sources for rare gas electronic metastable atoms and metastable vibrational or low lying electronic states in molecules. It is also desired that the fraction of metastable species relative to the total beam content be as large as possible. The relatively large absolute density and high fractional purity are desirable characteristics for enhancing the signal-to-noise ratio in various types of metastable beam scattering experiments. These experiments are usually difficult even when both collision partners are in the ground state. Low beam densities and concomitant low signal levels are required for producing the well-collimated beams needed for making angular measurements. The level of experimental difficulty is then further increased when information on excited state-ground state or excited state-excited state collision cross sections is desired. Nevertheless, this information is of fundamental importance for understanding the properties of excited states of atoms and molecules, and the development of methods to increase the data base in this area should be pursued.

During the initial phase of the program, it was decided that a single candidate technique that could generate both rare gas atomic and molecular metastable states would be sought in order to satisfy both the technical requirements and the scope of the program. This strategy has, however, prevented us from investigating some interesting but untested concepts which might greatly improve the state of the art in metastable sources. Of special note is the optical pumping method for the production of low lying metastable levels in the heavier rare gas atoms (see Section IV). This technique is believed capable of producing metastable fractional excitation ≥ 10 percent

but was not considered as a candidate method because of its complexity and inability to produce molecular metastables in its present embodiment. The choice of supersonic nozzle sources was also discounted due to the limited pumping speed of the available vacuum system.

B. METASTABLE SOURCES REVIEW

We briefly review a few of the metastable production concepts that were considered for this phase of the program. Section III-B-5 reviews the method of choice, namely, a low pressure, high current discharge source. A description of the experimental arrangement of the discharge source, associated diagnostics and results follows in Section III-C and III-D.

1. Atomic Metastable Production via Ion Impact on Surfaces

Experiments performed several years ago⁽³²⁾ demonstrated that when energetic helium positive ions collide with a metal surface, metastable states of the neutral parent species are produced. Subsequently, this technique was employed for producing beams of metastable inert gas atoms for studies of secondary electron emission produced by metastable atom impact on solid metal targets. The more recent⁽³³⁾ of these publications appeared in 1950, the original observations were published in 1929.⁽³²⁾ Little or no quantitative information describing the metastable beam densities and fractional population ratios was available from these publications since the main thrust of the work dealt with the energy distribution of the secondary electron ejected from the metal surface and hence this information was not critical to the needs of the experiments.

Hagstrum⁽³⁴⁾ has reported the reflection coefficients (or probability) for producing metastable atoms via rare gas ion impact on surfaces as a function of incident ion energy. A total of five surfaces were investigated: tungsten, molybdenum, silicon (100), hafnium and germanium (111). The results of this work indicate that : (1) the reflection coefficient increases rapidly with ion energy; (2) the magnitude of the reflection coefficient as a function of velocity is independent of the mass or nature of the ion (He^+ , Ar^+ ,

32. Oliphant, M.L.E., Proc. Roy. Soc. A124, 288 (1929).

33. Green, D. Phys. Rev., 876 (1950).

34. Hagstrum, H.D., Phys. Rev. 123, 758 (1961).

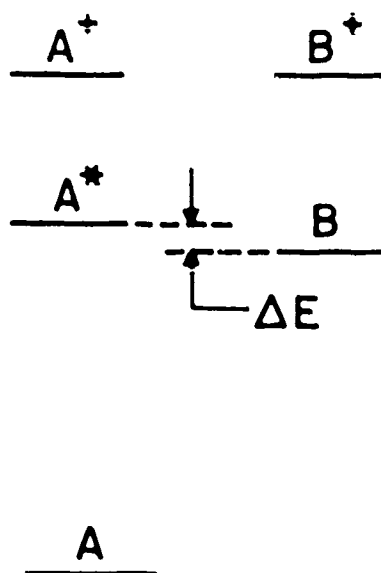
Ne⁺); and (3) the magnitude of the reflection coefficient depends upon the cleanliness of the surface. For atomically clean tungsten and molybdenum, the reflection coefficient increases from about 10^{-3} at 100 eV to ~ 0.04 at 10^3 eV. For atomically clean silicon, the values are about two to ten times higher. Much larger values have been observed for contaminated germanium and hafnium surfaces for which the reflection coefficient approaches 0.1 at 1000 eV.

In order to take advantage of the surface conversion of ions to metastables, a glancing incident collision is required in order to remove the metastable from the proximity of the surface and thus prevent re-ionization of the metastable. This application was reported in a post-deadline paper at the Paris ICPEAC Conference⁽³⁵⁾ which described an experimental measurement of electron impact excitation cross sections on metastable helium atoms produced by neutralization of positive ions on a graphite surface. Ion optics were used to focus the ions from a Penning ion source through an orifice drilled in the graphite plate. Few other experimental details were available although metastable helium densities of 10^{10} cm^{-3} were quoted and cross-section measurements were presented establishing the utility of this technique. Although our follow-up inquiries to the Russian authors requesting technical details has met with no response, we believe that a quantitative reinvestigation of this technique is required to validate the quoted metastable production especially at low translation ion energy.

2. Charge Exchange Method

The basic idea is to utilize the fact that the charge-transfer cross section becomes very large ($\geq 50 \text{ \AA}^2$) for a near resonant process. If one can therefore identify charge-transfer partners in which capture into an excited, metastable state is near-resonant, one can hope to selectively produce a large density of metastable atoms. The physical principle behind the method is illustrated by the energy-level diagram in Figure 1. This figure shows the case where the energy defect (ΔE) relative to excited-state A* is much smaller than that relative to the ground state A. Under such circumstances, one would expect the reaction

35. Kakhaev, A.D., Gostev, V.A., Saitsev, Yu.V., International Conference on the Physics of Electronic and Atomic Collisions, Paris, (1977).



G5707

Figure 1 Energy Level Diagram for Charge Exchange into Excited States



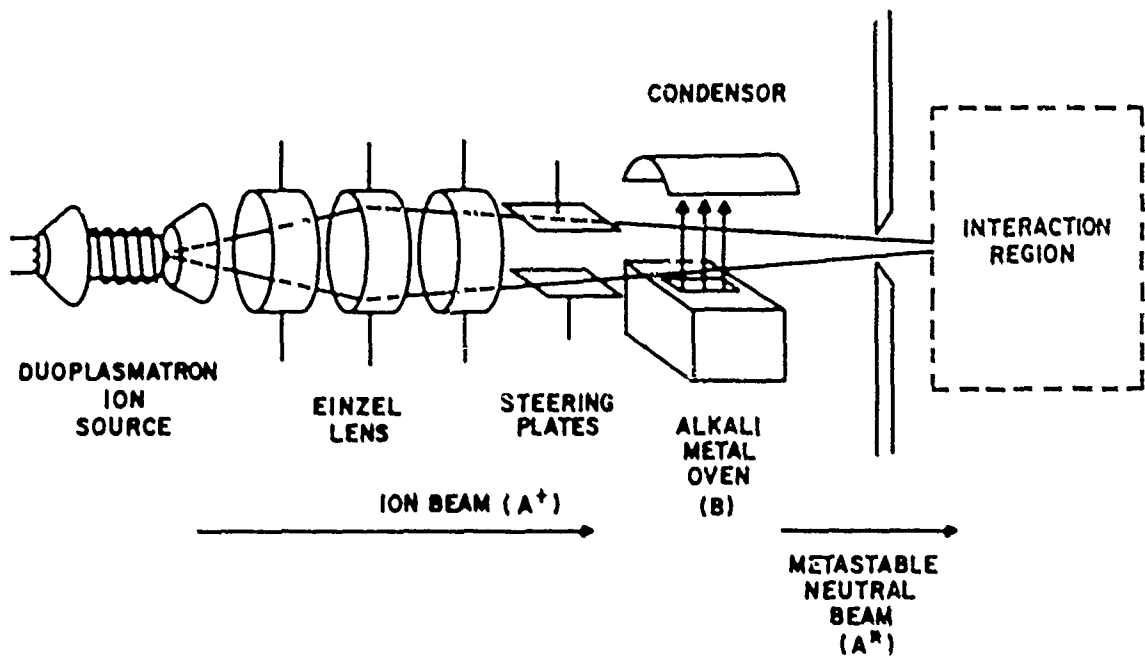
to be the dominant charge-transfer process. The situation shown schematically in Figure 1 is typical of rare gas ion-alkali atom pairs. Total cross sections for He^+ and Ar^+ ions charge-transferring to K, Rb and Cs atoms have been measured by Peterson and Lorents.⁽³⁶⁾ They found cross sections $\geq 50 \text{ \AA}^2$, and although they did not attempt to directly detect excited species, they concluded that such large total cross sections could only be compatible with electron capture into excited states of He and Ar. Their conclusions were subsequently supported by the theoretical results of Ice and Olson,⁽³⁷⁾ who noted in addition that the combinations $\text{Kr}^+ + \text{Rb}$, and $\text{Xe}^+ + \text{Cs}$ should favor production of metastable states of Kr and Xe. Finally, Neynaber and Magnuson⁽³⁸⁾ directly measured the composition of He, Ne, and Ar beams resulting from the rare gas ion-alkali atom charge transfer process, and found that ≥ 50 percent of the rare gas atoms were in excited metastable states.

A conceptual design for a charge transfer source is shown in Figure 2. The duoplasmatron is a dc arc-discharge source, yielding a high-intensity ($\sim 1 \text{ mA}$), space-charge-limited beam of positive ions in the kilovolt energy range. The electrostatic Einzel lens is a focusing device, which can produce a focused beam of ions $\sim 0.1 \text{ cm}$ in diameter over a large range of distances. The beam would be focused in the interaction region (where, for example, electron-metastable excitation or ionization experiments could be carried out), which would be separated from the ion source chamber by a small aperture and by differential pumping. Steering plates would permit precise alignment of the beam. Prior to entering the interaction region, the ion beam would transverse a well-defined perpendicular source of appropriate alkali vapor, effusing from a narrow slit in the heated oven. The perpendicular geometry minimizes the amount of alkali vapor component in the main beam.

36. Peterson, J.R., and Lorents, D.C., Phys. Rev. 182, 152 (1969).

37. Ice, G.E., and Olson, R.E., Phys. Rev. A11, 111 (1975).

38. Neynaber, R.H., and Magnuson, G.D., J. Chem. Phys. 65, 5239 (1976).



65658

Figure 2 Conceptual Design for a Charge Exchange Metastable Source

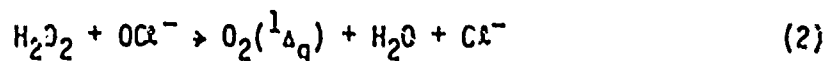
The charge exchange technique has several advantages compared with other conventional methods. Remote positioning of the source is possible, since the beam can be focused as required. Since the cross sections are very large, conditions in the oven can be conveniently arranged to guarantee essentially complete neutrality of the emerging beam. Furthermore, the beam will contain ~ 50 percent metastable atoms, whereas for conventional methods the ratio of metastables to ground-state atoms is $\sim 10^{-5} - 10^{-4}$. Finally, the absolute number density of metastables attainable with such a source is estimated to be $\sim 10^{10} \text{ cm}^{-3}$. The charge-transfer technique for producing metastables should certainly be useful for all of the rare gases and perhaps also for other species for which the appropriate charge-exchange partners can be found.

3. Optical Pumping of Metastable Calcium Atoms

The production of the lowest lying metastable triplet level in calcium, $4s4p \ ^3P_1$ at 1.88 eV, has been accomplished by direct optical excitation of the intercombination line ($4s^2 \ ^1S_0 \rightarrow 4s4p \ ^3P_1$) at 6572.8 Å using a tuned dye laser to excite calcium in an oven at $\sim 1100^\circ\text{K}$.⁽³⁹⁾ The oscillator strength of this transition is large enough that a significant fraction of the ground state population can be pumped into the metastable level during the intense dye laser pulse (fluence = 10 mJ/cm^2 ; pulse width = 30 ns). The calcium density was controlled by varying the oven temperature. At low optical depths corresponding to calcium densities of the order of $3 \times 10^{13} \text{ cm}^{-3}$ to $5 \times 10^{14} \text{ cm}^{-3}$, the authors report about 50 percent of the atoms excited in a cylinder volume (1 cm^2 by 10 cm long). At high optical depths, $\sim 10^{16} \text{ cm}^{-3}$ calcium atoms, the absolute density of excited atoms can be obtained from a measurement of the laser energy since the number of photons in the laser beam is much less than the number of calcium atoms in the line of sight. From the measured laser energy ($\sim 7 \text{ mJ}$), a measurement of the line width of the intercombination line ($\sim 0.15 \text{ Å}$) and a measurement of the laser line width ($\sim 0.5 \text{ Å}$), the authors obtain an absolute metastable density of $\sim 10^{15} \text{ cm}^{-3}$ under these conditions.

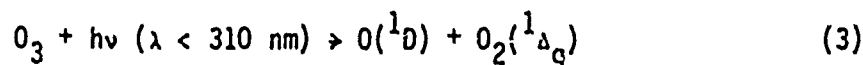
39. McIlrath, T.J., and Carlsten, J.C., J. Phys. B6, 697 (1973).

4. Production of $O_2(^1\Delta_g)$ via Chemical and Photolytic Methods
 Solution phase reactions of the type:



have long been known to produce the metastable oxygen molecule $O_2(^1\Delta_g)$. The mechanism was originally elucidated by Kasha and co-workers.⁽⁴⁰⁾ Recently, this reaction has been used to provide a chemical pumping mechanism for the O_2/I chemical iodine laser. Measurements of the absolute $O_2(^1\Delta_g)$ and $O_2(^3\Sigma_g^-)$ ground state density generated in the reaction of alkaline H_2O_2 and OCl^- were performed in order to determine whether sufficient excited oxygen is produced to produce iodine atom lasing.⁽⁴¹⁾ All species concentrations were obtained by an electron paramagnetic resonance technique using ground state O_2 as a calibrant and calculated matrix elements to determine the relative signal strengths of the other species. At the highest Cl_2 flow rate used, $13 \text{ cm}^3/\text{sec}$, about 10 percent of the oxygen is produced in the $^1\Delta_g$ state. The absolute metastable density was reported to be $\sim 10^{15} \text{ cm}^{-3}$. The 90 percent of the O_2 produced in the ground state was attributed to the base catalyzed decomposition of H_2O_2 .

Another unique $O_2(^1\Delta_g)$ production technique utilizes photolysis of O_3 below about 310 nm via the process:



which has an energetic threshold near 310 nm. The relative quantum yield for $O(^1D)$ production has been measured to be 1.0 ± 0.1 in the region 250-290 nm.⁽⁴²⁾ The absolute quantum efficiency for $O(^1D)$ production has been measured

40. Kahn, A.U., and Kasha, M., J. Amer. Chem. Soc. 92, 3293 (1970).

41. McDermott, W.E., Lotz, R.W., Delong, M.L., and Thomas, D.M., "Chemical Generation of $O_2(^1\Delta_g)$ ".

42. Fairchild, P.W., and Lee, E.K.C., Chem. Phys. Lett. 60, 36 (1978).

to be 1.0 at 253.7 nm for O_3 immersed in liquid Ar.⁽⁴³⁾ We are not aware of quantum yield measurements for $O_2(^1\Delta_g)$ production. However, we would expect a significant $O_2(^1\Delta_g)$ production via KrF ($\lambda = 249$ nm) laser photolysis of O_3 assuming that the quantum yields of $O(^1D)$ and $O_2(^1\Delta_g)$ are similar. The O_3 absorption coefficient is about 10^{-17} cm² at its peak near 249 nm. This value implies that a laser fluence of the order of 0.1 J/cm² would be required to insure a high photolysis probability per incident photon. A total of $\sim 10^{17}$ $O_2(^1\Delta_g)$ could be generated using a 100 mJ KrF laser pulse. Both the fluence and laser power are readily attainable using commercial KrF lasers.

5. Low Pressure, High Current Discharge

After reviewing a number of possible alternatives, it was decided that a low pressure, high current discharge of the type originally described by several groups^(44,45) was the method of choice for the experimental program described below. These reports indicate that metastable beams of alkaline earth atoms, e.g., $Ca(^3P_{0,1,2})$, $Ca(^1D_2)$, $Mg(^3P_{0,1,2})$ and $Ba(^3D_{1,2,3})$, can be produced with fractional excitation levels approaching 30 percent using high discharge current fluxes of the order of 1 A/cm² and low atomic vapor pressures, $\approx 2 \times 10^{-4}$ torr, where the source is operating under effusive conditions. The low voltage (~ 100 V), high current discharge was obtained by accelerating thermionically generated electrons in front of the exit orifice of a resistively heated oven containing the appropriate alkaline earth atomic vapor.

Although a detailed model of the source operation is not available, there are several qualitative aspects which suggest that this source may also be applied to the production of metastable species of interest here. First, the high current flux is necessary in order to obtain high metastable production rates via direct electron impact excitation of ground state species:



43. DeMore, W.B., and Raper, O.F., J. Chem. Phys. 44, 1780 (1966).

44. Brinkmann, U., Goschler, J., Steudel, A., and Walther, H., Zeits. fur Physik 228, 427 (1969); Brinkmann, U., Steudel, and H. Walther, Z. Angew. Phys. 22, 223 (1967).

45. Ishii, S., and Ohlendorf, W., Rev. Sci. Inst. 43, 1632 (1972).

where e_s denotes a discharge electron; M and M^* denote, respectively, the ground and metastable levels; and the energy threshold of this process is given by $E(e_s') - E(e_s)$. The M^* production rate is linear in discharge electron density up until M^* loss processes become important at high M^* density at which point the M^* density begins to level off. Second, a low atomic beam density is necessary to minimize heavy particle-metastable loss processes. Also, if the atomic beam density is low, the electron energy loss can be made small enough so that the electron average energy is directly determined by the applied field strength.

In order to obtain a high electron current, some fraction of the atomic beam must be ionized to neutralize the negative space charge which tends to limit the amount of electron current that can be drawn from an electron source. For plane parallel geometry, this limit is given by the Child-Langmuir law:⁽⁴⁶⁾

$$J_{\max} = 2.33 \times 10^{-6} \frac{V^{3/2}}{d^2} \text{ amp/cm}^2 \quad (5)$$

where J_{\max} is the maximum electron current flux which can be drawn across a region of space bounded by two electrodes having a voltage difference V between them and spaced d centimeters apart. This is about the limiting current that has been observed in space-charge limited electron bombardment metastable sources.⁽⁴⁷⁻⁴⁹⁾ For typical cases: $d = 1$ cm, $V = 30$ volts, $J_{\max} \approx 385 \text{ } \mu\text{amps/cm}^2$ and the maximum electron density, $n_e^M, \sim 10^7 \text{ cm}^{-3}$ assuming an average electron energy equals 30 eV. This value of n_e^M is smaller than that achievable with partial space charge neutralization.

46. Spangenberg, K.R., Vacuum Tubes (McGraw-Hill Book Co., N.Y.) p. 171 (1948).

47. Collins, R., Aubrey, B., Eisner, P., and Celotta, R., Rev. Sci. Inst. 41, 1403 (1970).

48. Freund, R.S., Rev. Sci. Inst. 41, 1213 (1970).

49. Shaw, H.J., "Atomic and Electron Physics - Part A: Atomic Sources and Detectors," Hughes, V.W., and Schultz, H.L. ed. in Vol 4 of Methods of Experimental Physics, Academic Press, p. 96 (1967).

The requirements of high electron current (density) and low neutral beam density cannot be achieved simultaneously under all conditions. On the one hand, the neutral beam density must be high enough to maintain a sufficient ionization rate needed for charge neutralization. On the other hand, the neutral beam density should be low enough to minimize heavy particle metastable quenching. In addition to beam density, the voltage across the discharge is another parameter which must be optimized. Metastable excitation cross sections typically peak at much lower energies than ionization cross sections implying that the ion production rate may not maximize at the same applied voltage for which the metastable production rate maximizes. In the studies described below we have investigated the performance of the high current discharge source as a function of discharge current, voltage and source pressure in order to optimize the metastable output for argon, krypton and N_2 beams.

C. APPARATUS

The experiment was housed within a differentially pumped stainless steel vacuum apparatus shown in Figure 3. The metastable source and detection system were each located in separate sections of the apparatus and communicate with each other via a 0.038 cm diameter orifice (see Figure 4). Each section is pumped by a 6 in. oil diffusion pump and can attain $\sim 10^{-8}$ torr ultimate vacuum. The quoted net pumping speed of the diffusion pump, gate valve and liquid nitrogen trap combination stack is about 800 l/sec (air).

The discharge source was located in the source chamber (Figure 4) and was comprised of a pair of stainless steel bias plates, a quartz nozzle gas source and a heated thoria coated iridium filament. A picture of the discharge source is shown in Figure 5 and a schematic of the discharge source and detector is shown in Figure 6. The gas nozzle source was made by heating 6 mm quartz tubing to white heat and then drawing the tubing apart until a thin (0.018 cm diameter) capillary was formed. Separate dc power supplies were used to supply heater power to the filament and the bias voltage across the plates number 1 and number 2. The filament was maintained at ground potential as was plate number 1.

Metastables created in the discharge source exit through the 0.038 cm diameter orifice that was drilled into the chamber bulkhead and enter a detector chamber where they are monitored by an Auger detector. A calibrated

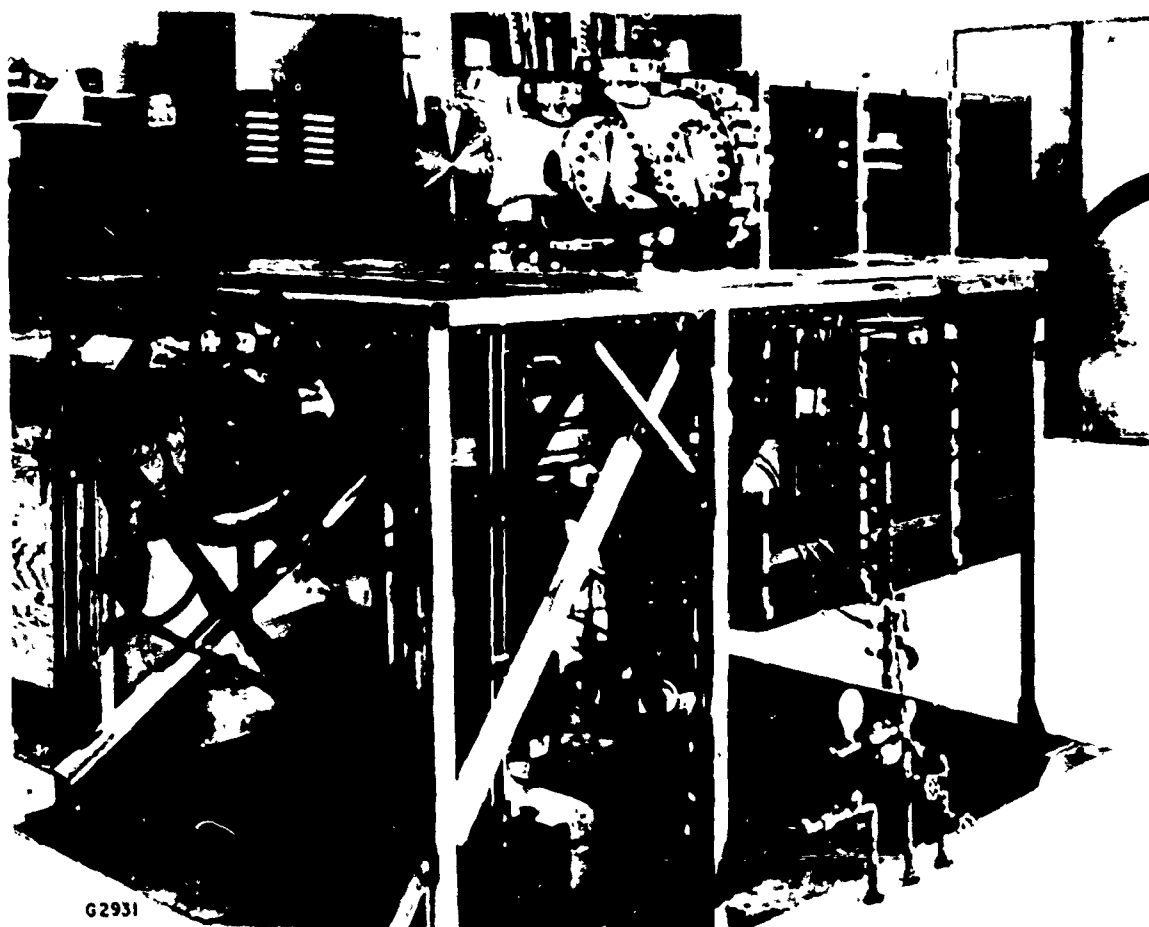
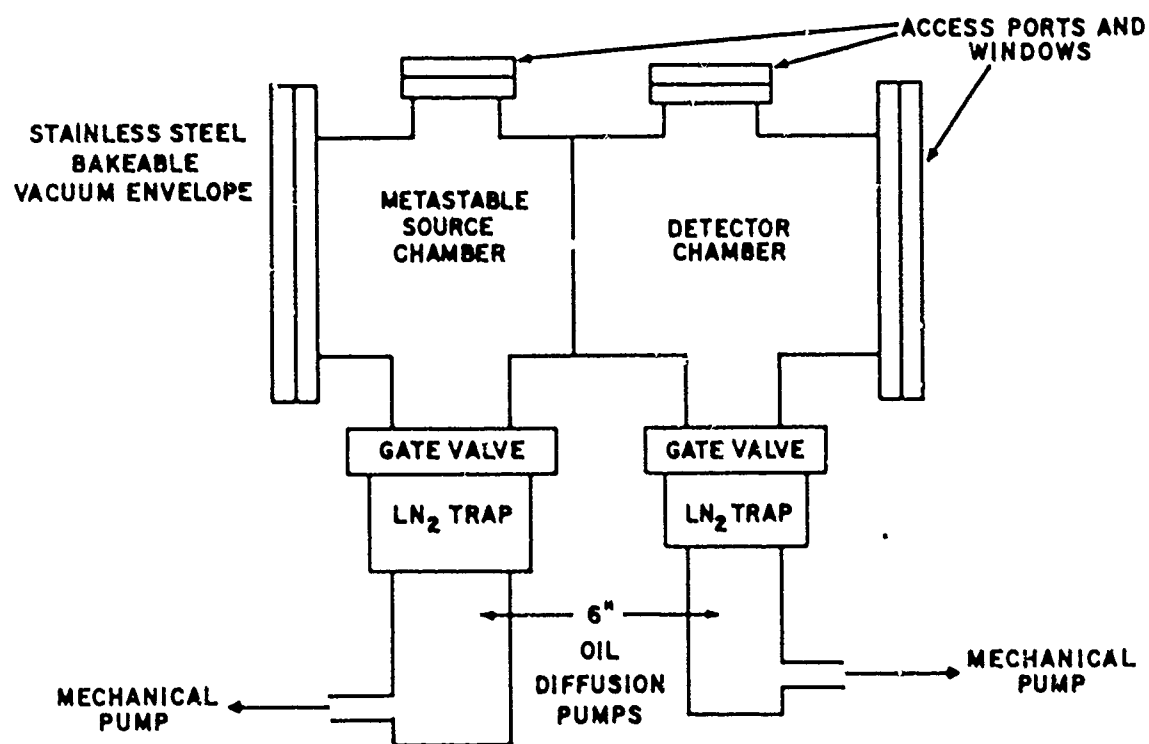


Figure 3 Photograph of Pumping System and Vacuum Chamber

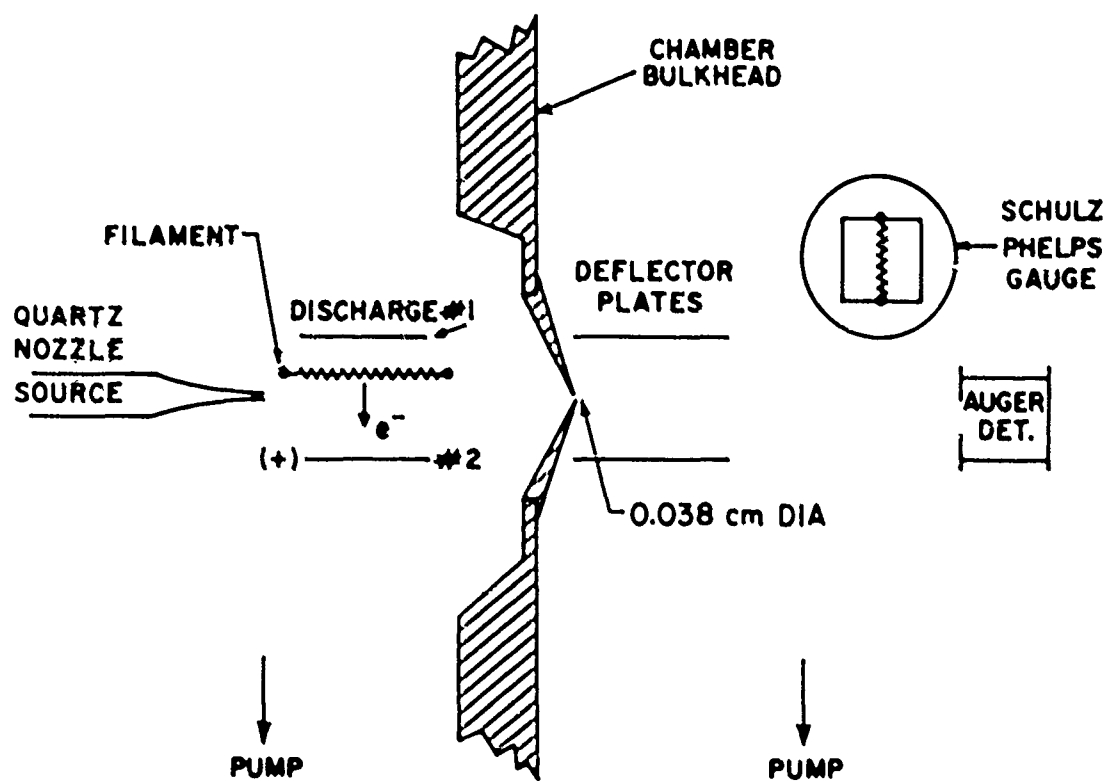


E7789

Figure 4 Schematic of Pumping System and Vacuum Chamber



Figure 5 Photograph of Discharge Source



K3721

Figure 6 Schematic Layout of Discharge Source and Detector

Schulz-Phelps type ionization gauge was used to monitor the total beam density in the detector chamber. Deflector plates attached to the chamber bulkhead were used to remove charged particles from the beam, and a capillary tubing used for injecting scattering gas was interposed between the deflector plates and Auger detector. Provision was also made for a LiF beam flag which could be positioned in front of the Auger detector. The Auger detector, ionization gauge and gas cell were all mounted on a translation stage that provided motion perpendicular to the beam axis so that either the Auger or the ionization detector could be positioned on the beam line. A picture of the detectors is shown in Figure 7.

A schematic diagram of the Auger detector and the associated biasing circuit is shown in Figure 8. The Auger plate is made of pure molybdenum with a 0.05 cm gold overcoat to provide an inert surface. Metastables incident on the gold surface will eject electrons if the metastable energy is greater than the work function of gold (4.3 eV). The highly transparent attractor grid is biased positively with respect to the Auger plate so that the ejected Auger electrons are completely removed from the plate resulting in a positive current monitored by a high sensitivity electrometer. The guard plates insure that leakage currents between the various elements of the Auger stack are minimized. This is essential for the measurement of the low metastable currents that were obtained in these experiments.

The Schulz-Phelps ionization gauge calibration was verified by filling the detector chamber with argon gas and comparing the ionization gauge measurements with that of an absolute reading McLeod gauge. The results of this calibration are shown in Figure 9. The ionization gauge measurements were obtained by scaling the ionization gauge output reading by the factor 1/1.29, which accounts for the difference in the ionization efficiency of argon and nitrogen. The calibration points are indicated by the solid dots, and the solid line with unity slope indicates what perfect agreement would look like. The ion gauge readings are reasonably accurate down to about 10^{-4} torr, the lowest pressure that the McLeod gauge can measure. Based upon the scatter about the solid line, the ion gauge readings are probably correct to better than a factor of two in this pressure range. However, under the operating conditions of the present experiments, pressures in the 10^{-5} - 10^{-6} torr

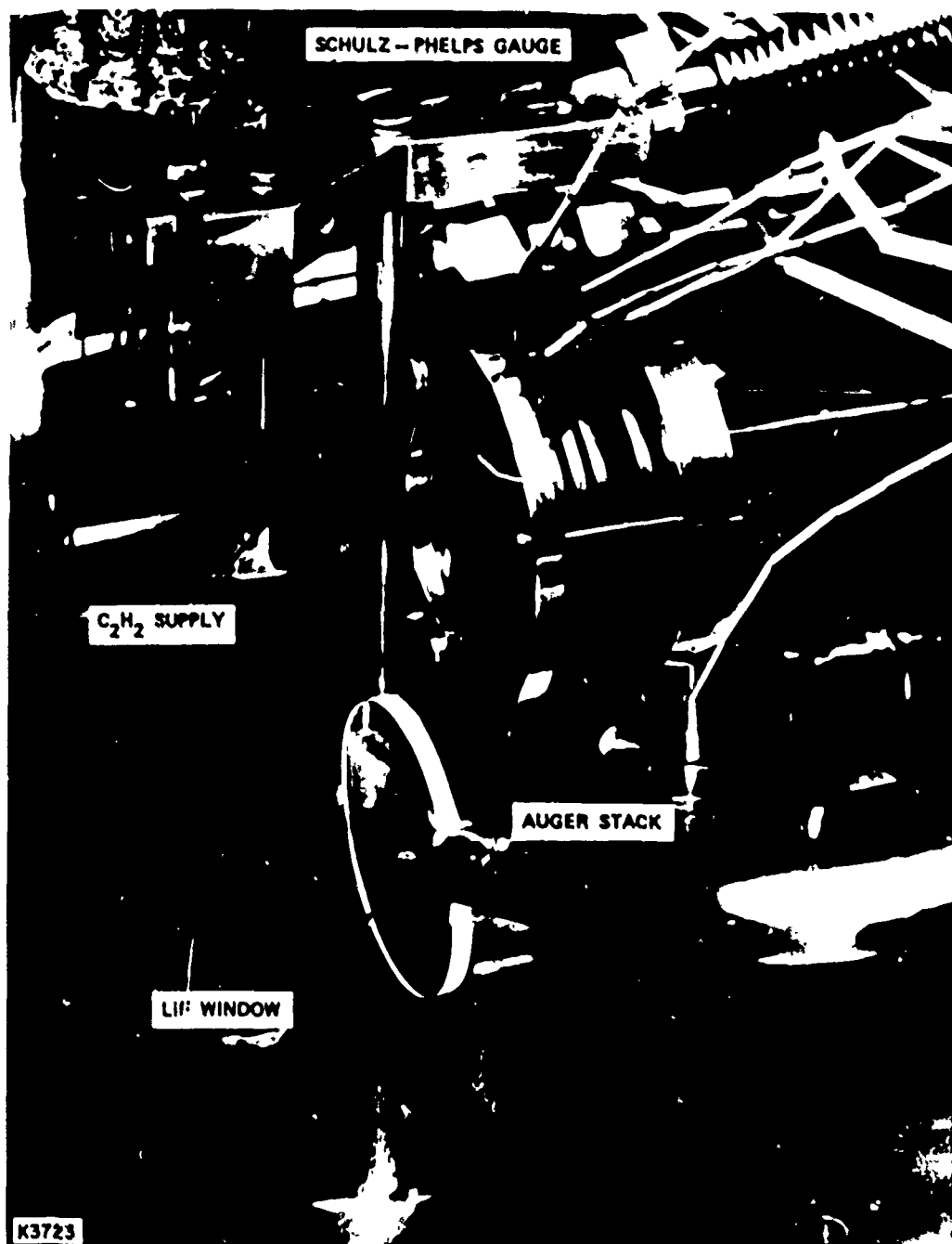
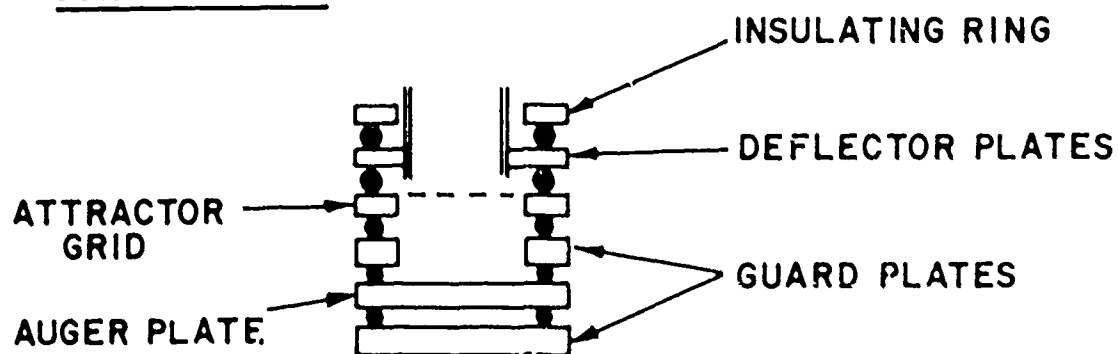


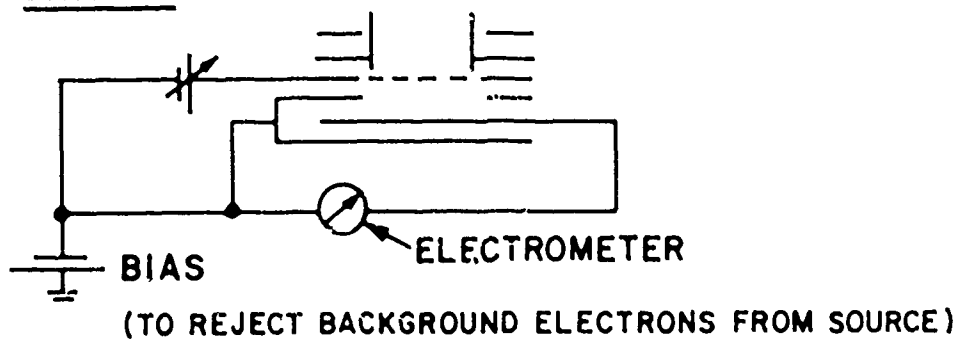
Figure 7 Photograph of Detectors

CONSTRUCTION



MATERIAL - MOLYBDENUM

CIRCUIT



H2680

Figure 8 Schematic of Auger Detector and Operating Circuit

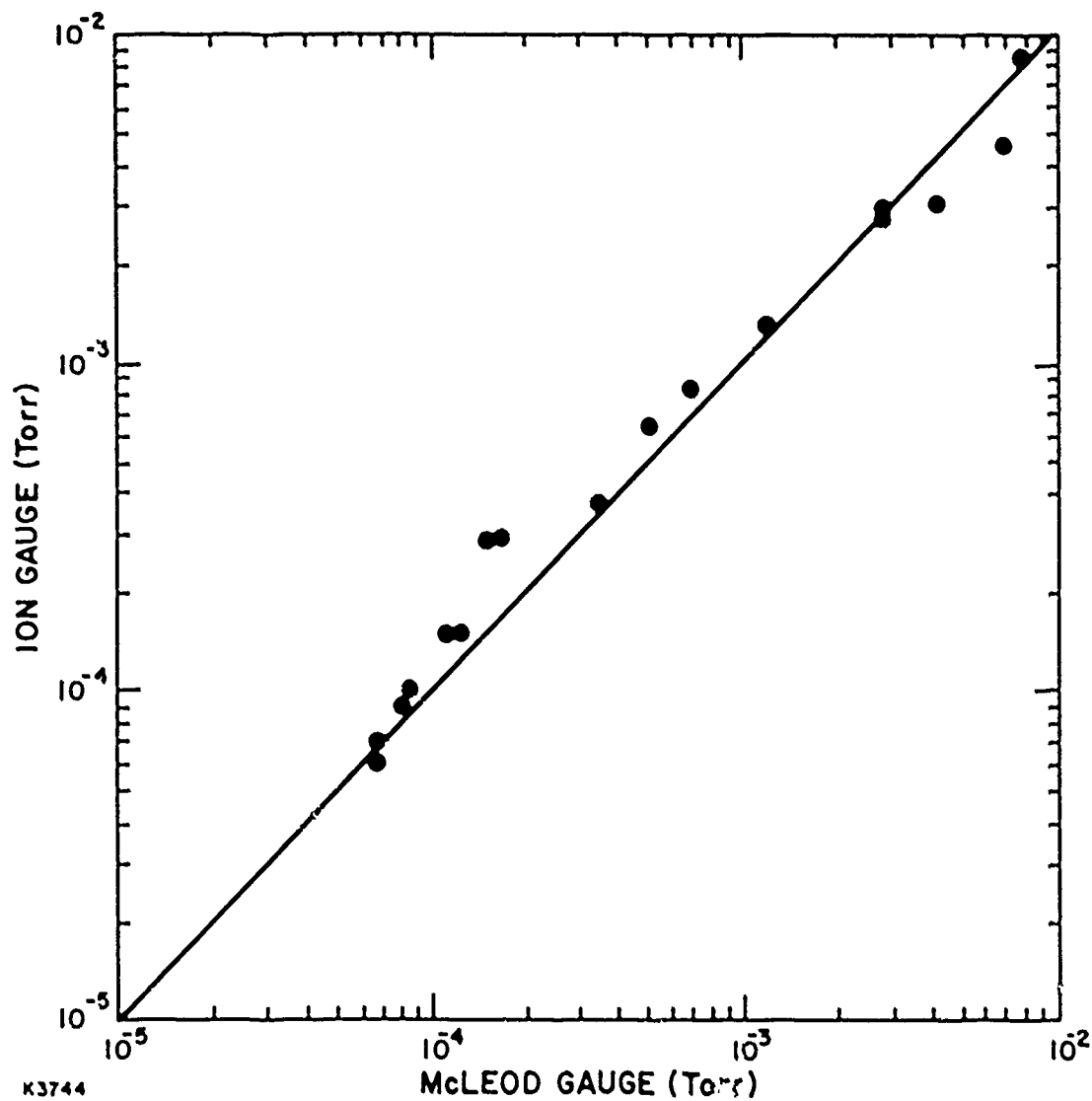


Figure 9 Schulz-Phelps Calibration Curve

range were measured. We assume that the error limit obtained at the higher pressures can be used in this lower pressure regime.

D. DIAGNOSTICS AND RESULTS

1. Discharge Diagnostics

The initial experiments involved measuring the discharge current enhancement due to partial ionization of an argon atom beam. Figure 10 indicates the total current drawn between the filament and plate number 2 in the absence of any ionization. The data was obtained for a 0.0127 cm diameter filament at an operating temperature of 2138°K. The temperature measurement was obtained by optical pyrometry including a correction for transmission losses through a quartz viewing port. The bias plate separation was 1 cm. The space charge limited behavior of the i - V characteristic is clearly indicated by the slope of curve drawn through the data points (crosses). At a fixed bias voltage (+35 V), the total current was then measured as a function of the pressure inside the source gas nozzle. This data is displayed in Figure 11. The current rises only slowly for pressures up to about 150 torr at which point the current increases dramatically (by almost two orders of magnitude) over a narrow pressure range, and then rises slowly for higher source pressures. Visual inspection indicates that a discharge is ignited in this high current region as is evidenced by a pale blue glow in the vicinity of the gas nozzle source. Similar results were found for both pure krypton and pure nitrogen beams except that the transition to the high current mode occurred for nozzle pressures around 100 torr for Kr and 180 torr for nitrogen. No discharge in helium was observed for source pressure up to 1000 torr.

During measurements of the metastable production in argon, krypton and nitrogen, source pressures in excess of 200 torr were not investigated due to an excessive gas load which could not be handled by the source chamber pumping system. At this pressure the gas flow from the 0.018 cm diameter nozzle is of the order of a few torr-l/sec.

2. Detector Diagnostics

The deflector plate voltage and the attractor grid voltage were optimized for metastable collection by monitoring the positive current emanating from the Auger collector plate as a function of each of these voltages. With the discharge lit and a nozzle pressure of about 160 torr argon, the Auger

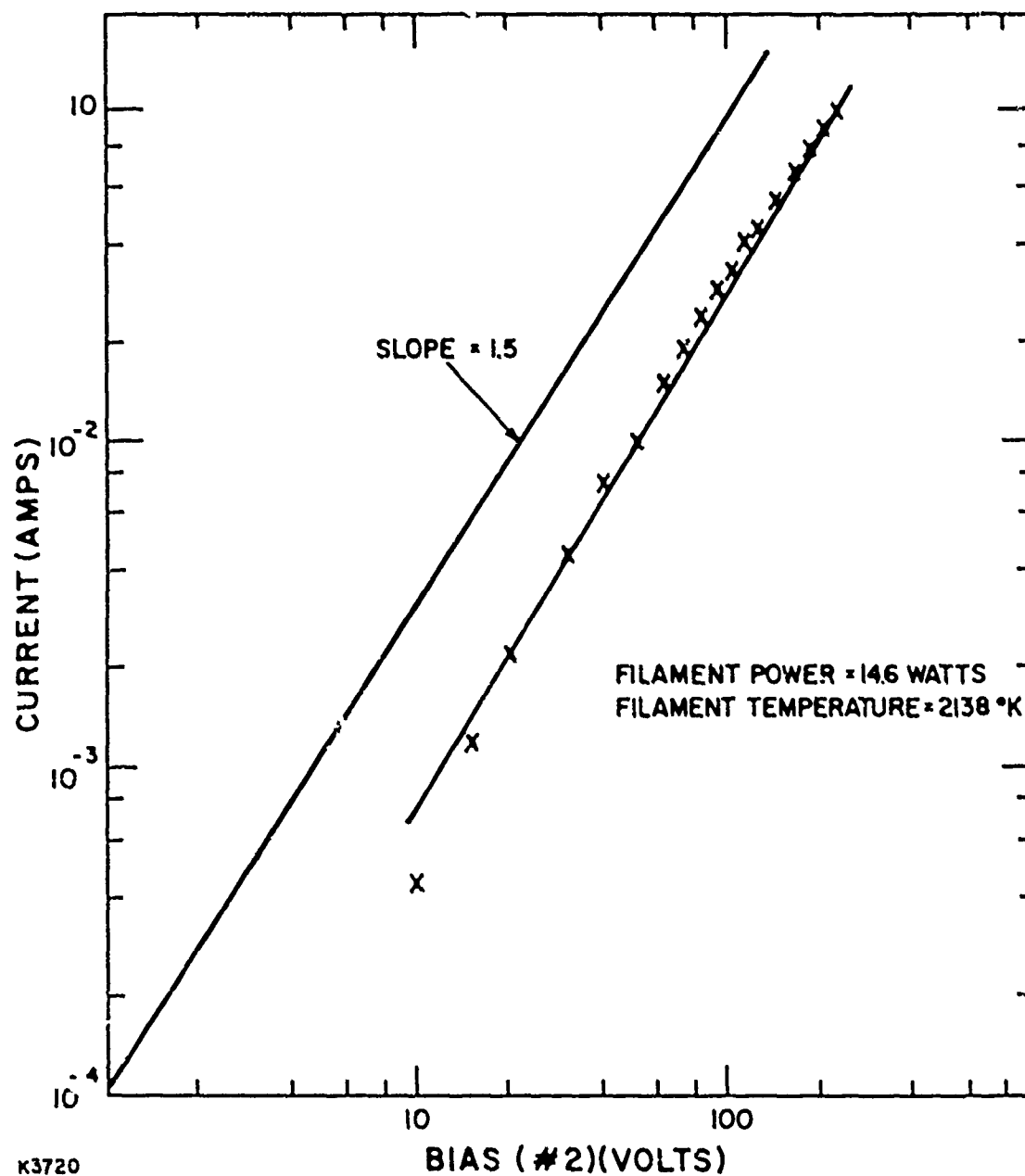


Figure 10 I-V Characteristics of Discharge Source in the Absence of Ionization

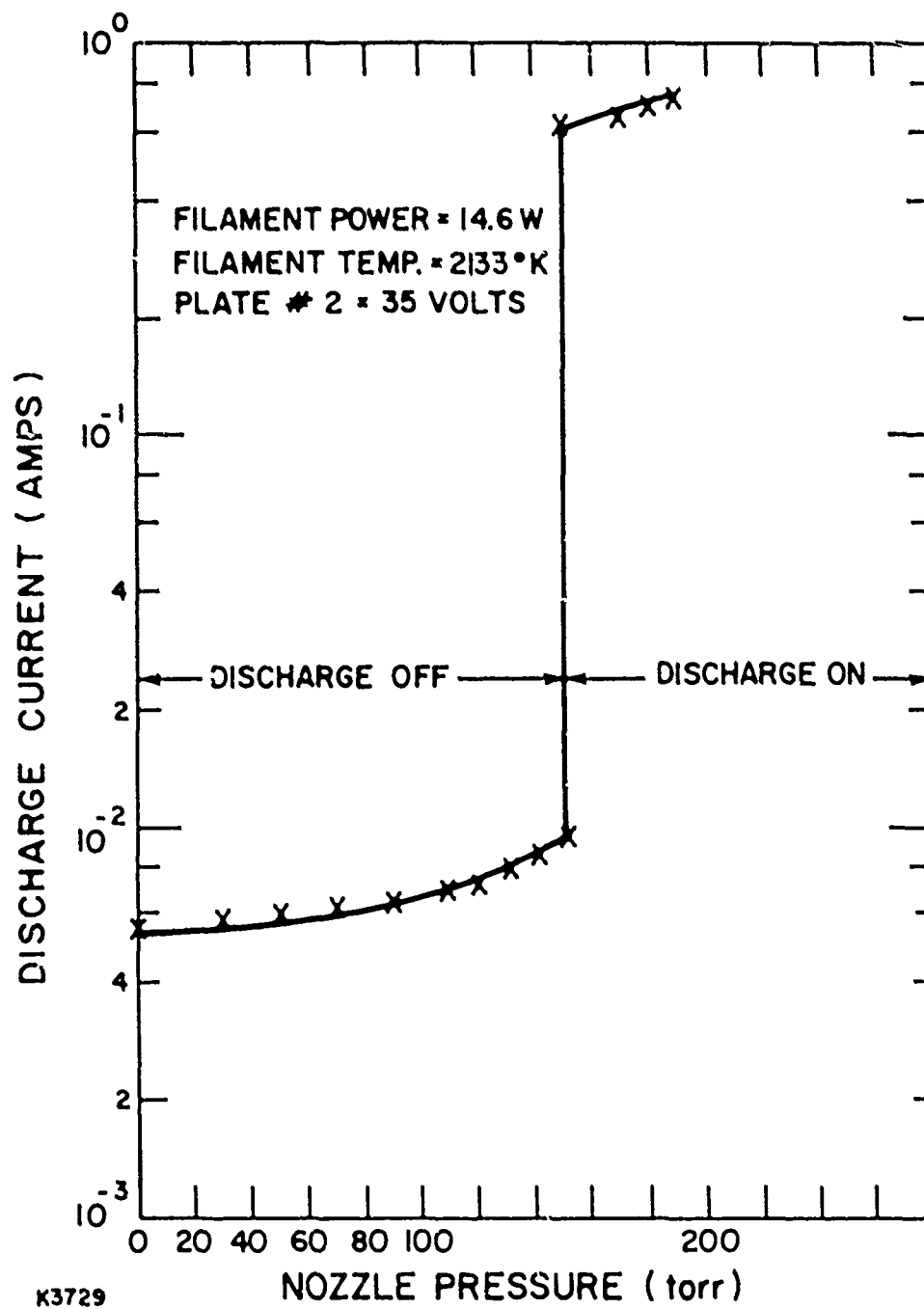


Figure 11 Discharge Current as a Function of Nozzle Source Pressure

signal is observed to be insensitive to deflector plate voltages greater than about 50 V. A similar result can be obtained by biasing the whole Auger stack 50 V negative with respect to the grounded discharge source suggesting that high energy electrons are the primary charged species carried in the beam. As is indicated in Figure 12, an attractor grid voltage of about + 20 V with respect to the Auger plate is required to insure that all the ejected Auger electrons are removed from the Auger plate. Higher attractor grid voltages are avoided to insure that the high energy discharge electrons do not impinge on the Auger plate and create secondary electrons.

3. Results

Using these optimal bias voltages, the Auger signal was measured as a function of the source nozzle pressure. These results are displayed in Figure 13 for conditions identical to Figure 11. A comparison of these two figures indicates that the Auger current behavior closely follows that of the source discharge current. Several additional checks were made to insure that the Auger current measured under "discharge on" conditions is a true measure of the metastable beam flux and is not contaminated by contributions from discharge photons or charged particles.

The photon contribution from a Kr discharge was estimated by observing the attenuation of the Auger signal when a LiF beam flag is interposed in the beam line to block all particles from hitting the detector. LiF crystal efficiently transmits over a very wide optical wavelength range (10 percent cutoff points: 100 and 9000 nm) including the krypton resonance line ($^1P_1 \rightarrow ^1S_0$) at 1165 Å where the LiF optical transmission is about 20 percent. Using a krypton discharge, the Auger signal attenuates by more than a factor of 100 when the beam flag is inserted directly in front of the Auger detector. This suggests that the photoemission contribution to the Auger signal is at most a few percent for the krypton metastable measurements. The similarity in the operating characteristics of the krypton, argon and nitrogen discharges suggests that photoemission also contributes negligibly to the argon and nitrogen Auger signals.

The presence of argon metastables in the beam was uniquely identified by a Penning ionization technique. The lowest lying argon metastable (3P_2 at

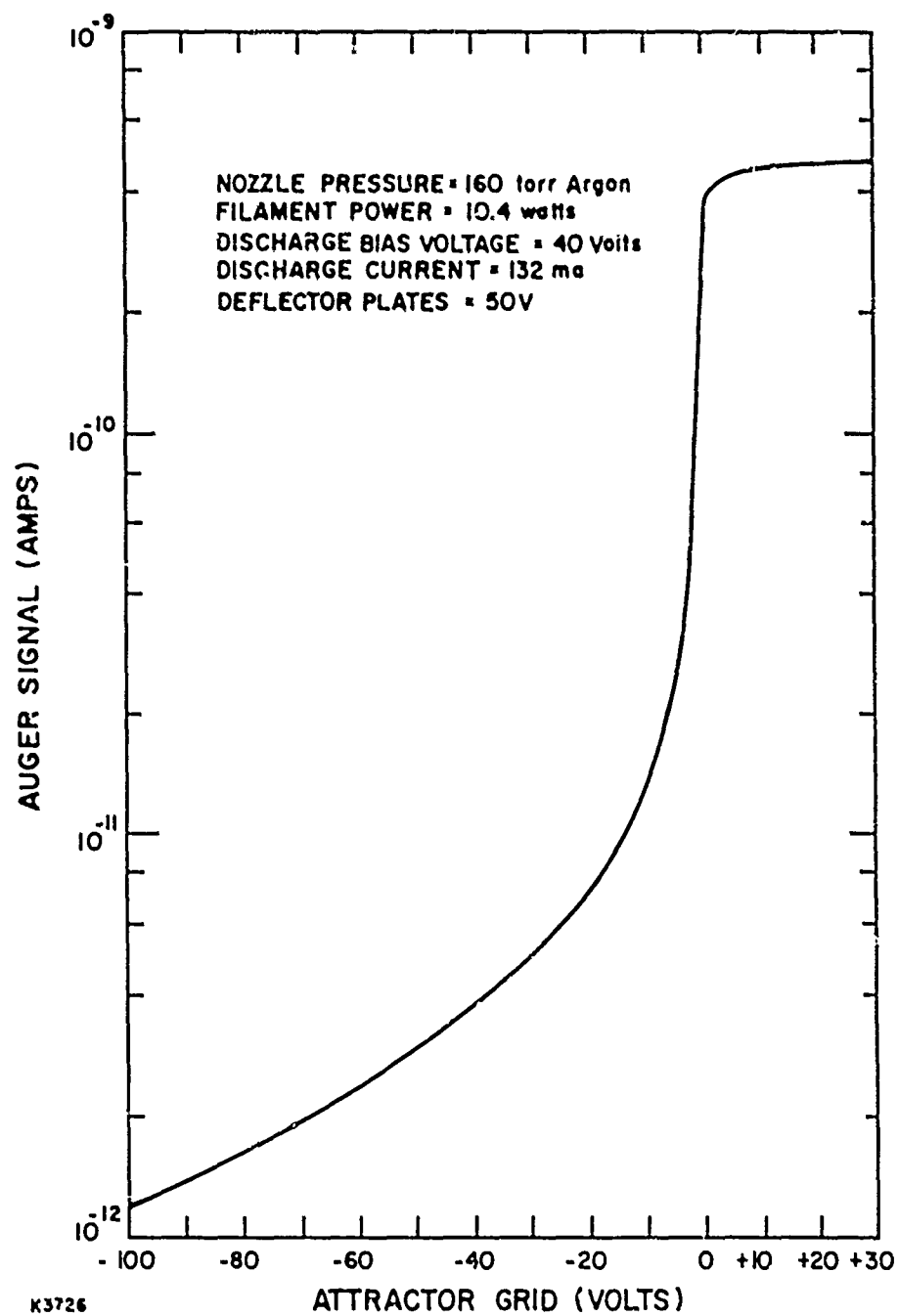


Figure 12 Auger Current as a Function of Attractor Grid Bias

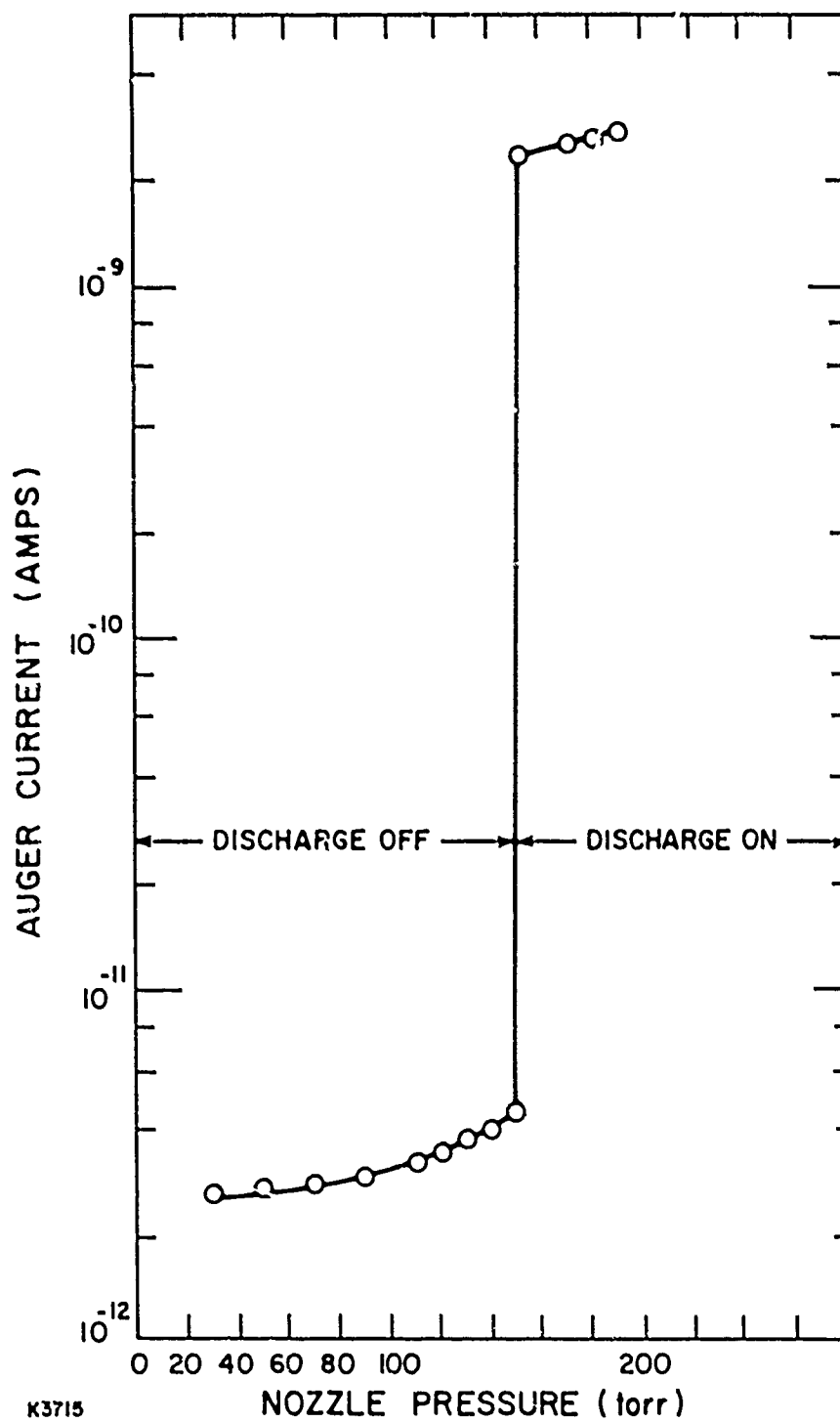


Figure 13 Auger Current as a Function of Nozzle Source Pressure

11.5 eV) is sufficiently energetic to Penning ionize C_2H_2 (ionization potential = 11.4 eV) but is insufficient to Penning ionize O_2 (ionization potential = 12.06 eV). On the other hand, Ar^+ (15.76 eV) can rapidly charge transfer to O_2 . A comparison of the ion currents collected when either C_2H_2 or O_2 are added to the metastable beam should give a relative indication of the Ar^+ and Ar^* (metastable) beam content. This measurement was accomplished by introducing a tiny flow of either gas through a capillary tube into the region between the deflector plates located directly ahead of the Auger plate (see Figure 7). The flow was directed nominally perpendicular to the beam line, and the resultant ion currents were collected on the deflector plates and measured with a sensitive electrometer. As C_2H_2 is added, the current to the deflector plates increases by about a factor of 30 at which point the current begins to saturate. Under similar conditions, the Auger current is reduced by a factor of about ten due to scattering and Penning ionization. For comparison, a negligible increase in the deflector plate current is observed when a comparable amount of oxygen is added sufficient to reduce the current to the Auger plate by a similar factor of ten. These results indicate that the ion content of the beam is negligible compared to metastable content, and that some fraction of the metastables is comprised of $Ar(^3P_2)$. We were unable to perform similar tests on krypton and nitrogen metastable beams. A potential problem for the N_2 metastable measurements is our current inability to distinguish between atomic and molecular metastable states in nitrogen. The atomic metastable states could be formed by dissociative excitation processes in N_2 discharges. Although the low lying $N(^4P)$ and $N(^4D)$ states have insufficient energy to eject Auger electrons from the gold surface (recommended work function = 4.3 eV), higher energy N atom metastable levels could contribute. The relative contribution of these states to our measured Auger current is not known at present.

Having concluded that the argon Auger current is a true measure of the argon metastable beam flux, the discharge source parameters were varied in order to optimize the metastable flux. The discharge bias voltage, discharge current and the nozzle source pressure are the parameters of primary interest here. Figure 11 has already indicated that there is only a slight increase in metastable flux for nozzle pressures in excess of that required to ignite the

discharge. Therefore, in light of this observation as well as for the need to remain within the pumping speed limitations of the vacuum system, we have held the nozzle pressure constant at ~ 150 torr (for argon), ~ 100 torr (for krypton), ~ 180 torr (for nitrogen) in these studies.

At fixed filament power, the discharge voltages at which the metastable signal optimizes are found to be: 30 to 40 V for krypton or argon and 50 to 60 V for nitrogen. Representative data for the optimization in a nitrogen beam are given in Figure 14. This variation is similar to that obtained in argon and krypton and is due to both variations in both the electron energy and electron current. These effects can be decoupled by varying the filament power at fixed discharge voltage. This data is shown in Figure 15 for both argon and krypton and nitrogen beams. In contrast to the data in Figure 14, the metastable signal varies monotonically with discharge current for each gas studied. The Auger current appears to be limited only by the filament burnout temperature ($\sim 2500^\circ\text{K}$) which is attained at about 30 W ($V_F = 7$ V, $I_F = 4.3$ amps) heater power corresponding to the high end of the abscissa in Figure 15. A comparison of Figure 14 and Figure 15 then suggests that the rollover at high discharge voltage can be directly attributed to an electron energy effect. We speculate that for discharge voltages below the peak in Figure 14, the increase in the ionization cross section with increasing electron energy dominates over any fall-off in the metastable excitation cross section leading to a net increase in the metastable signal. As the discharge voltage increases beyond the peak, the decrease in the metastable cross section begins to dominate over the slower rising ionization cross section leading to a net decrease in the metastable signal.

Several quantities are required to convert the Auger current measurements in Figure 15 into a metastable density value at the exit of the discharge zone: the secondary emission coefficient, n , for metastable impact on a gold-coated surface, the velocity distribution of the metastable beam, the angular distribution of metastables exiting from the discharge and the solid angle subtended by the detector. Of these only the Ar ($^3P_{2,0}$) secondary emission coefficient and the detector solid angle are known for these experiments. The secondary emission coefficient has been reported to be 0.66 ± 0.1

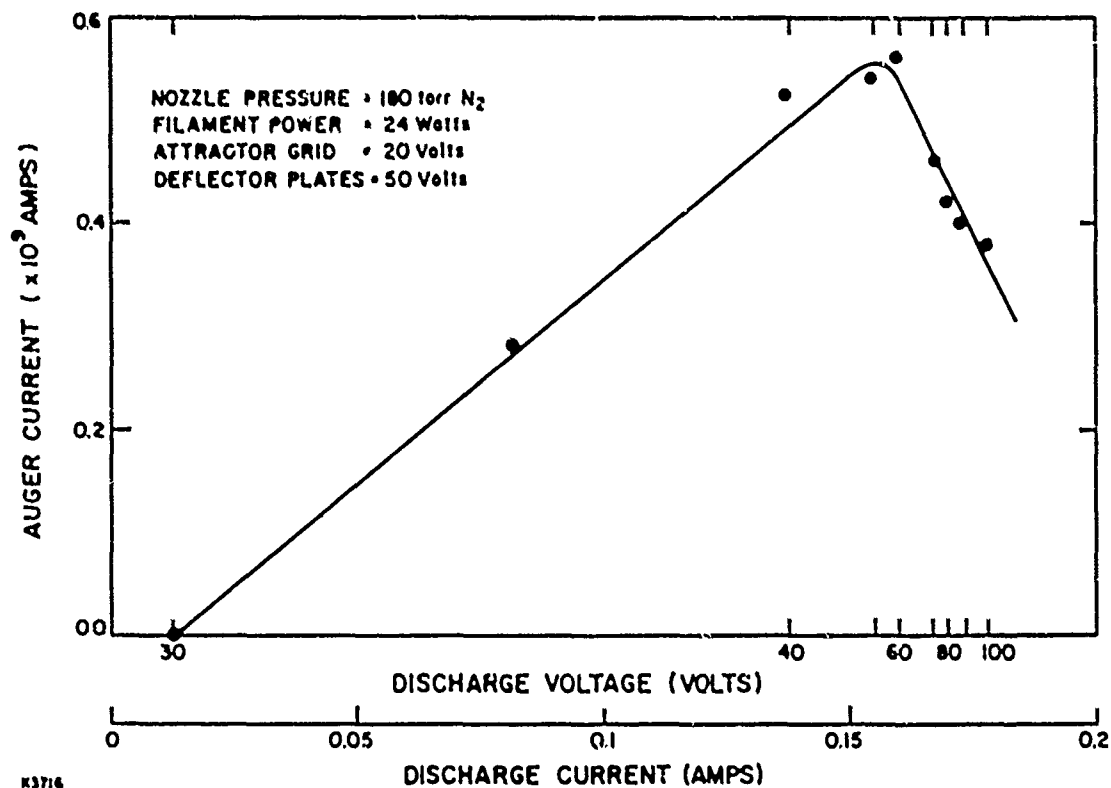


Figure 14 Auger Current as a Function of Discharge Voltage

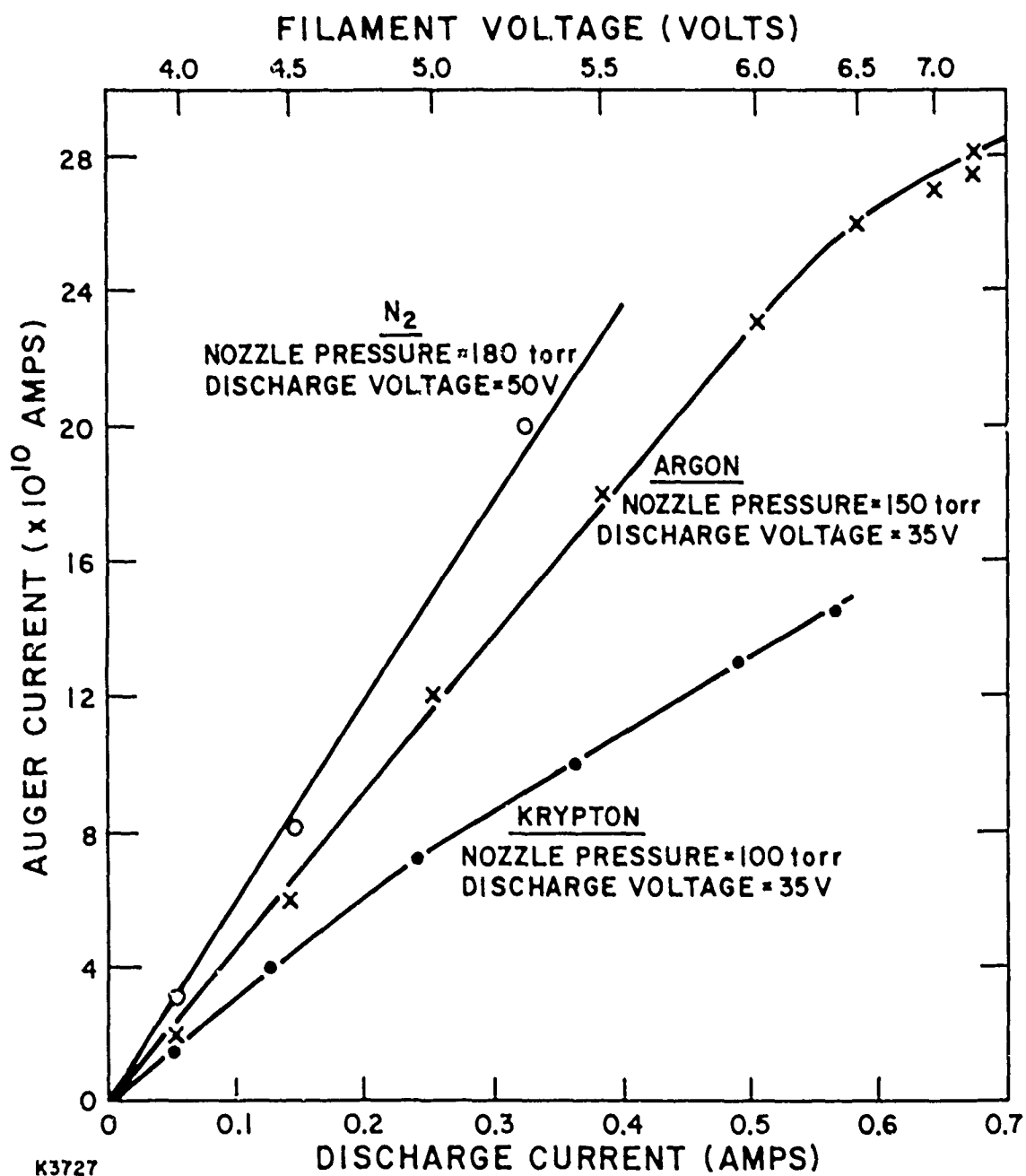


Figure 15 Kr, Ar and N_2 Metastable Signals as a Function of Discharge Current

for Ar ($^3P_{2,0}$).⁽⁵⁰⁾ The detector solid angle, $\Delta\Omega$, was established by locating a small aperture (0.079 cm^2) directly in front of the Auger plate at a distance of 8 cm from the discharge exit orifice. The angular and velocity distributions of the metastable beam need to be obtained experimentally due to the possibility of hydrodynamic flow at the discharge exit orifice. However, these measurements are difficult and were not attempted here.

We take what information is available to us and report the metastable flux per unit solid angle (a quantity analogous to brightness in optics), F , given by the expression

$$F = \frac{I^M}{\Delta\Omega A_s n e} \quad (6)$$

where I^M is the measured Auger current with the aperture in place, A_s is the discharge exit orifice cross-sectional area and e is the electron charge. We find that the I^M for argon is a linear function of the discharge source current, I_d , given by

$$I^M = 1.4 \times 10^{-9} I_d \text{ (in amps)} \quad (7)$$

for $I_d \leq 0.5 \text{ A}$. Using this value, the quantity, F , was evaluated for $\Delta\Omega = 1.2 \times 10^{-3} \text{ sr}$, $A_s = 1.14 \times 10^{-3} \text{ cm}^2$ and $n = 0.66$ to be about $10^{16} I_d$ metastables/ $\text{cm}^2\text{-sr}$ for an argon discharge. Using this value and our measurements of the atomic beam density, we estimate a fractional beam content of the order of 0.1 percent. Once the secondary emission coefficients for N_2 and Kr are known, the metastable yields for these gases can be scaled from F in argon using the data in Figure 15.

E. RECAP OF SOURCE AND DETECTOR OPERATING CONDITIONS

The optimal operating conditions for the discharge source and Auger detector are reviewed below:

50. Dunning, F.B., and Smith, A.C.H., J. Phys. 84, 1969 (1971).

a) Detector Conditions

Attractor Bias = +20 V relative to Auger plate

Deflector Bias \geq 50 V

Auger Plate = -50 V relative to case ground

Auger stack bias = -50 V relative to case ground

b) Source Conditions

Nozzle Pressure = 100 torr (Kr); 150 torr (Ar); 180 torr (N₂)

Discharge Voltage = +30-40 V (Kr and Ar); +50-60 V (N₂)

Discharge Current \leq 700 mA

Filament Temperature (0.0127 cm diameter) \leq 2500°K

F. PROPOSAL FOR MEASUREMENT OF ABSOLUTE METASTABLE DENSITY

We propose using the Penning ionization technique described previously to make absolute density measurements of argon metastables. The technique requires making absolute measurements of the electron currents generated from the process:



where Ar* is a metastable excited state and M is an appropriate collision partner that can be Penning ionized. For detecting Ar metastables, the ionization potential of this species must be \leq 11.55 eV, the energy of the lowest Ar metastable state. The electron current generated via reaction (8) will tend to a saturated value, I_e^S , as the M gas density is raised. At this point all the Ar* metastable species will be ionized. The value of I_e^S can then be related to the number density, ρ_M , via:

$$\rho_M = \frac{I_e^S}{eV_e A} \quad (9)$$

where V_e is the Penning electron velocity, A is the electron collector area and e is the electronic charge. In effect, this procedure converts one species (metastables) whose density is difficult to directly measure into another species (electrons) the density of which is relatively easy to measure.

The metastable density can be obtained from measurements of the total current and the electron energy distribution. This latter quantity can be obtained using an electrostatic energy analyzer. An accurate measurement of I_e^S would require a Penning electron collection efficiency approaching 100 percent. Electron scattering into angles outside the field of view of the electron collection optics would be the major effect that could reduce the efficiency below unity. The collection efficiency would be maximized by using an M-gas for which the cross-section ratio σ_p/σ_M , the ratio of the Penning cross section to the momentum transfer cross section, is large. This would insure minimal amount of e-M large angle scattering. The collection efficiency could also be optimized by choosing the M-gas such that the product electron would have little excess translational energy.

C_2H_2 is a reasonable M gas candidate. The energy difference between $Ar(^3P_2)$ and $C_2H_2^+$ is only 0.15 eV. The momentum transfer (and rotational excitation) cross sections are not known although it is expected that $\sigma_M(C_2H_2)$ is small due to its zero dipole moment and small polarizability. On the other hand, the $Ar(^3P_2)/C_2H_2$ Penning ionization cross section has been measured to be $> 10^{-15} \text{ cm}^2$ at high energy ($\geq 100 \text{ eV}$), and the cross section is rising towards lower energy.⁽⁵¹⁾

51. Moseley, J.T., Peterson, J.R., Lorents, D.C., and Hollstein, M., Phys. Rev. A6, 1025 (1972).

IV. METHODS FOR PRODUCING HIGH THROUGHPUT SOURCES OF METASTABLE ATOMS AND MOLECULES

The objective of this phase of the program is to investigate the possibility of developing sources that can generate high flux levels of metastable atoms and/or molecules. An arbitrary preliminary design goal of the order of $10^{21} - 10^{22}$ metastables $\text{cm}^{-2} \text{sec}^{-1}$ is assumed. An additional constraint requiring flow velocities that do not exceed the speed of sound insures that the internal energy of the metastables greatly exceeds the translational kinetic energy. At a typical sound speed of the order of 10^4 cm/sec, the required metastable density levels are of the order of $10^{17} - 10^{18} \text{cm}^{-3}$, a range that is orders of magnitude larger than most any metastable source (except one) with which we are familiar. The one exception is the $\text{O}_2(^1\Delta_g)$ chemical metastable generator that is used in the $\text{O}_2(^1\Delta_g)/\text{I}$ chemical laser system. $\text{O}_2(^1\Delta_g)$ densities of the order of $\sim 10^{17} \text{cm}^{-3}$ have been reported.

Four different approaches were considered in this study. Discharge production of the metastable $\text{N}_2(\text{A})$ state was investigated using an e-beam sustained discharge to generate volumetric pumping at the high energy loadings needed to provide a high flux level. The ability to independently vary the e-beam current and discharge voltage to optimize the A-state production is a decided advantage of the e-beam-sustained discharge over more conventional self-sustained discharge sources. On the other hand, the issue of the hot electrons, which both produce the A-state and, unfortunately destroy it by cumulative ionization and dissociation processes, arises in all discharge pumping techniques and cannot be avoided. An alternative approach which attempts to circumvent the hot electron problem is production of metastables via electron-ion recombination processes which are most efficient for cold electrons due to the inverse electron temperature dependence of most electron-ion recombination rate constants. We have investigated this concept using a magnetic annular arc (MAARC) generator as a high-temperature thermal ionization source of ions and electrons. The recombination of ions and electrons is

allowed to take place in a cool region that is spatially removed from the ion source. The plasma is physically transported from hot to cold regions by a flow and confining magnetic field

Experience in atomic and molecular physics suggests that optical excitation techniques should be expected to be more efficient and selective than processes using electrons. Generally speaking, the optical selection rules and photon energy resonance requirements lead to preferential excitation of fewer levels and decidedly fewer loss processes than occurs for nonresonant electron impact excitation. As a result, we have investigated two purely optical metastable production techniques. The first uses a two-color optical pumping scheme for production of low lying metastable levels in the heavier rare gases (krypton and xenon). The second uses a stimulated Raman technique to produce vibrationally excited H_2 and N_2 .

A. STIMULATED RAMAN SCATTERING PRODUCTION OF H_2 ($v=1$) and N_2 ($v=1$)

1. Introduction and Background

Stimulated Raman scattering (SRS) involves an inelastic scattering mechanism in which a photon incident on an atom or molecule causes that atom or molecule to undergo a change in internal energy and emit a photon that is shifted in wavelength from the incident photon by that exact change in internal energy. In the case of an atom, the internal energy is in the form of an electronic transition (see Figure 16). For a molecule, the change in internal energy can be vibrational or rotational. We intend to make use of SRS to produce significant fractional populations of vibrationally excited diatomic molecules at high densities to meet the desired high flux requirements.

The molecular Raman process, involving a very non-resonant scattering process, has a smaller Raman cross section than is typical for the atomic case and, therefore, experiments are typically carried out at high pressure. In fact, pressure is one of the most significant parameters affecting the molecular SRS process. This is because the variation in pressure will affect both the number density of the scatterer and the spontaneous Raman linewidth. Since the gain is equal to the Raman cross section times the density times the length, i.e.,

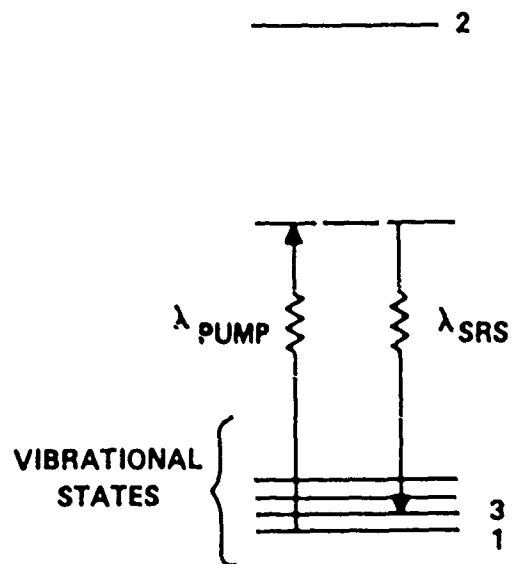
$$\text{Gain} = \sigma n L$$

and the Raman cross section is inversely proportional to the Raman linewidth for the case of forward SRS, a consideration of the pressure influence on the gain is important. This will enable us to evaluate the quantitative performance of this Raman approach for a variety of system total pressures.

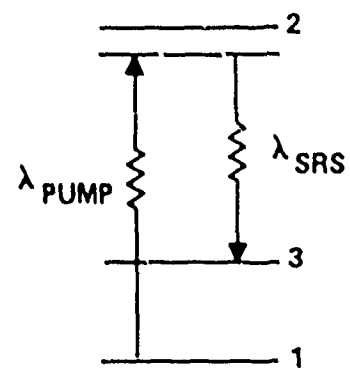
For H_2 , there are three distinct pressure regimes for the Raman linewidth (see Figure 17). At very low pressures, the linewidth is primarily determined by Doppler broadening $\Delta\tilde{\nu}_D = 2\tilde{\nu}/C \sqrt{2 \ln 2} \sqrt{kT/M} = 3.6 \times 10^{-2} \text{ cm}^{-1}$ for forward scattering. In the collision narrowing regime, $\Delta\tilde{\nu}_{CN} = 4\pi D/\lambda \cdot 1/C = 9.74 \times 10^{-3} \text{ cm}^{-1}/M(\text{Ang})$ where D is the diffusion coefficient of H_2 in H_2 ($D = 1.35$), C is the speed of light and $\Delta\tilde{\nu}_{CN} = \Delta\tilde{\nu}_D$ at $\lambda = 0.27 \text{ Ang}$ or 205 torr.⁽⁵²⁾ At slightly higher pressures, the

52. Murray, J.R. and Javan, A., J. Molec. Spectry 42, 1 (1972); Dicke, R.H., Phys. Rev. 89, 472 (1953).

MOLECULAR SRS

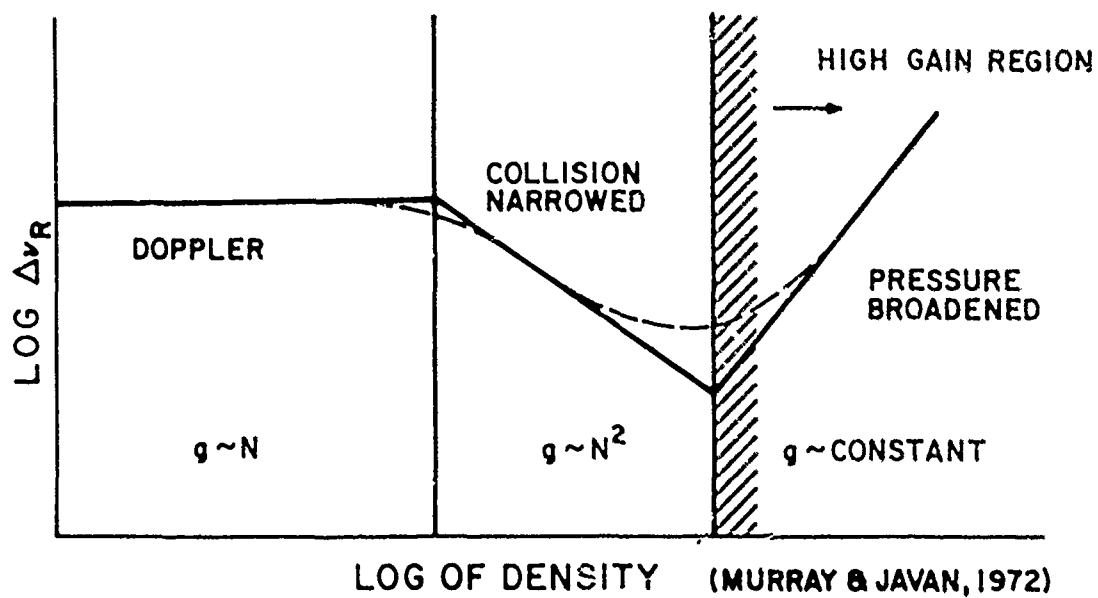


ATOMIC SRS



H8143

Figure 16 Stimulated Raman Scattering (SRS)



J6973

$$\text{GAIN} = \sigma NL \sim \frac{1}{\Delta\nu_R} NL$$

Figure 17 Pressure Effect of H₂ Raman Linewidth

forward scattering Raman linewidth decreases due to collision narrowing effects resulting from the frequent velocity-changing, but not phase-changing, collisions. In this regime, the linewidth becomes inversely proportional to the density of the collision partner (i.e., H_2) and, therefore, the gain scales as the density squared. At still higher pressures where $\Delta\tilde{\nu}_{CN} = \Delta\tilde{\nu}_{PB}$ i.e., the linewidth becomes pressure broadened, the gain becomes independent of pressure.

We can now calculate the gain in each of these three regimes, first defining a $g(\lambda)$ such that

$$g(\lambda) = \frac{f(\lambda)}{\Delta\tilde{\nu}}$$

with $\Delta\tilde{\nu}$ independent of pump wavelength. Therefore,

$$g_{PB}(\lambda) = \frac{f(\lambda)}{\Delta\tilde{\nu}_{PB}}$$

$$g_{CN}(\lambda) = g_{PB}(\lambda) \frac{\Delta\tilde{\nu}_{PB}}{\Delta\tilde{\nu}_{CN}} = g_{PB}(\lambda) \frac{1.5 \times 10^{-3} N}{9.74 \times 10^{-3}/N} = 0.154 N^2 g_{PB}(\lambda)$$

$$g_D(\lambda) = g_{PB}(\lambda) \frac{\Delta\tilde{\nu}_{PB}}{\Delta\tilde{\nu}_D} = g_{PB}(\lambda) \frac{(1.5 \times 10^{-3} N)}{(3.6 \times 10^{-2})} = 0.0417 N g_{PB}(\lambda)$$

The value of $g_{PB}(\lambda)$ in cm/W as a function of wavelength is plotted in Figure 18 normalized to the data of Bloembergen et al.⁽⁵³⁾ The pressure broadened linewidth of $1.5 \times 10^{-3} N$ was taken from Murray et al.⁽⁵⁴⁾ Using these relationships, with various laser pump sources, we arrive at the following values:

	Ruby ($\lambda = 694 \text{ nm}$)	KrF ($\lambda = 248 \text{ nm}$)	ArF ($\lambda = 193 \text{ nm}$)
g_D	$6.3 \times 10^{-11} N$	$3.6 \times 10^{-10} N$	$6.7 \times 10^{-10} N$
g_{CN}	$2.3 \times 10^{-10} N^2$	$1.3 \times 10^{-9} N^2$	$2.5 \times 10^{-9} N^2$
g_{PB}	1.5×10^{-9}	8.6×10^{-9}	1.6×10^{-8}

53. Bloembergen, N., Bret, G., Lallemant, P., Pine, A. and Simova, P., IEEE J. Quant. Electron QE-3, 197 (1967).

54. Murray, J.R., Goldhar, J., Eimer, D., and Szöke, A., IEEE J. Quant. Electron QE-15, 342 (1979).

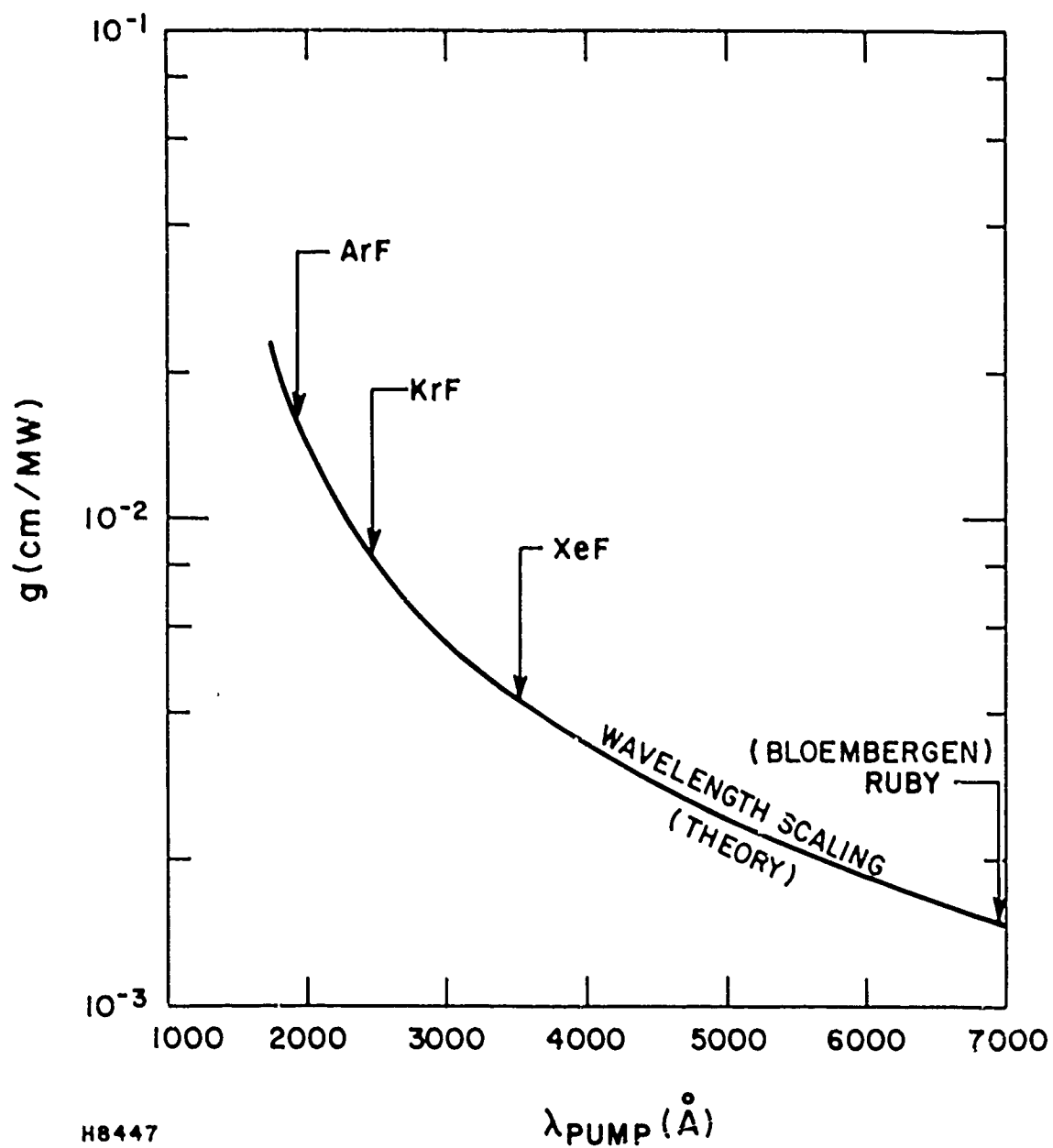


Figure 18 First Stokes Gain for Forward SRS in H₂

Similarly, one can explore the analogous processes for SRS in nitrogen but unfortunately little information is available with regard to the effect of pressure on the Raman linewidth in the regime of interest. Murray et al.⁽⁵⁴⁾ suggest that for pressures of a few atmospheres or more, the linewidth is probably independent of density. At very high pressures (> 200 Atm) the linewidth begins to narrow such that at liquid densities it is only about 0.067 cm^{-1} . For this reason, most SRS studies involving nitrogen have been carried out using liquid nitrogen, which is unacceptable for the present application. If the Raman linewidth is indeed independent of density for pressures below 1 atm, then the gain scales with density. Using the published value for g at 486 nm and scaling with wavelength to $\lambda = 560 \text{ nm}$ (see below for choice of appropriate wavelength) we obtain

$$g = 1.38 \times 10^{-12} \text{ N},$$

which is considerably smaller than those for H_2 (see above).

These cross sections can now be used to calculate the expected number densities of vibrationally excited H_2 or N_2 that can be produced by co-propagating (i.e., coherently mixing) both pump and Stokes photons, which act to shift population from the lowest $v = 0$ state (i.e., N) to the $v = 1$ state (i.e., N^*). At this time, let us assume the Stokes photons are produced arbitrarily. A rate expression describing this excitation process is

$$\frac{dN^*}{dt} = \sigma_{\text{SRS}} \phi_S N$$

where σ_{SRS} is the SRS cross section in cm^2 and ϕ_S is the flux of photons at the Stokes frequency. Assuming no saturation effects (i.e., small changes in N , ϕ_{pump} and ϕ_S),

$$N^* = \sigma_{\text{SRS}} \phi_S N \tau_{\text{pulse}}$$

Substituting

$$\sigma_{\text{SRS}} = \sigma'_{\text{SRS}} I_p,$$

where σ'_{SRS} is the SRS "cross section" in cm^4/W , we obtain

$$N^* = \sigma'_{\text{SRS}} I_p \phi_S N \tau_{\text{pulse}}$$

Now $\sigma_{\text{SRS}}' N = g(\text{cm/W})$, which we have tabulated above, and $\phi_s = I_s/h\nu_s$, therefore

$$N^* = \frac{q}{h\nu_s} I_p I_s \tau_{\text{pulse}}$$

and values of $g/h\nu_s$ can be tabulated as before. For H_2 ,

	Ruby ($\lambda = 694 \text{ nm}$)	KrF ($\lambda = 248 \text{ nm}$)	ArF ($\lambda = 193 \text{ nm}$)
$g_D/h\nu_s$	$3.2 \times 10^8 \text{ N}$	$5.0 \times 10^8 \text{ N}$	$7.0 \times 10^8 \text{ N}$
$g_{CN}/h\nu_s$	$1.2 \times 10^9 \text{ N}^2$	$1.8 \times 10^9 \text{ N}^2$	$2.6 \times 10^9 \text{ N}^2$
$g_{PB}/h\nu_s$	7.8×10^9	1.2×10^{10}	1.7×10^{10}

whereas $g/h\nu_s$ for nitrogen is $4.5 \times 10^5 \text{ N}$ at $\lambda_{\text{pump}} = 560 \text{ nm}$. From these data, it is apparent that the quantity $g/h\nu_s$ is very weakly wavelength dependent. This arises because $g \sim \nu_s g'(\lambda)$, and $g'(\lambda)$ has a wavelength dependence which is only due to the resonance denominator, which is very non-resonant for all of these pumps and, therefore, a very weak function. Although ArF has minor gain advantage, its short wavelength poses optics damage considerations and, therefore, we shall pursue our calculations using KrF ($\lambda = 248 \text{ nm}$) as the pump for H_2 . We will also assume we will generate the needed Stokes radiation ($\lambda = 277 \text{ nm}$) in a high-pressure hydrogen cell.

2. Proposed Experimental Set-Up and Predicted Yields

Based on experience at AERL with commercially available KrF lasers and SRS conversion in H_2 ,⁽⁵⁵⁾ the following values for the needed parameters are considered to be realistic estimates. For an unstable cavity operated Lumonics (Model TE-261-2) laser, energy expected at KrF wavelengths is 80 mJ in a 8 nsec pulse. From our SRS work⁽⁵⁵⁾ and that of others,⁽⁵⁶⁾ we project we can easily convert 50 percent of this energy into a number of Stokes and anti-Stokes lines with most (75 percent) going into the desired S_1 radiation. Therefore, after the pump has been converted in the high

55. Trainor, D.W., Hyman, H.A., Itzkan, I. and Heinrichs, R.M., App. Phys. Lett. 37, 440 (1980).

56. Loree, T.R., Sze, R.C. and Barker, D.L., App. Phys. Lett. 31, 37 (1977); Loree, T.R., Sze, R.C., Barker, D.L. and Scott, P.B., IEEE J. Quant. Electron QE-15, 337 (1979).

pressure cell (see Figure 19), we have $E_p = 40$ mJ and $E_s = 30$ mJ. This 30 mJ of 277 nm radiation corresponds to 4.2×10^{16} photons, thereby establishing the maximum number of excited $H_2(v=1)$ states that can be achieved with this pump. This number and the desire to have high fractional excitation places constraints on operating conditions.

Since $I_p = E_p/\tau_p A$ and $I_s = E_s/\tau_p A$, where A is the cross-sectional area of the beam, then

$$N^* = \left(\frac{q}{h\nu_s} \right) \left(\frac{E_p}{\tau_p A} \right) \left(\frac{E_s}{\tau_p A} \right) \tau_p$$

Also, with $A = \pi w^2$, then N^* for H_2 for each pressure regime can be tabulated as a function of beam waist in the farfield (i.e., focal spot size). For these assumed experimental conditions, we have

$$N_D^* = \frac{2.75 \times 10^{-7}}{w^4} \quad N < 7.3 \times 10^{18} \text{ cm}^{-3}$$

$$N_{CN}^* = \frac{3.75 \times 10^{-26}}{w^4} N^2 \quad 7.2 \times 10^{18} \leq N \leq 7 \times 10^{19} \text{ cm}^{-3}$$

$$N_{PB}^* = \frac{1.8 \times 10^{-16}}{w^4} \quad N > 7 \times 10^{19} \text{ cm}^{-3}$$

where the beam waist (for a diffraction limited beam) is given by

$$w = \frac{1.22 f \lambda}{D}$$

where f is the focal length of the optics employed, λ , is the wavelength and D is the diameter of the incident laser beam. The depth-of-field over which the beam is within a factor of the $\sqrt{2}$ of this beam waist is given by

$$z_v = \frac{\pi w^2}{\lambda} \quad (\text{i.e., the Rayleigh Range})$$

Therefore, the irradiated volume is approximately

$$\text{Vol} = \pi w^2 z_v = \frac{\pi^2 w^4}{\lambda}$$

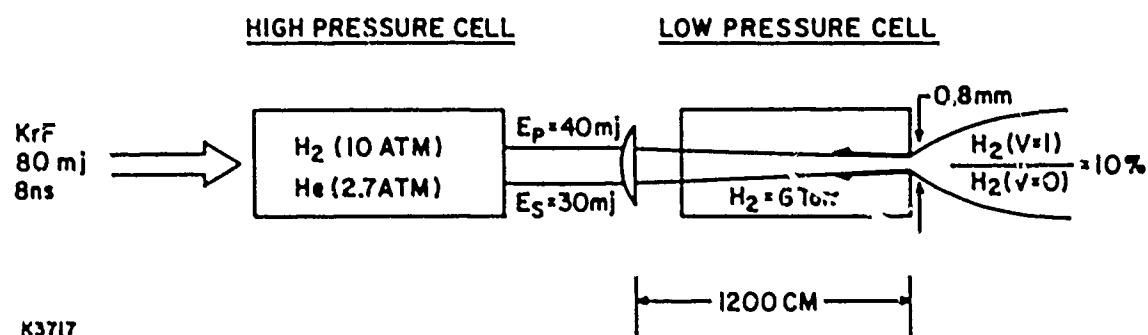


Figure 19 Experimental Setup for H₂ SRS

The number of excited states in this volume (for the Doppler regime) is

$$\text{Vol} * \text{density} = \frac{\pi^2 w^4}{\lambda} * \frac{2.75 \times 10^{-7}}{w^4} N$$

$$\# \text{ excited states} = 0.098 * N$$

which must be smaller than the number of photons available, i.e.,

$$0.098 * N < \frac{E}{h\nu} = \frac{30 \times 10^{-3} \text{ J}}{1.6 \times 10^{-19} * 4.48} = 4.2 \times 10^{16}$$

Assuming one is restricted to converting $\sim 1/2$ the number of photons available, then $N * \text{Vol} \sim 2 \times 10^{16}$ or $N \leq 2 \times 10^{17} \text{ cm}^{-3}$, or

$$N * \text{Vol} = N * \frac{\pi^2 w^4}{\lambda} = 2 \times 10^{16}$$

and

$$N * w^4 = 2 \times 10^{16} \frac{\lambda}{\pi^2}$$

or

$$\log N * + 4 \log w = 10.75$$

A plot of this equation is shown in Figure 20. It shows for 10 percent excitation into the $v = 1$ level, the beam waist is $w = 0.41 \text{ mm} = 0.041 \text{ cm}$. This corresponds to a Rayleigh range of 190 cm and an irradiated volume of $\sim 1 \text{ cm}^3$. These focal parameters can be accomplished through a system with an effective focal length given by

$$f = \frac{w D}{1.22} \sim 1200 \text{ cm for } D = 1 \text{ cm.}$$

This long focal length can be achieved in a compact manner through use of a Galilean type telescope arrangement, which avoids breakdown concerns, which may occur with use of a Keplerian type.

We have now defined a typical set of experimental conditions for the low pressure cell. They are summarized as follows:

H_2 pressure = 6.2 torr = $2 \times 10^{17} \text{ cm}^{-3}$ for $\text{H}_2(v=1)/\text{H}_2 = 10$ percent excitation implies $\text{H}_2(v=1) = 0.62 \text{ torr} = 2 \times 10^{16} \text{ cm}^{-3}$ for the case of a beam diameter = $2w \approx 0.08 \text{ cm} = 0.8 \text{ mm}$. Assuming a flow velocity which is sonic, $v = \sqrt{2KT/M} = 1.5 \times 10^5 \text{ cm/sec}$. For this velocity and this density, one would anticipate a flux of $\sim 3 \times 10^{21} \text{ cm}^{-2} \text{ sec}^{-1}$, which is

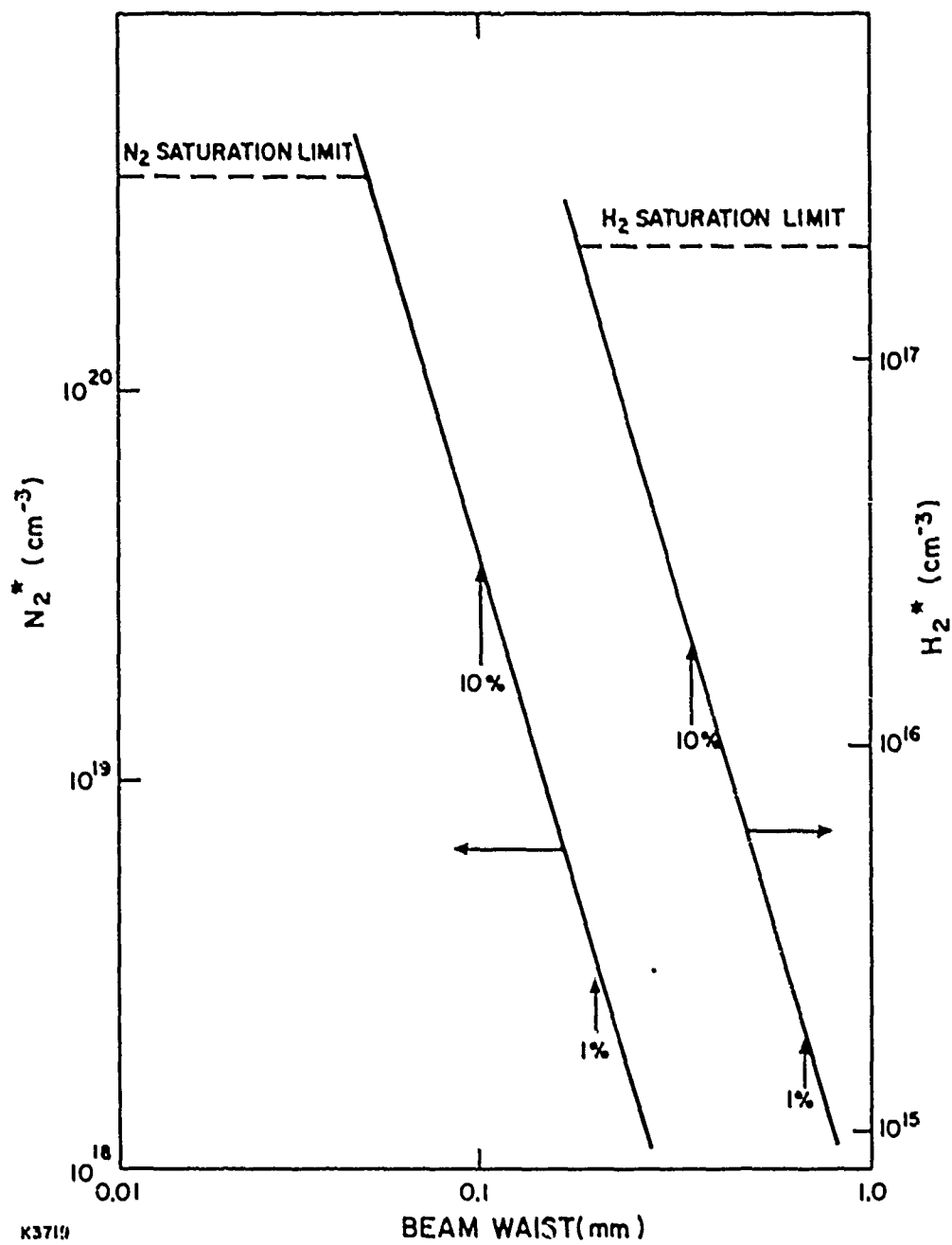


Figure 20 H_2^* and N_2^* Production as a Function of Laser Beam Waist

near the Task requirements. In practice, both the velocity and density at the exit plane will be reduced somewhat but the development presented here would not change significantly. (Significant increases in flux can be realized through additional laser pump energy or different focal parameters (see Figure 20)).

The Raman frequency shift due to the high-pressure gas ($H_2 = 10$ atm) in the high-pressure cell will tend to drive the frequency difference between the pump and the Stokes photon off the resonance value for coherent excitation of the low pressure H_2 ($p \sim 6$ torr). However, a full compensation can be accomplished through the addition of 2.73 atm of Helium to the high pressure cell (see Ref. 57).

The ease of accomplishing this correction in H_2 is to be contrasted with N_2 , where the gas phase vibrational Raman shift has been measured at 2327 cm^{-1} , whereas at liquid densities (a convenient high pressure cell) the shift is 2331 cm^{-1} . This corresponds to a change in frequency of 4 cm^{-1} , which is much too large to be conveniently circumvented. For this reason, we have explored the use of two high power dye lasers to generate the pump and "Stokes" photons for the calculation of SRS production of $N_2(v=1)$.

Current state of the art commercial dye laser devices have demonstrated 200 mJ in 10 nsec at 575 nm using a doubled yag laser to pump rhodamin 6 G. Similarly, one can expect near 60 mJ in 10 nsec at 644 nm through use of Rhodamin 640 dye. These commercially available lasers would, thereby, produce the following excitation in nitrogen.

$$N^* = \frac{2 \times 10^{-9}}{w^4} N$$

As before, the number of excited states in a focal volume

$$\text{Vol} \times \text{density} = \frac{\pi^2 w^4}{\lambda} * \frac{2 \times 10^{-9}}{w^4} N$$

$$\# \text{ excited states} = 3.07 \times 10^{-4} N$$

which must be smaller than the number of photons

$$3.07 \times 10^{-4} N < \frac{E}{h\nu} = \frac{60^{-3}}{1.6 \times 10^{-19} * 1.9} = 2.0 \times 10^{17}$$

57. Lallemand, P. and Simova, P., J. Molec. Spectro. 26, 262 (1968).

Again, assuming one can convert 1/2 of the photons available, then

$$N^* \text{ Vol} \sim 1.0 \times 10^7 \text{ or } N \leq 3.2 \times 10^{20} \text{ cm}^{-3},$$

Therefore,

$$N^* \text{ Vol} = N^* \frac{\pi^2 w^4}{\lambda} = 1 \times 10^{17}$$

or

$$\log N^* + 4 \log w = 11.8$$

This equation is also plotted on Figure 20. It shows that to achieve 10 percent excitation into $v = 1$, the beam waist must be significantly tighter than for the H_2 case, i.e., $w = 0.12 \text{ mm} = 0.012 \text{ cm}$. This corresponds to a Rayleigh range of $\sim 7 \text{ cm}$ and an irradiated volume of $\sim 3 \times 10^{-3} \text{ cm}^3$.

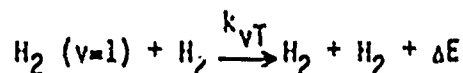
Conversely, the orifice diameter appropriate for 10 percent excitation in H_2 will achieve only ~ 0.7 percent excitation in N_2 . For this regime, the effective focal length would be near 150 cm f.l. The tight focusing condition would correspond to intensities of near $4 \times 10^{10} \text{ W/cm}^2$ which may prove experimentally troublesome. For the conditions used in the H_2 example, we have N_2 pressure = 13 atm. For a beam diameter of 0.8 mm, $\text{N}_2(v=1)/\text{N}_2 = 0.7$ percent or $\text{N}_2(v=1) = 69 \text{ torr}$. Assuming a flow velocity which is sonic ($v = 4.2 \times 10^4 \text{ cm/sec}$) and these experimental conditions, one would anticipate a flux of $9.4 \times 10^{22} \text{ cm}^{-2} \text{ sec}^{-1}$ which significantly exceeds the task requirements.

We will now consider the various experimental system constraints, having demonstrated, at least in principle, that we can generate the needed densities and flux at high fractional excitation ratios using realistic laser pumps for both H_2 and N_2 .

3. System Parameters (Using H_2 as an Example)

Since these lasers have pulse lengths of near 10 nsec the resulting flux of vibrationally excited H_2 exiting from the 0.8 mm orifice will have a finite on-time. Beam duration times will be constrained as a result of the influence of a number of potentially limiting factors, such as flow time, and vibration to translation (V-T) relaxation processes in the gas phase as well as on the nozzle walls.

For our experimental conditions, we anticipate the production of 10 percent excitation of $v = 1$ H_2 molecules in a "slug" of gas with dimensions of 0.8 mm diameter and ~ 190 cm long moving at near Mach 1 or 1.5×10^5 cm/sec. It will, therefore, take 1.3 msec to flow this "slug" of gas out of the chamber. This flow time can be compared to various potential loss processes also expressed as characteristic times, e.g., consider losses in the degree of excitation due to vibration-to-translation energy transfer processes, i.e.,



where k_{VT} at room temperature has been determined to be $\sim 1.5 \times 10^{-16}$ $cm^3 \text{ sec}^{-1}$ (see Figure 21). This results in a relaxation time of

$$\tau_{VT} = \{k_{VT} [H_2]\}^{-1} = 33 \text{ msec}$$

which is long compared to the flow time, so little de-excitation due to relaxation in the gas phase is expected.

Another consideration is relaxation at the walls. Diffusion to the walls can be of two forms: mass transport and excitation transport. With regard to mass diffusion, a diffusion time is given by

$$\tau_D = \frac{w^2}{D} = \frac{(0.04)^2}{1.243} \times \frac{6}{760} = 0.01 \text{ msec},$$

which is very fast compared to the flow time so the potential for de-excitation is significant. Alternately, energy changing collisions may provide a mechanism for even more rapid transport of vibrational excitation to the walls. Studies have been done by Kovacs, and Javan⁽⁵⁸⁾ for $CO_2(001)$ diffusion in CO_2 with the result that diffusion was found, in fact, to be slower due to the effective larger cross section involved. Therefore, regardless of the diffusion mechanism, $H_2(v=1)$ molecules will suffer tens of collisions with the nozzle wall before exiting. At issue then is the likely effect of the wall for deactivation. Studies by Heidner and Kasper⁽⁵⁹⁾ on vibrational relaxation of $H_2(v=1)$ also provided an upper limit on the

58. Kovacs, M.A., Ph.D. Thesis, (Massachusetts Institute of Technology, 1969).

59. Heidner, R.F. and Kasper, J.V.V., Chem. Phys. Lett. 15, 179 (1972).

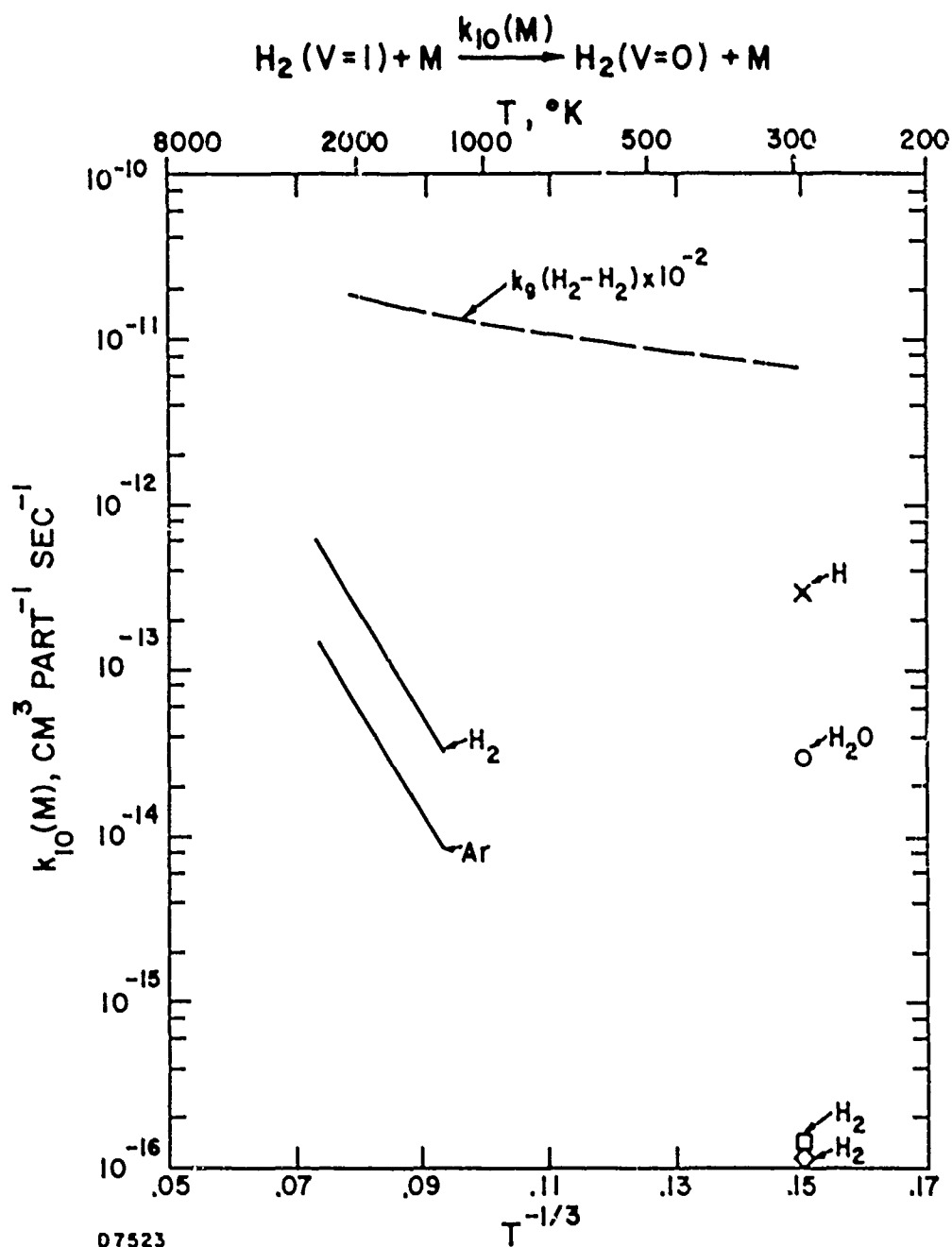


Figure 21 Experimentally Derived Rate Constants, $k_{10}(\text{M})$ as a Function of Temperature T for Deactivation of H_2 by Various Collision Partners M

probability for deactivation of $H_2(v=1)$ on collisions with pyrex walls. They found this limit to correspond to a probability constant which corresponds to many thousands of encounters. This suggests that once formed (essentially instantaneously by the laser pulse), the H_2 metastable molecules may suffer numerous wall collisions before exiting the nozzle, but with little loss in excitation either from gas phase or wall encounters. This fixes the flow time to repetition frequency as the duty cycle or on-time of the metastable beam.

The commercial Lumonics laser which we have used in performing our sample calculations can pulse at 10 pps, which allows a duty cycle of about 1 percent, however, 100 to 1000 Hz devices have been built for isotope separation applications⁽⁶⁰⁾ and, therefore, are conceptually reasonable to consider. A 500 Hz laser would give a duty cycle of > 50 percent.

4. Limiting Assumptions

All of the above discussion has considered the excitation laser sources to be flat top temporal pulses of diffraction limited beam quality. Clearly, this is an idea that is difficult to achieve experimentally. This will cause these projections to be modified to some extent. The fact that significantly greater flux is projected than our original objective gives us confidence that such a high flux is not totally unrealistic. If achieved, it would represent a considerable advance in the current state of the art.

We have also defined our flux at the exit port of the nozzle. Clearly, a "beam" exiting a small diameter (0.8 mm) nozzle with a driving pressure of 6 torr will expand and form a classic supersonic expansion jet. Depending on the application, one may have to consider skimmers to redefine the beam at some distance from the exit nozzle with a subsequent reduction in flux through the skimmer's entrance orifice. An entire literature has developed devoted to understanding and characterizing these phenomena and detailed calculations are outside the scope of this program. Several studies at similar pressures and nozzle diameters have been done and the reader is referred to these literature sources.⁽⁶¹⁾

60. Pike, C., Avco Everett Research Laboratory, Inc. (private communication).

61. See, for example, "Rarefied Gas Dynamics, edited by R. Campargue (Paris, 1979) and References therein.

Other potential limiting issues which we have not fully evaluated include: gas breakdown, plasma formation due to laser nozzle interactions, and clustering phenomena. We do not expect gas breakdown to be an issue in the H_2 example in that the laser beams (total energy of 80 mJ in 8 nsec focused to 0.8 mm diameter) are focused to near 2 GW/cm^2 . This is below the breakdown⁽⁶²⁾ of H_2 and the intensity will (in principle) never be achieved since these beams will be efficiently converted to H_2 excitation. However, surface breakdown due to laser irradiation at solid/gas interfaces is clearly to be avoided, since we could expect plasma formation for these same conditions. This requires a suitable alignment procedure to insure the laser light propagates on axis centrally down the nozzle. A trade off of nozzle to laser beam diameter may be necessary to avoid these difficulties or one may consider going to longer wavelengths (e.g., Ruby, doubled yag) to reduce the potential for plasma formation.⁽⁶²⁾

Also, since the gas expands on exiting the nozzle, one may have the potential for hydrogen cluster formation, i.e., $(H_2)_n$; however, studies⁽⁶³⁾ to investigate the properties of H_2 clusters are typically carried out at source temperatures below 80°K - not the room temperature conditions considered here. Also, the influence of high effective vibrational temperatures in the hydrogen beam (e.g., 10 percent excitation corresponds to $T_v \sim 2600^\circ\text{K}$) should further lessen the likelihood of this formation. In fact, performing such experiments at low source temperatures with and without vibrational excitation would be an interesting fundamental application of this technique.

62. Alcock, A.J., Kato, K. and Richardson, M.C., Optics Communications 6,

63. See, for example, "The Population of $L=0$ and $L=1$ levels, for Ortho-Para (H_2) in an Expanding Jet" by J. Verberne and J. Reuss in Rarefied Gas Dynamics, edited by R. Campargue (Paris, 1979) p. 1049.

5. Other Applications

This technique for producing vibrationally excited molecules has found limited application to date in the literature. The most significant has been the work of Ducuing and co-workers,⁽⁶⁴⁾ whereby the excitation was directly accomplished using a high pressure H₂ cell to generate Stokes radiation followed by the "amplifying cell" or, in more recent work,⁽⁶⁵⁾ generalizing the technique by using two dye lasers pumping N₂ and O₂. In these experiments, fractional populations were purposely kept low, so that the process of interest could be clearly studied, i.e., vibration to translation energy transfer.

This technique has also found application in chemical kinetic studies designed to evaluate the effect of vibrational energy in overcoming chemical barriers, e.g., the reaction



was investigated⁽⁶⁶⁾ using this technique to ascertain if localized vibrational energy was effective in overcoming the > 25 kcal/mole activation energy.

It is easy to envision other reactions with applications in isotope separation, chemiluminescence studies, lasers and astrophysics.

64. Ducuing, J., Joffrin, C. and Coffinet, J.P., Optics Comm. 2, 245 (1970).

65. Frey, R., Lukasik, J. and Ducuing, J., Chem. Phys. Lett. 14, 514 (1972).

66. Bauer, S.H., Lederman, D.M., Resler, E.L. and Fisher, E.R., Int. J. Chem. Kinetics 5, 93 (1973).

B. OPTICAL PUMPING METHODS FOR THE PRODUCTION OF HIGH DENSITY, HIGH-SELECTIVITY METASTABLE SOURCES

1. Introduction

The basic concept is to use several optical pumping sources (i.e., fluorescence sources, lasers, or combinations of both) to access metastable levels of atoms initially in the ground state. Optical pumping has the advantage of being a selective excitation method, as opposed to discharge or e-beam excitation, in which the free electrons, as well as other transient species formed during the pumping process, tend to destroy the metastables.

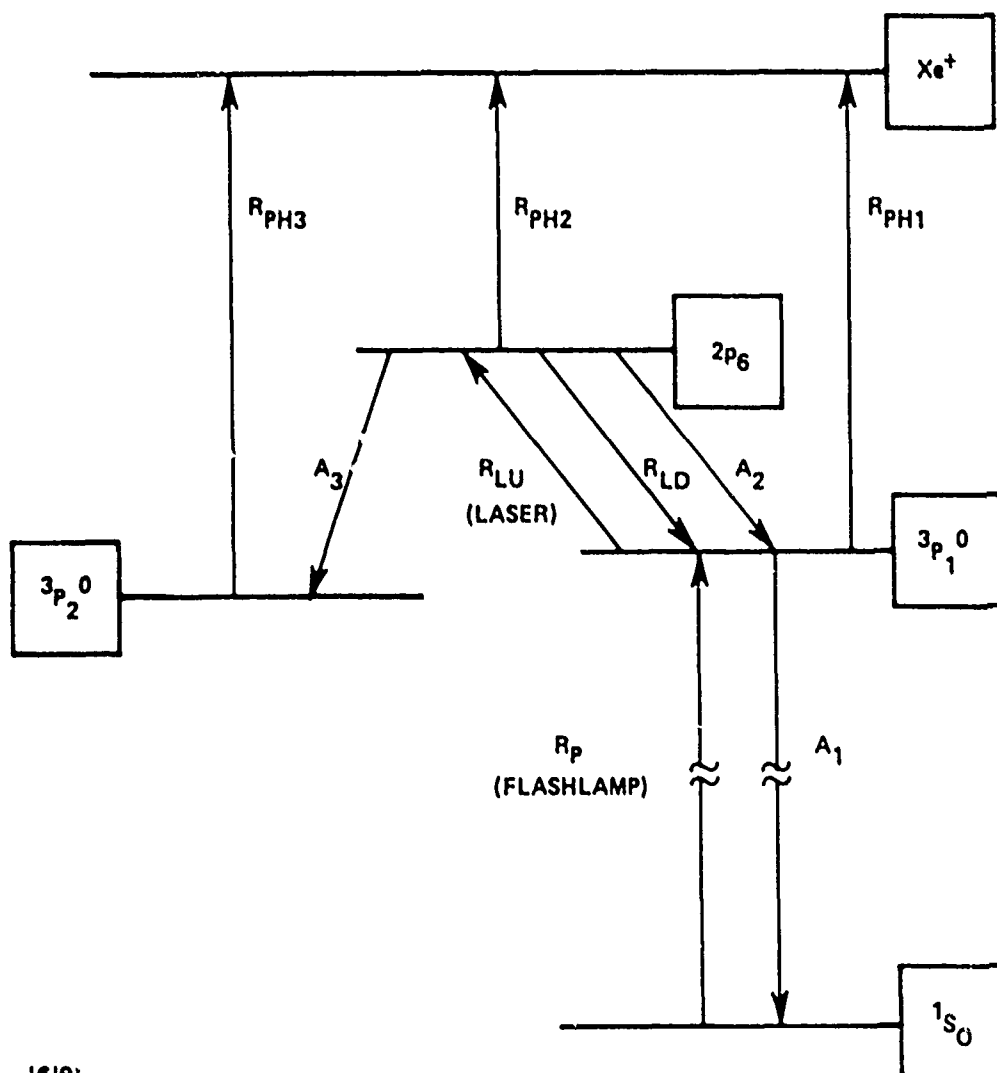
The metastable rare gases are of particular interest both to basic kinetics studies as well as to the physics of high-power lasers (e.g., the rare gas-halides). Unfortunately, even the lowest of the metastable rare gas energy levels, the $\text{Xe}^*(^3\text{P}_2^0)$ with an excitation energy of 8.3 eV, is out of reach of existing tunable lasers. We have, therefore, devised a combined flashlamp + laser optical pumping scheme to produce a beam of metastable xenon at typically $[\text{Xe}^*] \sim 10^{12} \text{ cm}^{-3}$ and with a selectivity (i.e., percent of metastables relative to ground-state atoms) of ~ 10 percent. It should be noted that such a metastable source would be well beyond the existing state of the art.

Atomic krypton at a pressure of ~ 1 -2 atm, pumped by a high-energy (~ 450 kV), intense ($\sim 20 \text{ A/cm}^2$) e-beam, emits a strong UV band centered at $\lambda \sim 1460 \text{ \AA}$ and with FWHM $\sim 138 \text{ \AA}$; this radiation is attributed to the Kr_2^* excimer.^(67,68) The present scheme is to use this Kr_2^* source as a "flashlamp" to pump the Xe resonance line at $\lambda = 1470 \text{ \AA}$. The energy levels of atomic Xe and the important kinetic processes are shown schematically in Figure 22. Briefly, the ground state Xe ($5\text{p}^6\text{ }^1\text{S}_0$) atoms are excited by the Kr_2^* flashlamp to the $\text{Xe}^*(5\text{p}^5\text{6s } ^3\text{P}_1^0)$ resonance level. These excited atoms are subsequently transferred with a tunable laser to one of the ten $\text{Xe}^*(5\text{p}^5\text{6p})$ states the (" 2p_6 " level is preferred) and then spontaneously decay to the metastable $\text{Xe}^*(5\text{p}^5\text{6s } ^3\text{P}_2^0)$ state, which has a natural lifetime⁽⁶⁹⁾

67. Hoff, P.W., Swingle, J.C., and Rhodes, C.K., Appl. Phys. Lett. 23, 245 (1973).

68. Duzy, C. and Boness, M.J.W., IEEE JQE 16, 640 (1980); Boness, M.J.W. and Duzy, C., "Development of Rare Gas Photolytic Drivers," Final Technical Report, Dec. 1979; private communication.

69. Small-Warren, N.E. and Chiu, L.Y.C., Phys. Rev. A11, 1777 (1974).



J6191

Figure 22 Energy Level Diagram and Processes Relevant to Model Calculation of Xe ($3p_2^0$) generation

of ~ 150 sec. The various processes indicated in Figure 22 will be discussed in detail below.

A conceptual view of the apparatus is shown in Figure 23. It consists of a coaxial arrangement, with an outer cell filled with Kr at ~ 1 -2 atm pressure and inner cell, made of MgF_2 to pass the 1470 \AA radiation, containing the Xe beam at a density $\sim 10^{13} \text{ cm}^{-3}$ and with a beam diameter $\sim 1 \text{ mm}$. The laser radiation propagates along the axis of the inner cell. A transverse e-beam irradiates the Kr in the outer cell, forming the Kr_2^* excimer, which then optically pumps the Xe in the inner cell, as described above. A similar system (without the tunable laser) exists at AERL, and has yielded a measured⁽⁶⁸⁾ fluence of $\sim 100 \text{ mJ/cm}^2$ impinging upon the central tube with a pulsewidth of $\sim 1 \text{ \mu sec}$, giving a pump power of $I \sim 10^5 \text{ W/cm}^2$ in the Kr_2^* band of interest. This is clearly a very intense "flashlamp," and is well-suited for our purposes. One caveat to be interjected at this point is that krypton gas usually contains trace amounts of xenon as an impurity. This is clearly intolerable for the present scheme, since the xenon resonance line would absorb just that portion of the Kr_2^* band that is needed to pump the coaxial Xe beam. It is, therefore, necessary to obtain pure (i.e., Xe-free) krypton. Should this not be technically feasible, the present calculations can be regarded as a generic example of an optically-pumped metastable source, illustrating the relevant principles and constraints.

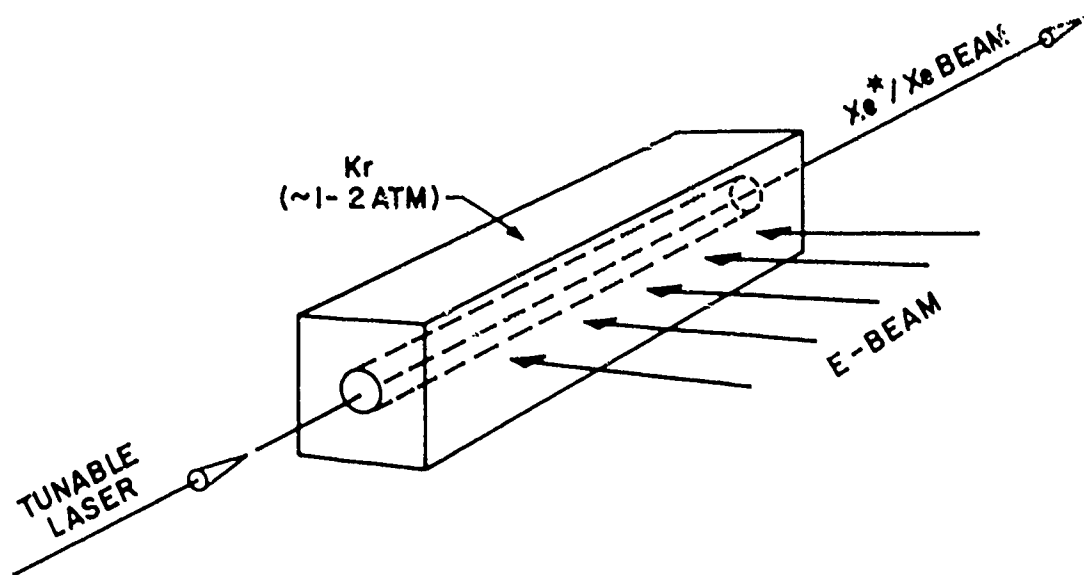
2. Results and Discussion

a. Optical Pumping Rates

We now consider in more detail the optical pumping scheme shown in Figure 22. In order to model the system we must first calculate the parameters indicated in the figure.

We begin with the Kr_2^* flashlamp pumping rate, R_p . At the densities of interest, the Xe resonance line is Doppler broadened, with a FWHM given by

$$\Gamma_D = \frac{2\tilde{\nu}}{c} \sqrt{2 \ln 2 \frac{kT}{M}} = 0.073 \text{ cm}^{-1} \quad (10)$$



J6189

Figure 23 Schematic Layout of Optical Excitation Source

The oscillator strength of the $\text{Xe}(^1S_0 \rightarrow ^3P_1^0)$ resonance transition is ⁽⁷⁰⁾
 $f \approx 0.22$, giving an absorption cross section at line center of $\sigma_0 = 2.5 \times 10^{-12} \text{ cm}^2$. In order for the pump photons to be effectively absorbed, we must have the optical depth $\sigma_0 [\text{Xe}] r > 1$. Taking a beam radius of $r = 0.5 \text{ mm}$ gives $[\text{Xe}] > 8 \times 10^{12} \text{ cm}^{-3}$. To obtain high metastable selectivity and reasonably uniform deposition, we take $[\text{Xe}] = 10^{13} \text{ cm}^{-3}$. It is of interest at this point to compare the total number of Xe atoms with the total number of pump photons. The pump flux is $I = 10^5 \text{ W/cm}^2$ incident on the beam, giving $\phi_p = I_p/h\nu = 7.4 \times 10^{22} \text{ photons/sec-cm}^2$. However, the total pump bandwidth is 138 \AA or $\Gamma_p = 6.5 \times 10^3 \text{ cm}^{-1}$, while only those photons within approximately the Doppler width will be effectively absorbed. Thus, the "useful" pump flux is only

$$\phi'_p = \phi_p \left(\frac{\Gamma_D}{\Gamma_p} \right) = 8.3 \times 10^{17} \frac{\text{photons}}{\text{sec-cm}^2} \quad (11)$$

corresponding to $I'_p = 1.1 \text{ W/cm}^2$. We are, therefore, only utilizing $\sim 10^{-5}$ of the available pump intensity due to bandwidth limitations. The total number of useful photons per unit length of the beam is then given by

$$n'_p = \phi'_p \tau_{\text{pulse}} (2\pi r) = 2.6 \times 10^{11} \text{ photons/cm}, \quad (12)$$

while the total number of ground-state Xe atoms per unit beam length is

$$N_{\text{Xe}} = [\text{Xe}] (\pi r^2) = 7.8 \times 10^{10} \text{ atoms/cm}. \quad (13)$$

70. Ganas, P.S. and Green, A.E.S., Phys. Rev. A4, 182 (1971), and references contained therein.

The number of pump photons available is therefore sufficient to bleach the Xe atoms; however, the pump rate and pulsewidth are such that bleaching does not occur (see below). The pump rate is given by

$$R_p = \int_{-\infty}^{\infty} \sigma \frac{\phi_p}{\Gamma_p} d\tilde{\nu} \approx \frac{\phi_p}{\Gamma_p} \int_{-\infty}^{\infty} \sigma d\tilde{\nu} = \frac{\phi_p}{\Gamma_p} \pi r_e f = 2.3 \times 10^6 \text{ sec}^{-1} \quad (14)$$

where $r_e = 2.818 \times 10^{-13}$ cm is the classical electron radius and all of the other quantities have been defined earlier. Finally, knowing f , we can calculate A_1 , the spontaneous decay rate, from

$$A_1 = \frac{8\pi^2 r_e c}{\lambda^2} \frac{g_1}{g_2} f = 2.3 \times 10^8 \text{ sec}^{-1} \quad (15)$$

The next step is to consider the transfer of excitation from the $\text{Xe}^*(^3\text{P}_1^0)$ resonance level over to the $\text{Xe}^*(^3\text{P}_2^0)$ metastable state. As discussed briefly in the Introduction, this is accomplished via one of the ten $\text{Xe}^*(5\text{p}^5 6\text{p})$ levels with a tunable laser. The particular choice of $5\text{p}^5 6\text{p}$ level involves selection rules, branching ratios, and transition rates. The 2p_6 state (see Ref. 71 for notation) appears to be ideal: it has branching ratios of 0.7 to the $^3\text{P}_2^0$ state, 0.3 to the $^3\text{P}_1^0$ state, and no branching to any other level.⁽⁷²⁾ The transition wavelengths, A-factors (A_2 and A_3 of Figure 22) and absorption oscillator strengths are tabulated below:⁽⁷²⁾

71. Moore, C.E., Atomic Energy Levels, U.S. Nat. Bur. Stand. Circ. No. 467 (U.S. Dept. of Commerce, Washington, D.C., 1949), Vol. III.

72. Setser, D.W., private communication.

<u>transition</u>	<u>$\lambda(\text{\AA})$</u>	<u>$A(\text{sec}^{-1})$</u>	<u>f</u>
$2p_6 - {}^3p_1^0$	8952	9.6×10^6	0.12
$2p_6 - {}^3p_2^0$	8232	2.2×10^7	0.13

Assuming the two transitions to be Doppler-broadened, the relevant cross sections are $\sigma_0({}^3p_1^0 \rightarrow 2p_6) \approx \sigma_0({}^3p_2^0 \rightarrow 2p_6) \approx 8.3 \times 10^{-12} \text{ cm}^2$. In order to obtain high selectivity, we would like the $2p_6 \rightarrow {}^3p_2^0$ transition to be optically thin, so that the metastable state acts as a true excitation sink. Consistent with this picture, we have neglected reabsorption of the 8232 Å photons in our model (see Figure 22). The requirement that the 8232 Å transition be optically thin leads to a constraint on the metastable density: $\tau_0 = \sigma_0[\text{Xe}^*({}^3p_2^0)]r < 1$, giving $[\text{Xe}^*({}^3p_2^0)] < 2.4 \times 10^{12} \text{ cm}^{-3}$. Finally, the rate for laser excitation, R_{LU} , is given by

$$R_{LU} = \sigma_0({}^3p_1^0 \rightarrow 2p_6) \frac{I_L}{h\nu_L} = 3.7 \times 10^7 I_L \text{ sec}^{-1} \quad (16)$$

where I_L is the intensity in W/cm^2 of the tunable laser at 8952 Å. The reverse rate, R_{LD} , is given by detailed balance to be $R_{LD} = 2.2 \times 10^7 I_L (\text{sec}^{-1})$.

The remaining processes involve photoionization from the excited states due to the short-wavelength Kr_2^* pump radiation. It should be noted that photoionization involves a broadband continuum as the final state, so that the entire pump bandwidth is effective in this case, as opposed to the resonance line absorption process which utilized only $\sim 10^{-5}$ of the pump bandwidth. Fortunately, the photoionization cross sections from the $\text{Xe}^*({}^3p_1^0)$ and $\text{Xe}^*({}^3p_2^0)$ levels are very small at the wavelength of interest,⁽⁷³⁾ with $\sigma_{\text{PH}}({}^3p_1^0) \approx \sigma_{\text{PH}}({}^3p_2^0) \approx 3 \times 10^{-20} \text{ cm}^2$, giving

73. Duzy, C. and Hyman, H.A. Phys. Rev. A22, 1878 (1980).

$$R_{PH1} \approx R_{PH3} = \sigma_{PH} \phi_p \approx 2.2 \times 10^3 \text{ sec}^{-1} \quad (17)$$

The value⁽⁷³⁾ for $\sigma_{PH}(2p_6) \approx 10^{-18} \text{ cm}^2$, gives $R_{PH2} \approx 7.4 \times 10^4 \text{ sec}^{-1}$.

b. Modeling Calculations

We have numerically modeled the system shown in Figure 22 using the rates derived above. In Figure 24 we have plotted the metastable density normalized to the initial ground-state density as a function of I_L , the intensity of the tunable laser. The fractional metastable density "saturates" at a value of 0.26 (i.e., bleaching does not occur, as indicated earlier). Starting with an initial Xe density of $[Xe]_0 = 10^{13} \text{ cm}^{-3}$, this gives a maximum metastable density of $2.6 \times 10^{12} \text{ cm}^{-3}$. However, from our earlier arguments, we required $[Xe^*(^3P_2^0)] < 2.4 \times 10^{12} \text{ cm}^{-3}$ for the transition to be optically thin. Thus our model, neglecting reabsorption, is only valid at the lower fractional excitation values. A realistic expectation would be a fractional density of $[Xe^*(^3P_2^0)]/[Xe]_0 \approx 0.1$ giving a metastable density of about 10^{12} cm^{-3} . This would require $\sim 1 \text{ W/cm}^2$ of $\lambda = 8952 \text{ \AA}$ laser intensity over a 1 μsec pulsewidth. We may, however, require somewhat more intensity if the laser cannot be narrowed to the Doppler width of the 8952 \AA transition, which is $\sim 0.01 \text{ \AA}$.

In order to test the sensitivity of the results to the Kr_2^* pump intensity, I_p , we have repeated the modeling calculations for the case $I_p = 5 \times 10^4 \text{ W/cm}^2$ (i.e., one-half of the original value given in Section IV-B-2-a). The results are shown in Figure 24. In this case the fractional metastability "saturates" at 0.14, as compared to the earlier value of 0.26. In general, the magnitude of $[Xe^*(^3P_2^0)]/[Xe]_0$ for comparable laser intensity, I_L , is seen to be approximately proportional to the value of the Kr_2^* pump flux.

In order to calculate the linewidth for the Xe resonance transition [Eq. (10)], we used the Doppler velocity $\langle v_D \rangle = \sqrt{2kT/M}$, with $T = 300^\circ\text{K}$ as the source temperature. For a collimated atomic beam, however, we may have $\langle v_{axial} \rangle \approx \langle v_D \rangle$, but $\langle v_{transverse} \rangle \ll \langle v_D \rangle$. This would lead to a very narrow line in the case of transverse optical pumping with a coherent (i.e., laser) source, where the relevant parameter is $\langle v_{transverse} \rangle$. For an incoherent (i.e., flashlamp) optical pump, however, the photons impinge upon the

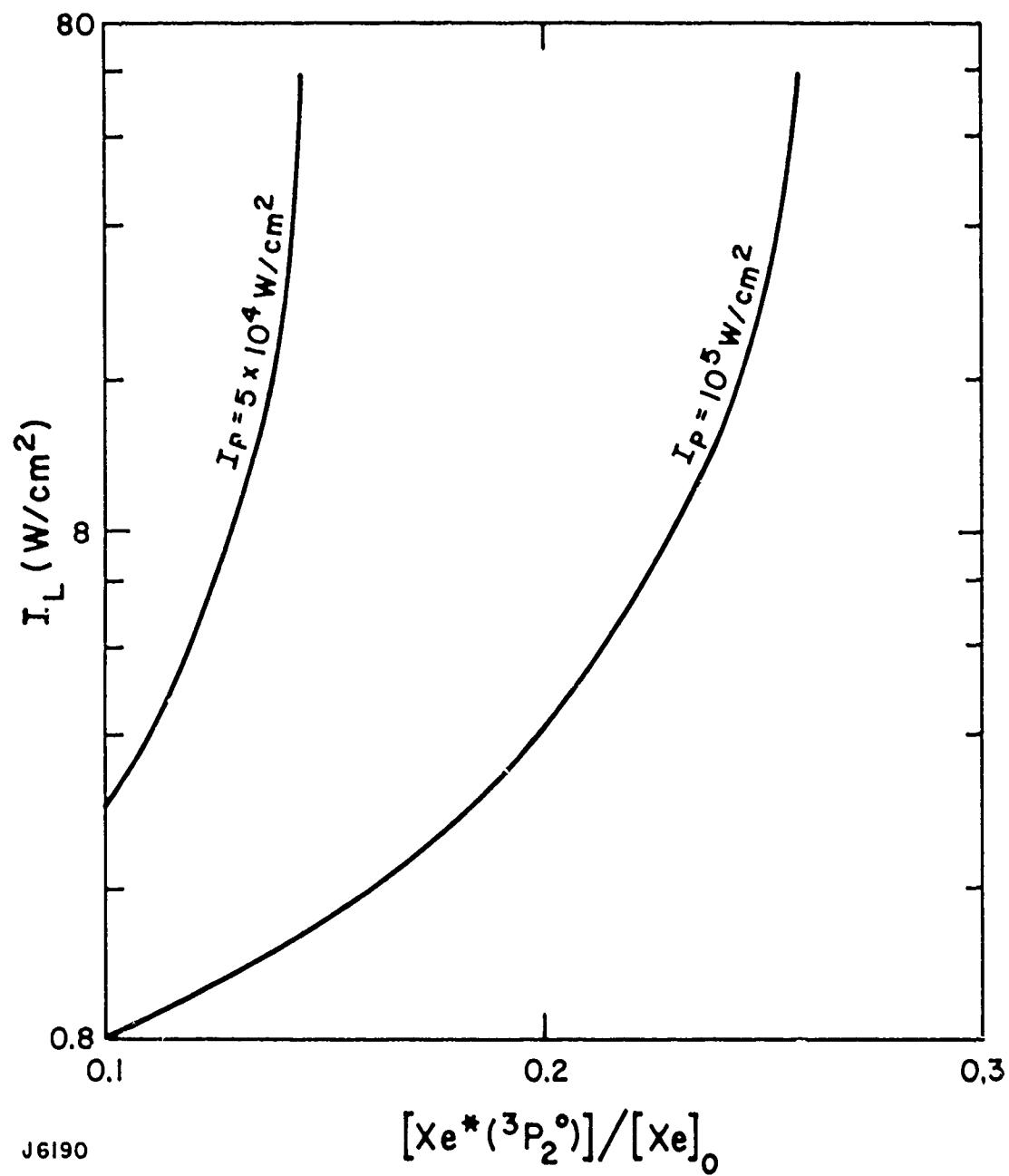


Figure 24 Model Calculation of $\text{Xe} (^3\text{P}_2^0)$ Production as a Function of Laser Intensity

beam at all angles and therefore utilize the axial component of the velocity as well as the transverse component. An accurate calculation would require a convolution of the spatial photon distribution for the particular geometry of interest with the velocity distribution of the atomic beam. For the flashlamp pumping case considered here, we do not expect this effect to significantly alter our results or conclusions.

3. Conclusions

We have shown that the flashlamp + laser optical pumping scheme under consideration should be capable of producing a metastable xenon beam, with metastable density $\sim 10^{12} \text{ cm}^{-3}$ and selectivity of ~ 10 percent. This represents a large improvement over the current state of the art. The principal constraint on extending the scheme to higher densities is the broad bandwidth of the Kr_2^* fluorescence pump relative to the narrow absorption bandwidth of the Xe atomic resonance line. From formula (12), we found that the number of useful pump photons was $n'_p = 2.6 \times 10^{11}$ photons/cm of beam length, which corresponds to a density of 3.3×10^{13} photons/cm³. Thus, even if there were no losses in the system whatsoever, so that every pump photon yielded a metastable atom, we could still only achieve a metastable density of $\sim 3 \times 10^{13}$ atoms/cm³. Generally, fluorescence pump sources do not have the intensity per unit bandwidth to achieve extremely high metastable densities (i.e., $\sim 10^{16} \text{ cm}^{-3}$).

As indicated in the Introduction the present scheme for accessing high-lying metastable energy levels, which are typically out of the range of existing tunable lasers, should be generally applicable to a variety of systems. For example, the Ar_2^* excimer emission band overlaps the krypton atomic resonance line,⁽⁷⁴⁾ while the $\text{XeI}^* \Sigma \rightarrow \Sigma$ band overlaps the mercury 2537 Å resonance transition.⁽⁷⁵⁾ In fact, at AERL we have used a coaxial, e-beam pumped device, of the type shown in Figure 23, to produce $[\text{Hg}^*] > 5 \times 10^{14} \text{ cm}^{-3}$ optically pumped by the XeI^* fluorescence band.⁽⁷⁵⁾ Detailed modeling for these, and perhaps other cases, could be carried out in a similar fashion to the xenon case.

74. Wrobel, W.G., Rohr, H. and Steuer, K.H., Appl. Phys. Lett. 36, 113 (1980).

75. Mandl, A. and Hyman, H.A., J. Chem. Phys. 74, 3167 (1981).

Finally, it should be noted that although the Kr_2^* "flashlamp" produces a fluorescence intensity $\sim 10^5 \text{ W/cm}^2$, only $\sim 1 \text{ W/cm}^2$ is useful (i.e., within the absorption bandwidth). It may therefore be worthwhile to examine the possibility of utilizing an intense, but unreversed, xenon resonance lamp to accomplish the "flashlamp" pumping step. Using a coaxial xenon lamp in place of the e-beam pumped Kr_2^* source would greatly simplify the apparatus, and may therefore be desirable even at the sacrifice of some metastable density. Similarly, intense resonance lamps might also be useful for the krypton and mercury examples cited above. The operating characteristics of these sources are described in the next section along with a laser based method for the generation of 1470° \AA xenon resonance radiation via a four wave mixing technique in magnesium vapor.

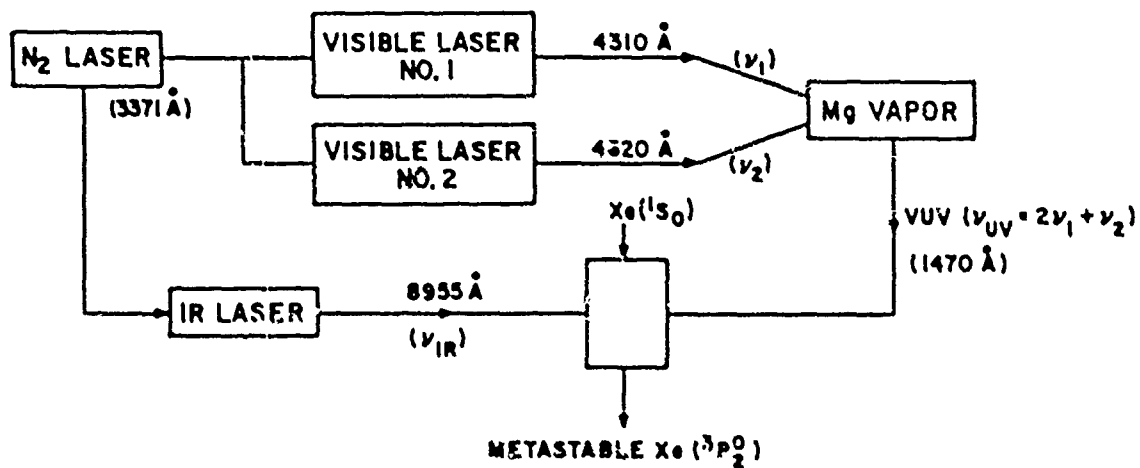
4. Other Methods for Generating Vacuum Ultraviolet (VUV) Radiation

a. VUV Generation by Four-Wave Mixing

We wish to transfer a sizeable fraction of a ground-state ($^1\text{S}_0$) xenon beam into the metastable $^3\text{P}_2^0$ level. We have established that this may be done by optically pumping the Xe atoms with two light sources of frequency 68045.7 cm^{-1} (1469.6 \AA vacuum wavelength) and 11167.3 cm^{-1} (8954.7 \AA wavelength), respectively. We propose that both sources be pulsed, that the IR source be a dye laser, and that the VUV be generated by four-wave mixing of two dye lasers.

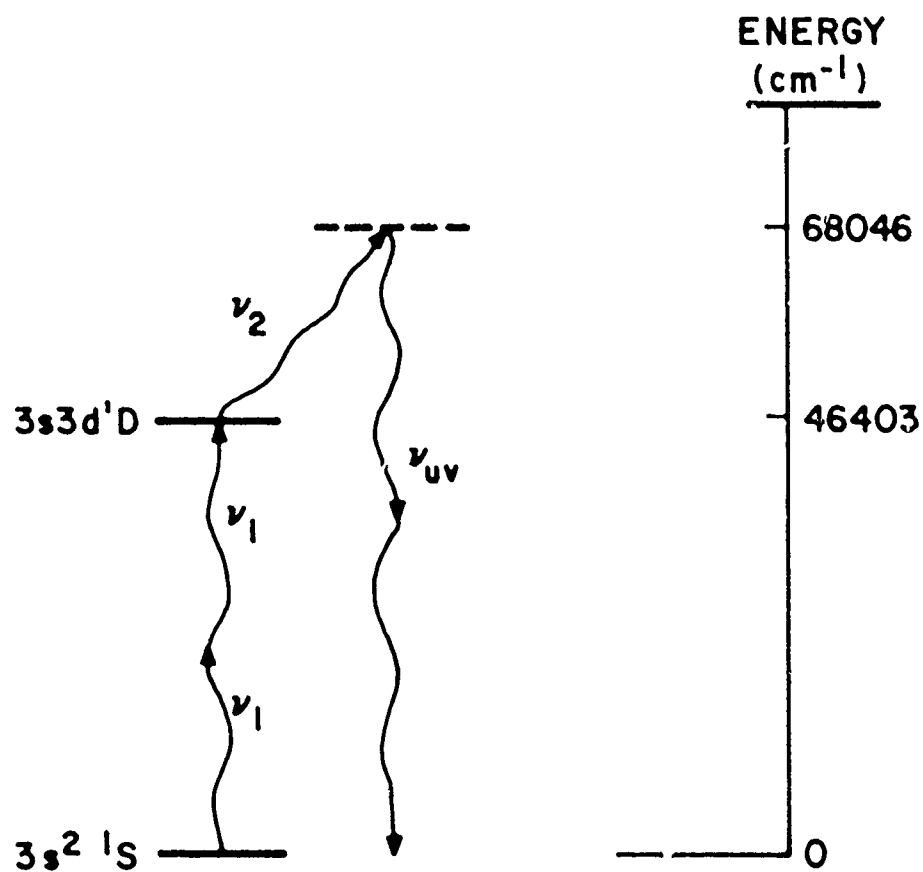
A schematic of our proposed metastable generator is shown in Figure 25. A pulsed N_2 laser simultaneously pumps three dye lasers of vacuum wavelengths 8955, 4310 and 4620 \AA , respectively. (Alternatively the pump can be a frequency-doubled and tripled Nd-YAG laser.) The visible lasers are mixed in a cell containing ~ 10 torr of Mg vapor and He buffer gas; with the wavelength of one laser (4310 \AA) tuned to a two-photon resonance of atomic Mg, the wave mixing is enhanced and efficient production of the VUV (at the sum frequency $2\nu_1 + \nu_2$) will occur (see Figure 26). 1470 \AA VUV production by this technique was reported in 1975 by Wallace and Zdasiuk,⁽⁷⁶⁾ These authors

76. Wallace, S. and Zdasiuk, G., Appl. Phys. Lett 28, 449 (1976).



K3728

Figure 25 Generation of a Pulsed Beam of Metastable Xe Atoms Using Four-Wave Mixing in Mg Vapor



K3725

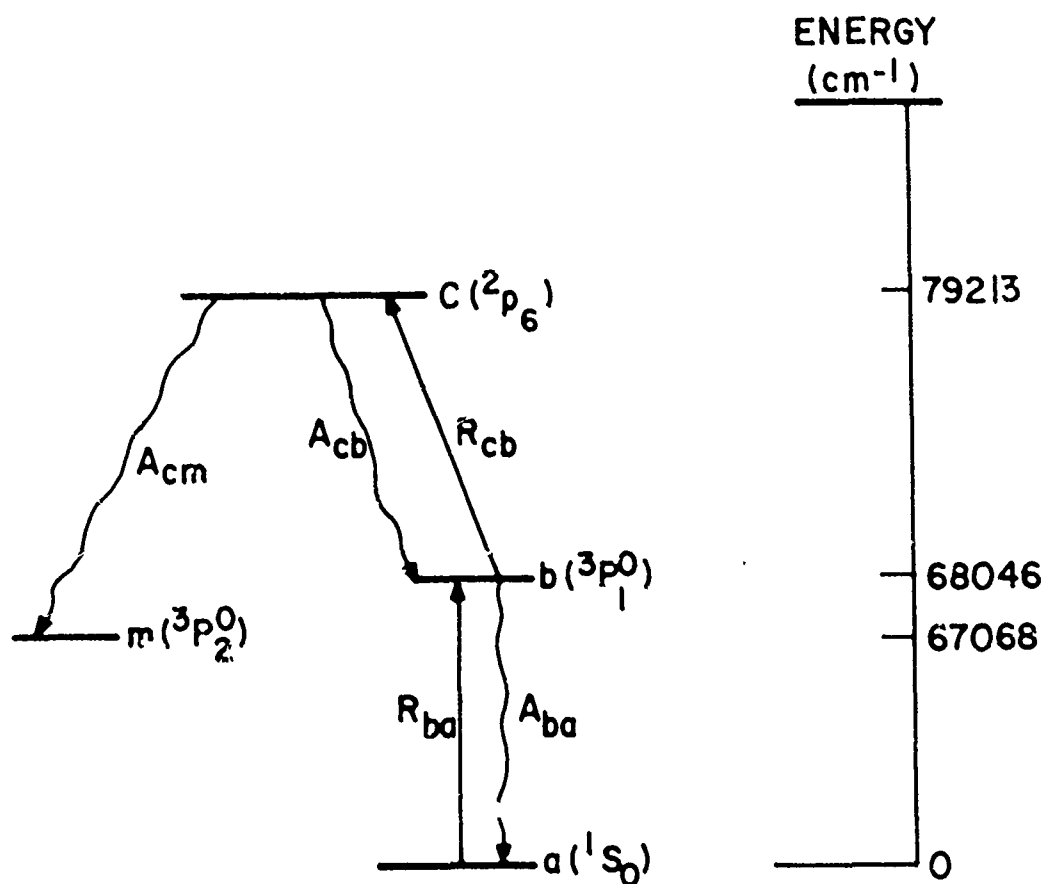
Figure 26 Energy Levels of Atomic Mg Relevant to Four-Wave Mixing VUV Generation. The Dye Laser Frequencies are Labeled ν_1 and ν_2 ; $\nu_{UV} = 2\nu_1 + \nu_2$

reported a conversion efficiency (ν_1 to ν_{VUV}) of ~ 0.1 percent for peak dye laser powers of 50 kW (in a ~ 7 -nsec pulse) and dye laser spectral widths of $\sim 0.1 \text{ cm}^{-1}$. Because of pulse narrowing which is inherent in wave mixing of this type, we can expect to generate a 3-nsec-wide, 50 W peak-power VUV pulse, corresponding to a VUV energy of $\sim 0.15 \text{ }\mu\text{J}$ in a spectral width of 0.3 cm^{-1} . This can be easily focused into an Xe beam to give a fluence of 10 J/cm^2 , a fluence which is sufficient to saturate the Xe $^1\text{S}_0$ - $^3\text{P}_1^0$ transition (see Section IV-B-5). The VUV pulse is timed to coincide with the center of the 7-nsec IR pulse ($8955 \text{ }\text{\AA}$) in the region of their spatial overlap. Thus, the Xe atoms excited up to the $^3\text{P}_1^0$ state will tend to be excited by the IR laser to the 2p_6 level if the IR laser spectral intensity ($\text{W/cm}^2 \text{ GHz}$) is sufficiently large to make the $^3\text{P}_1^0$ - 2p_6 transition rate R_{cb} much greater than the rate A_{ba} ($= 2.3 \times 10^8 \text{ s}^{-1}$) at which the $^3\text{P}_1^0$ level decays spontaneously (Figure 27). The required IR spectral intensity is a relatively modest $80 \text{ W/cm}^2 \text{ GHz}$, which is easily achievable in a pulsed dye laser, (see Section IV-B-5). Because of the favorable branching ratio, most of the 2p_6 atoms decay spontaneously to the metastable $^3\text{P}_2^0$ level after the light pulses end. Spontaneous decay of the 2p_6 level during the light pulses is negligible.

The metastable generator we have described requires the following hardware: (a) a 1 MW peak-power pulsed N_2 laser, such as the Molelectron UV-1000; (b) three Hansch-type transversely pumped dye lasers, (c) two intracavity dye laser etalons (one in each visible dye laser) to narrow the spectrum to $\sim 0.1 \text{ cm}^{-1}$ and, thereby, enhance the four-wave mixing, (d) a heat-pipe-type oven for atomic Mg (the required temperature is $\sim 850^\circ\text{C}$), (e) various focusing lenses and mirrors, and (f) a VUV-sensitive solar-blind photomultiplier tube. No elaborate VUV spectrometer is required, since the proposed wavelength tuning may be established by observing the fluorescence produced when the VUV beam is incident on a cell containing Xe.

b. Low and High-Pressure VUV Lamps

There are two types of incoherent VUV sources that are currently being considered: a rare gas atomic line source and an excimer emission band source. The atomic line source is a low pressure ($\leq 1 \text{ torr}$), cw, microwave discharge lamp that contains a rare gas that generates the appropriate resonance fluorescence, i.e., a Xe lamp to pump the Xe resonance line, etc. A



K3724

Figure 27 Energy levels of Atomic Xe Relevant To Metastable (state m) Generation. The level Heights (about 0) are not drawn to scale. The R's represent Light Induced Transition Rates, while the A's are Spontaneous Decay Rates. It is seen that the Ratio R_{cb}/A_{ba} determines what fraction of the VUV-Induced Population in level b is transferred to level c. Because of the favorable branching ratio ($A_{cm} \approx 2A_{cb}$), most of the population excited to level c decays to the metastable level m

number of these devices have been built and their characteristics reported in the literature.⁽⁷⁷⁾ Photon fluxes in the range 10^{16} – 10^{17} photons/sec (2×10^{-3} – 2×10^{-2} W/cm² for the Xe resonance radiation) were obtained using a 25 mm diameter LiF window. The relevant VUV fluence can be obtained from the product of the lamp flux and the transit time, t_p , of the atom beam across the lamp window. For thermal Xe beams, $t_p = 115$ μ sec for a 2.5 cm diameter window. Using a mid-range value for the flux, 0.01 W/cm², yields a VUV fluence ~ 1.2 μ J/cm². Assuming that the lamp linewidth is dominated by Doppler broadening at low pressure (~ 0.1 cm⁻¹) yields a spectral fluence ~ 0.4 μ J/cm²-GHz, a value comparable to that required to saturate the resonance line transition (see Section IV-B-5). We recognize that the detailed relative spectral power distribution of the lamp (including self-reversal) will have to be measured to validate this linewidth assumption. This type of measurement requires a very high resolution VUV monochromator ($\Delta\lambda/\lambda \leq 1 \times 10^{-6}$) that is not available in most laboratories. Further investigations will be required to determine if this information is available in the literature.

Broadband Ar₂^{*} (1300–1600 Å) and Kr₂^{*} (1500–1800 Å) excimer emission flashlamps provide alternative continuum VUV sources for pumping Kr and Xe resonance lines, respectively. These sources utilize cold cathode, pulsed discharges ($\tau_{\text{pulse}} \approx 1$ –2 μ sec) at several hundred torr noble gas pressure. This type of excimer flashlamp is more compatible with the types of experiments described here than is the e-beam pumped flashlamp described previously. Although a great deal is known about the relative spectral bandwidth of these sources ($\Delta\lambda \sim 150$ Å FWHM), little information is available concerning absolute spectral power output of these lamps in comparison with the absolute fluorescence efficiencies available for e-beam pumped flashlamps. We estimate that equivalent blackbody temperatures greater than 20,000°K would be required to generate the necessary spectral fluence to saturate the Doppler broadened resonance line transition.

The requirements on the infrared laser pump depend to some extent on the type of incoherent VUV excitation source that will be employed. A cw tuneable dye laser would be required if the low pressure atomic line source is used.

77. Stief, L.J. and Mataloni, R.J., Appl. Optics 4, 1674 (1965).

On the other hand, the pulsed VUV flashlamps would require flashlamp pumped IR dye lasers that have about the same pulsewidth as the VUV flashlamp. Tuneable radiation in the 7000-8000 Å region is required to pump the s-p transitions, $b \rightarrow c$, in Figure 27 with a spectral flux of $\sim 80 \text{ W/cm}^2\text{-GHz}$. There are at least two reports of cw tuneable infrared radiation from krypton ion pumped dye lasers using carbocyanine and oxazine dyes.^(78,79) Tuned output powers in the range 0.1-1.0 W were obtained with a 1 Å linewidths. The required spectral flux ($\sim 100 \text{ W/cm}^2$) can then be obtained by focusing to a 1 mm diameter spot (see Section IV-B-5). Similar results can be expected from flashlamp pumped dye lasers.

5. Calculation of Required VUV Fluence and IR Flux

We wish to calculate the following two quantities: (see Figure 27) (i) the VUV spectral fluence required to saturate the resonance transition, $^1S_0 \rightarrow ^3P_1$ ($A \rightarrow b$) in the rare gases and (ii) the IR spectral intensity required to transfer most of 3P_1 population to the higher p levels ($b \rightarrow c$). Both requirements may be estimated by noting that the transition rate R for a transition of wavelength λ and oscillator strength f induced by a spectral intensity $dI/d\nu$ ($\text{erg/cm}^2 \text{ Hz}$) on resonance is

$$R = \frac{\pi r_e f}{h} \frac{dI}{d\nu}$$

A transition is saturated if $R \tau > 1$, where τ is the laser pulsewidth. Requiring $R_{ba} \tau = 1$ for the $a \rightarrow b$ transition ($\lambda_{ba} = 1.5 \times 10^{-5} \text{ cm}$, $f_{ba} = 0.22$) implies a minimum VUV spectral fluence $dF/d\nu$ of

$$\begin{aligned} \frac{dF}{d\nu} &= \frac{h}{\pi r_e \lambda_{ba} f_{ba}} = 2.3 \times 10^{-9} \text{ erg/cm}^2 \text{ Hz} \\ &= 0.23 \text{ } \mu\text{J/cm}^2 \text{ GHz} \end{aligned}$$

78. Romanek, K.M., Hildebrand, O. and Gobel, E., Opt. Comm. 21, 16 (1977).

79. Donzel, A. and Weisbuch, C., Opt. Comm. 17, 153 (1976).

Similarly, we calculate the minimum spectral intensity of the IR laser from the requirement that $R_{cb} \geq A_{ba}$. To be specific, we require that $R_{cb} = 5A_{ba}$. With

$$\lambda_{cb} = 9.0 \times 10^{-5} \text{ cm}, f_{cb} = 0.12, A_{ba} = 2.3 \times 10^8 \text{ s}^{-1},$$

we obtain

$$\frac{dI_{cb}}{d\nu} = \frac{5h}{\pi r_e \lambda_{cb} f_{cb}} A_{ba} = 0.81 \text{ erg/cm}^2/\text{s Hz}$$

$$= 81 \text{ W/cm}^2 \text{ GHz}$$

C. E-BEAM-SUSTAINED DISCHARGE EXCITATION OF METASTABLE $N_2(A^3\Sigma_u^+)$

The objective of this phase of the program is to assess the feasibility of utilizing an e-beam sustained discharge as a high flux molecular beam source of metastable $N_2(A^3\Sigma_u^+)$ states, hereafter abbreviated A or $N_2(A)$ states. The emphasis in this part of the study is focused primarily on the energy transfer and chemical kinetic modeling aspects of high flux A-state production using a computer kinetics code. The time dependence of $N_2(A)$ states as well as a number of other species is investigated as a function of e-beam current density and electric field strength. We also briefly discuss a method for extracting A-states from the discharge.

The basic idea is to produce A-states by e-beam sustained discharge pumping a high-speed flow (flow speed $\sim 10^4$ cm/sec) of pure N_2 at near atmosphere pressure and then forming a high flux molecular beam source by expanding a small portion of the flow through a supersonic nozzle/skimmer sampling orifice into a high vacuum chamber. Using this technique we believe that an A state flux of at least 10^{19} cm $^{-2}$ sec $^{-1}$ can be obtained at the throat of a sonic orifice for modest energy loadings (30 J/l-atm). Our modeling calculations also indicate much higher flux levels can be achieved at higher energy loadings (500-1000 J/l-atm). However, these results require more detailed kinetic information regarding translational heating rates and temperature dependences of a number of important energy transfer processes before an adequate assessment can be made.

There are two distinct advantages which favor the use of the e-beam sustained discharge over the self-sustained discharge: (1) uniform, volumetric excitation at high gas densities, and (2) independent control over both the secondary electron density and electron energy distribution. The ionization rate is controlled by varying the primary e-beam current while the electron energy is controlled by varying the sustainer electric field strength. In this way, the electron energy distribution can be tailored to efficiently pump the electronic states in N_2 while, at the same time, maintaining a relatively low ionization rate and, therefore, a stable discharge at high pressure.

Our modeling calculations of A-state excitation indicate that the total lifetime of $N_2(A)$ within the discharge zone is of the order of 1 msec.

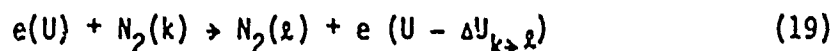
Therefore, the high-speed flow and supersonic nozzle sampler will be required to extract the A-states from the discharge zone and transport them to some other region where their properties can be investigated.

1. Overview of Modeling Calculation

The time dependence of $N_2(A)$ state formation and loss is obtained in a two step calculation. First the AERL Boltzmann computer code is used to obtain steady-state electron energy distributions $f(U)^{S.S.}$ and average electron excitation rate constants, $k_i(E/N)$, at a given value of E/N , the pressure reduced electric field strength. These quantities are related by

$$k_i(E/N) = \int_0^{\infty} dU f(U)^{S.S.} \sigma_i(U) U \quad (18)$$

where $\sigma_i(U)$ is the energy dependent cross section for the i th electron-heavy particle inelastic process:



and where the indices k and l label two N_2 quantum states and ΔU is the energy difference between those two states. The values of k_i for electronic excitation and ionization are then fed into a kinetics code calculation which integrates the coupled set of rate equations that describe all the formation and loss processes included in this model for six species: $N_2(A)$, $N_2(B)$, $N_2(C)$, $N(^4S)$, $N(^2P)$ and electrons that are formed in the discharge. The output of the kinetics computer code is then displayed in the form of computer generated plots of the temporal dependence of the number density of electrons, $N_2(A)$, $N(^4S)$ and $N(^2P)$ states.

2. Boltzmann Code Calculation

By utilizing the two-step calculation described above, we have made the implicit assumption that the time evolution of the secondary electron energy distribution can be completely decoupled from the time evolution of the number densities of the electrons and heavy particles. This approximation is valid in the present set of calculations since the time scale required for the secondary electron distribution to settle down to a steady-state value is much

faster than the time scale for variations in the species number densities in the discharge. Given that the cross section for some of the important electron energy loss processes are in the range $10^{-16} - 10^{-17} \text{ cm}^2$ and that the initial ground state N_2 density is assumed to be 1 amagat ($2.45 \times 10^{19} \text{ cm}^{-3}$), we estimate that the characteristic time for electron energy relaxation is < 1 nsec for 1 eV electrons, whereas it will be shown below that number density variations always occur on much slower time scales.

Table 2 lists the electron energy loss processes included in the AERL Boltzmann Code calculation.⁽⁸⁰⁻⁸⁷⁾ Cross-section values from threshold to 100 eV electron energy were used to describe each process. Experimental energy dependent cross-section data were available for each of these processes except for the three metastable ionization processes from $N_2(A^3\Sigma_u^+)$, $N_2(B^3\Pi_g)$ and $N_2(C^3\Pi_u)$ states and rotational excitation in ground state N_2 . Cross sections for ionization from the A state were taken from the binary encounter calculations of Ion-That and Flannery.⁽⁸⁷⁾ Ionization cross sections from the B and C states⁽⁸⁸⁾ were then scaled from the A state results using the relationships:

$$\sigma_{Bi}(U) = [\sigma_{Ai}(U = (I_B/I_A)U)] (I_A/I_B)^2 \quad (20a)$$

$$\sigma_{Ci}(U) = [\sigma_{Ai}(U = (I_C/I_A)U)] (I_A/I_C)^2 \quad (20b)$$

where I_X and σ_{Xi} are the ionization energy and cross section for each state X (= A, B, and C).

Using this set of cross-section data, Boness⁽⁸⁹⁾ has shown that the calculated values of N_2 drift velocity, characteristic energy and first Townsend ionization coefficients derived from the AERL Boltzmann code are in good agreement with experimental measurements of these quantities for E/N values up to $\sim 6 \times 10^{-15} \text{ V-cm}^2$.

Figure 28 displays the steady-state electron energy distribution at two different E/N values: $4.1 \times 10^{-15} \text{ V-cm}^2$ and $1.02 \times 10^{-15} \text{ V-cm}^2$. The average electron energy $\langle U \rangle$ for each of these distributions is 1.09 and 1.77 eV, respectively, where

87. Ion-That, D. and Flannery, M.R., Phys. Rev. A15, 517 (1977).

88. Hyman, H., Avco Everett Research Laboratory, Inc. private communication.

89. Boness, J., Avco Everett Research Laboratory, Inc. private communication.

TABLE 2
ENERGY LOSS PROCESSES INCLUDED IN AERL BOLTZMANN CODE

<u>PROCESS</u>	<u>ΔU (eV)</u>	<u>Refs.</u>
o Momentum Transfer		
$e_s + N_2 \longrightarrow N_2 + e'_s$	3.918×10^{-5}	80
o Rotational Excitation		
$e_s + N_2(J) \longrightarrow e'_s + N_2(J')$	0.02	81
o Vibrational Excitation		
$e_s + N_2(V=0) \longrightarrow e'_s + N_2(V')$		
$\Delta V = 1$	0.29	82
$\Delta V = 2$	0.58	"
$\Delta V = 3$	0.88	"
$\Delta V = 4$	1.17	"
$\Delta V = 5$	1.46	"
$\Delta V = 6$	1.75	"
$\Delta V = 7$	2.05	"
$\Delta V = 8$	2.34	"
o Electronic Excitation		
$e_s + N_2(X^1 \Sigma_g^+) \longrightarrow e'_s + N_2(A^3 \Sigma_u^+)$	6.17	83
" $\longrightarrow e'_s + N_2(B^3 \Pi_g)$	7.35	"
" $\longrightarrow e'_s + N_2(W^3 \Delta_u)$	7.36	"
" $\longrightarrow e'_s + N_2(B'^3 \Sigma_u^-)$	8.165	"
" $\longrightarrow e'_s + N_2(a'^1 \pi_g)$	8.55	"
" $\longrightarrow e'_s + N_2(W^1 \Delta_u)$	8.895	"
" $\longrightarrow e'_s + N_2(C^3 \pi_u)$	11.03	"
" $\longrightarrow e'_s + N_2(E^3 \Sigma_g^+)$	11.88	"

TABLE 2 (Continued)

<u>PROCESS</u>	<u>ΔU (eV)</u>	<u>Refs.</u>
o Dissociation		
$e_s + N_2(X) \longrightarrow 2N(^4S)$	9.76	84, 85
o Ionization		
$e_s + N_2(X) \longrightarrow N_2^+ + 2e_s$	15.58	86
$e_s + N_2(A) \longrightarrow N_2^+ (A^2\pi_u) + 2e_s$	10.79	87
$e_s + N_2(B) \longrightarrow N_2^+ (A^2\pi_u) + 2e_s$	9.62	this work
$e_s + N_2(C) \longrightarrow N_2^+ (A^2\pi_u) + 2e_s$	5.99	this work

80. Englehardt, A.M., Phelps, A.V. and Risk, C.G., Phys. Rev. 135, A1566 (1964).
81. Chandra, N. and Burke, P.G., J. Phys. B 6, 2355 (1973).
82. Chandra, N. and Temkin, A., Phys. Rev. A 13, 188 (1976) and references cited therein.
83. Cartwright, D.C., Trajmar, J., Chutjian, A. and Williams, W., Phys. Rev. A 16, 1041 (1977).
84. Winters, H.F., Horne, D.E. and Donaldson, E.E., J. Chem. Phys., 41, 2766 (1964).
85. Niehaus, A. and Naturforschung, Z., 22a, 690 (1967).
86. Rapp, D., Briglia, D.D. and Englander-Golden, P., J. Chem. Phys. 42, 4081 (1965).
87. Ton-That, D. and Flannery, M.R., Phys. Rev. A 15, 517 (1977).

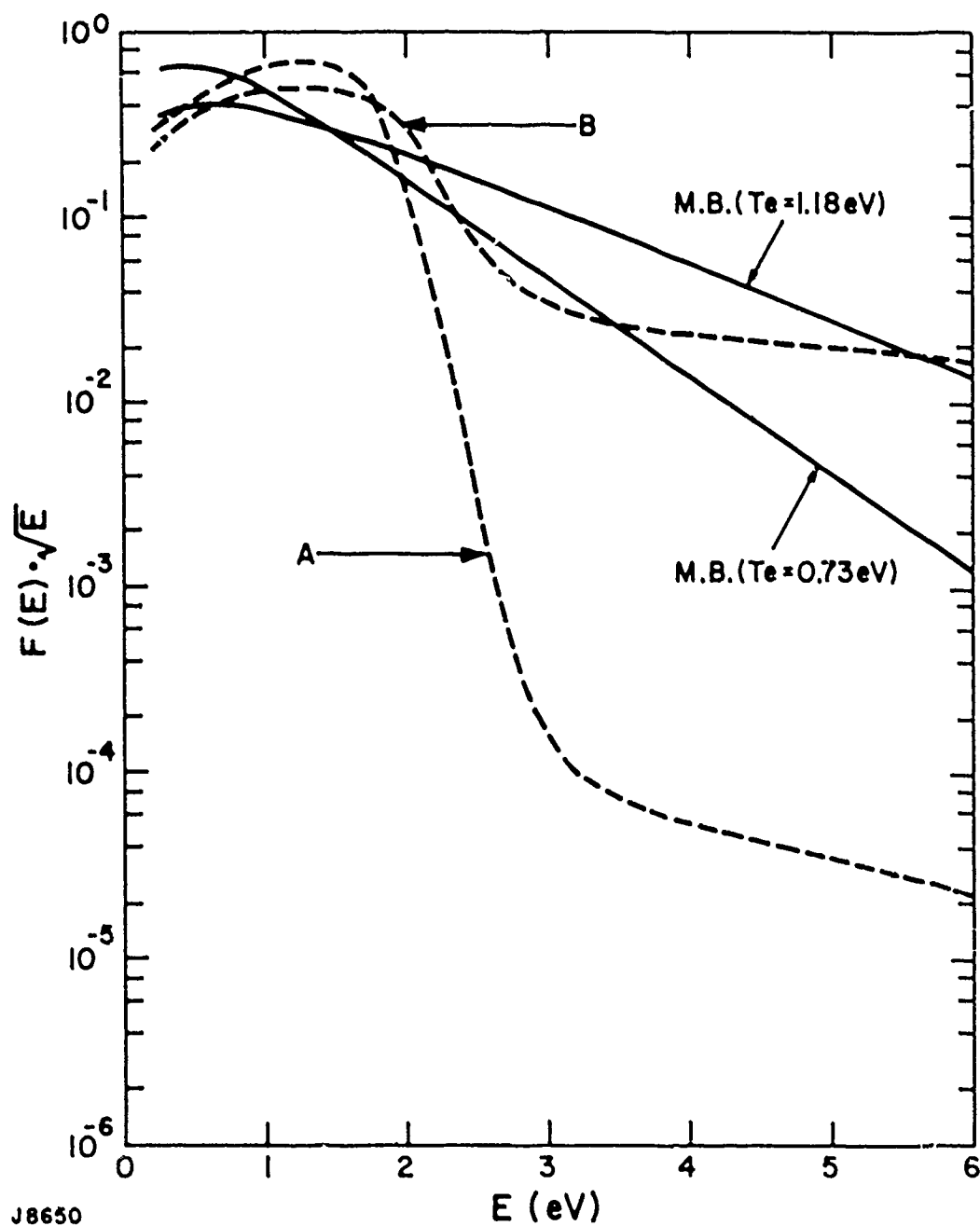


Figure 28 Dotted Curves are Electron Energy Distributions as Calculated by the Boltzmann Code: $E/N = 4.1 \times 10^{-16} \text{ v-cm}^2$ (curve A); $E/N = 1.02 \times 10^{-15} \text{ v-cm}^2$ (curve b). Solid lines are Maxwell Boltzmann Distributions for two average energies, $T_e = 1.09 \text{ eV}$ and $T_e = 1.77 \text{ eV}$

$$\langle U \rangle = \int_0^{\infty} dU f(U) U^{3/2} \quad (21)$$

For comparison, the Maxwell-Boltzmann (M-B) distributions which yield the same average energies are also displayed. It can be seen that the M-B distribution is a better approximation at the higher E/N value, but it always tends to overestimate the high energy tail and underestimate the low energy peak at both E/N values. These discrepancies should be kept in mind since, later, we will estimate rate constants for superelastic relaxation of the $N_2(A)$ and $N(^2P)$ states from the up-excitation rate constants using detailed balancing, a procedure that is only strictly correct for M-B distributions.

Fractional energy deposition ϕ_i into a particular inelastic channel is obtained by integrating Eq. (18) for each inelastic process and then evaluating the expression

$$\phi_i = \Delta U_i k_i / \sum_l \Delta U_l k_l$$

where l is an index running over all the inelastic processes. The results for total vibrational excitation, $\sum_{v=1}^8 \phi_v$; electronic excitation into A, B and C states $\sum_{E=1}^3 \phi_E$; dissociation and ground state ionization are displayed in Figure 29 as a function of E/N. It can be seen that vibrational excitation dominates for $E/N \leq 4 \times 10^{-16} \text{ V-cm}^2$ where the average electron energy is about 1 eV or less. This is the well-known region where the CO_2 laser operates. At higher E/N the vibrational contribution decreases and electronic excitation becomes important once the high energy tail of the electron energy distribution surpasses the first electronic threshold. This defines the lower limit of the E/N range that will lead to significant production of $N_2(A)$ states. However, there is also an upper limit to the useful E/N range due to the proportionately higher production rate of $N(^4S)$ atoms, produced through electron impact dissociation of N_2 . It will be shown below that $N(^4S)$ atoms are the dominant quenchers of $N_2(A)$. Therefore, it is important to produce as few $N(^4S)$ atoms as possible while still producing as many $N_2(A)$ states as possible. This effect can be seen more clearly in Figure 30 which displays the ratio, R, of the sum of the A, B and C electronic excitation rate constants k_{Ei} to the dissociation rate constant, k_D

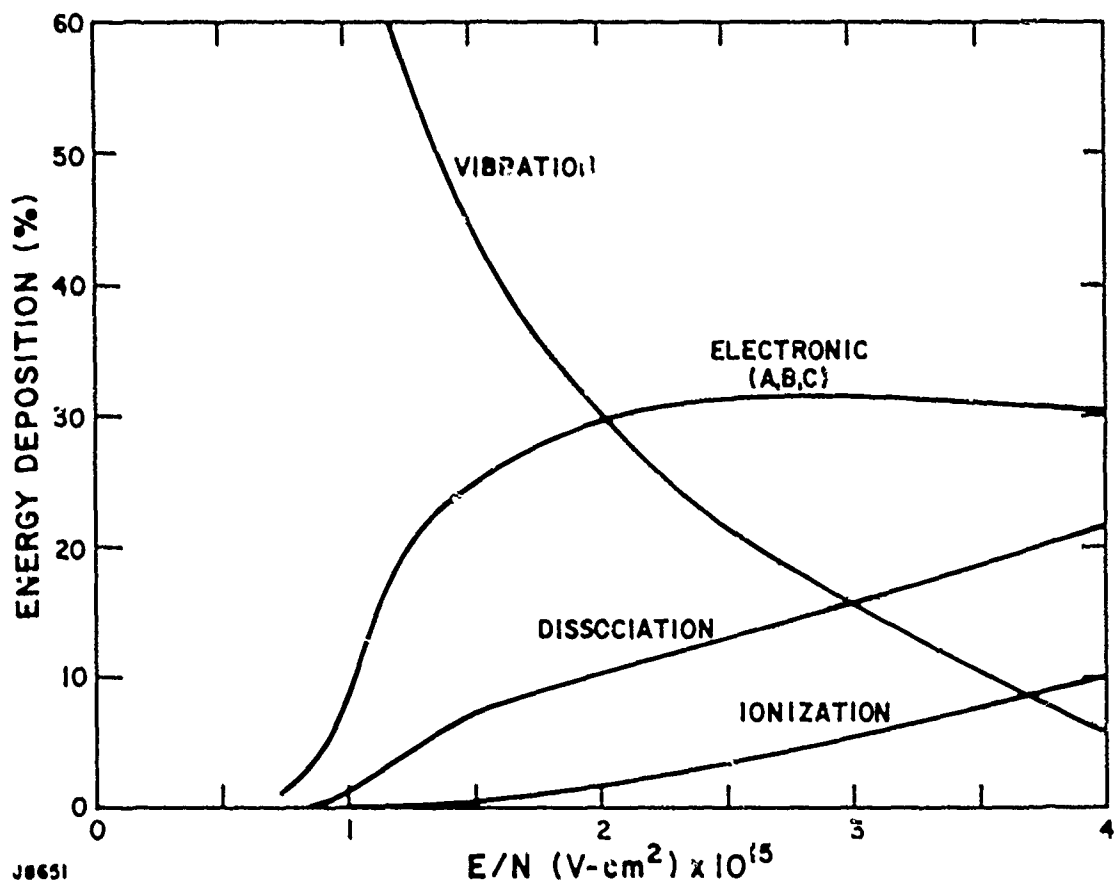


Figure 29 Fractional Energy Deposition in N_2 at 1 atm and 298°K vs E/N

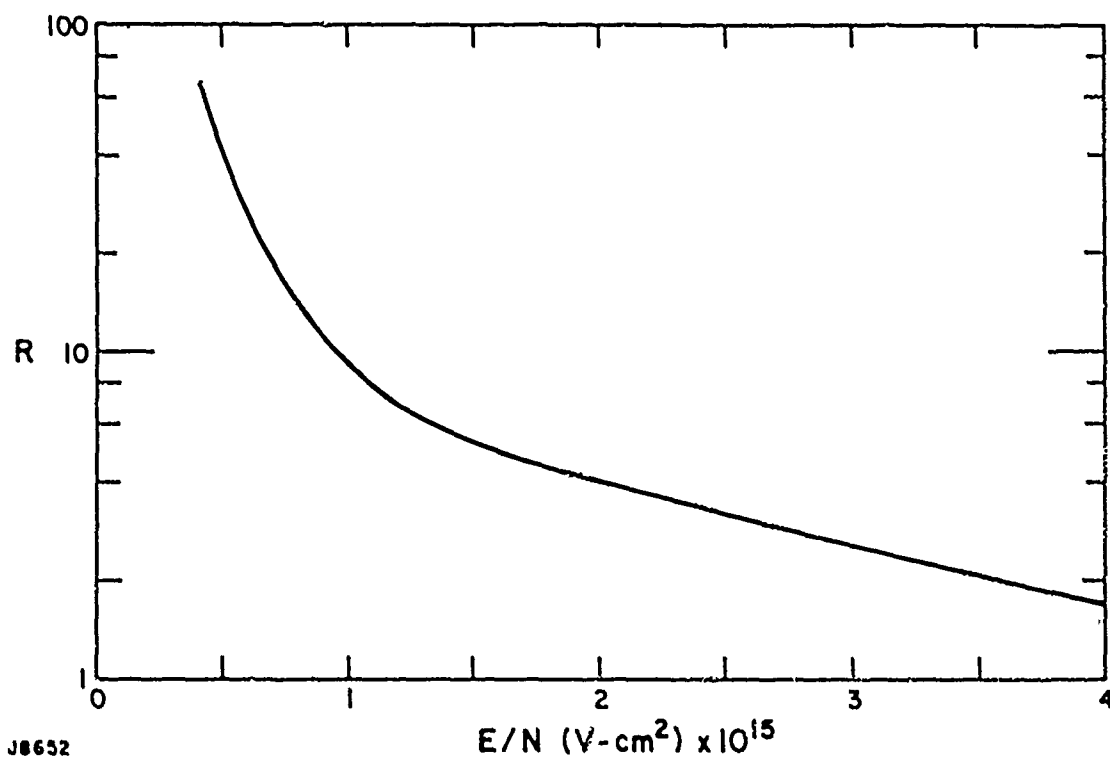


Figure 30 The Ratio, R , vs E/N for N_2 at 1 atm and 298°K

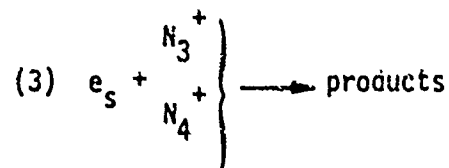
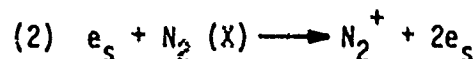
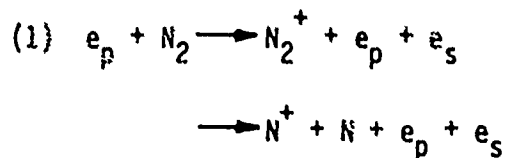
$$R = \sum_i k_{Ei} / k_D \quad i = A, B \text{ and } C \quad (22)$$

versus E/N . The ratio approaches one as E/N approaches $4 \times 10^{-15} \text{ V-cm}^2$ implying that at least one $N(^4S)$ atom is available to quench each $N_2(A)$. On the other hand, R -values in the range of 10-100 are available at somewhat lower E/N where significant $N_2(A)$ production may still be realized. As long as the $N_2(A)$ states can be extracted from the discharge before each $N(^4S)$ can be cycled through 10-100 quenching events, much of the initial $N_2(A)$ state population may still be extracted from the discharge as will be shown in the next section.

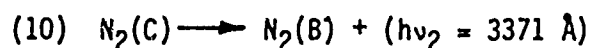
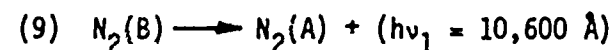
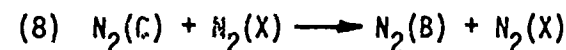
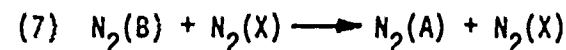
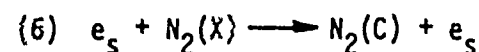
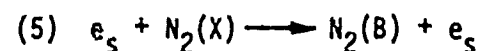
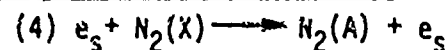
3. Kinetic Model

The following kinetic scheme was chosen to model the production.

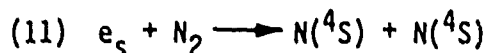
Ionization and Recombination Processes



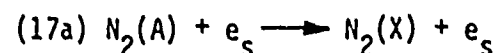
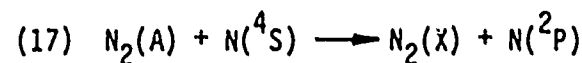
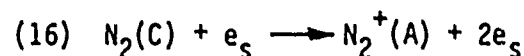
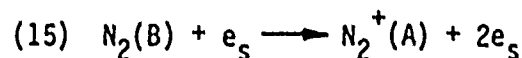
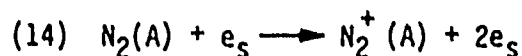
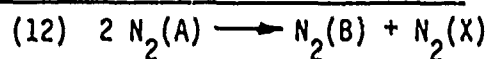
A- B- and C-State Excitation



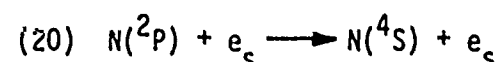
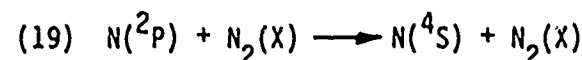
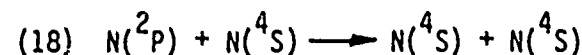
N₂ Dissociation



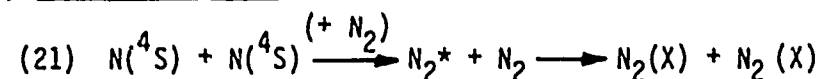
A- B- and C-State Loss Processes



N(^2P) Quenching



N(^4S) Recombination



where $N_2(X)$ is the N_2 ground electronic state.

The $N_2(A)$ states are produced via the direct secondary electron impact process (4) and through cascade from the higher lying $N_2(B)$ and $N_2(C)$ states, processes (7), (8), (9), and (10). The primary $N_2(A)$ loss process is due to the electronic-electronic energy transfer to $N(^4S)$ atoms to produce $N(^2P)$ states, process (17). The $N(^2P)$ states can then relax via processes (18), (19), and (20) allowing recycling of $N(^4S)$ population. $N(^4S)$ quenchers

are produced through both primary and secondary electron impact dissociation processes (1) and (11) and are permanently lost only through recombination (21). Other molecular N_2 triplet manifold loss processes are metastable ionization (14), (15), and (16) and superelastic loss (17a). We now describe how the values for the source functions and rate constants were chosen for each process.

The ionization rate by primary electrons was obtained from the energy deposition tables of Berger and Seltzer⁽⁹⁰⁾ and the energy partitioning results available from the radiation chemistry literature.⁽⁹¹⁾ The total e-beam deposition rate in N_2 is given by S ($W\ cm^{-3}$)

$$S = \left(\frac{1}{\rho} \frac{\partial E}{\partial X} \right)_{N_2} \rho_{N_2} J_{eb} \quad (23)$$

where J_{eb} is the primary e-beam current (in A/cm^2), ρ_{N_2} is the density of N_2 gas and $(1/\rho \partial E/\partial X)_{N_2}$ is the stopping power at a particular primary electron energy. For several hundred keV primary electrons, Ref. 90 gives $(1/\rho \partial E/\partial X)_{N_2} \approx 2\ MeV - cm^2/gr$ yielding a total energy deposition rate at 1 atm and 298°K

$$S = 2400 J_{eb} W/cm^3 \quad (23a)$$

The ionization rate, S_i ($cm^{-3}\ sec^{-1}$) is then given by:

$$S_i = (S/W_i) f_i \quad (24)$$

where W_i is the ion pair formation energy (eV per ion pair formed) for both N^+ and N_2^+ formation and f_i is the fraction of e-beam energy converted into ions. Reference 91 indicates $W_i = 34.5\ eV$ and $f_i \approx 0.5$ yielding $S_i = 2.28 \times 10^{20} J_{eb}$ ions/ cm^3 -sec. The secondary ionization rate constant, k_2 , is obtained from the Boltzmann code and is displayed in Table 3.

The dominant electron loss processes in pure N_2 are assumed to be volumetric electron ion recombination processes involving N_3^+ and N_4^+ clusters formed in the association reactions:

90. Berger, M.J. and Seltzer, S.M., Tables of Energy Losses and Ranges of Electrons and Positrons, NASA Special Publ. 3012, 1964.

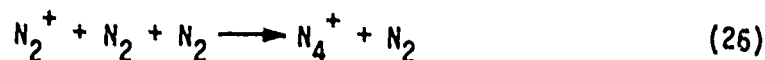
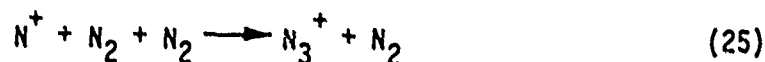
91. Willis, C. and Boyd, A.W., Int. J. Radiat. Phys. Chem. **8**, 71 (1976).

TABLE 3
EXCITATION RATE CONSTANTS VS E/N

RATE CONSTANT*	E/N ($\times 10^{15}$ V-cm ²)		
	<u>0.41</u>	<u>0.61</u>	<u>1.02</u>
k_2	1.24^{-20}	9.92^{-17}	1.47^{-13}
k_4	2.0^{-14}	1.61^{-12}	5.12^{-11}
k_5	1.68^{-14}	1.74^{-12}	6.66^{-11}
k_6	2.53^{-16}	1.04^{-13}	1.24^{-11}
k_{11}	5.66^{-16}	1.51^{-13}	1.36^{-11}
k_{14}	2.56^{-17}	2.15^{-14}	4.95^{-12}
k_{15}	1.97^{-15}	4.29^{-13}	3.22^{-11}
k_{16}	3.68^{-13}	2.85^{-11}	8.98^{-10}

$$a^{-N} = a \times 10^{-N} \text{ cm}^3/\text{sec}$$

*NOTE: k_i refers to rate constant for i th process in the kinetic model.



At these pressures the time scale for clustering is orders of magnitude faster than the expected recombination lifetime ($\leq 10^{-6}$ sec) justifying the assumption that N_3^+ and N_4^+ are the dominant positive ions in an e-beam sustained discharge. The global recombination rate constant in pure N_2 has been measured by D. Douglas-Hamilton⁽⁹²⁾ over the E/N range: $10^{-17} \leq E/N \leq 2.2 \times 10^{-16}$ V/cm². No attempt was made to deconvolute the separate recombination coefficients for N_3^+ and N_4^+ in these measurements. We fit these measurements to the following exponential functional forms:

for $1 \times 10^{-17} \leq E/N \leq 4 \times 10^{-17}$ V-cm²:

$$k_3(E/N) = \exp(-13.28 - (7.32 \times 10^{16} E/N))$$

for $4 \times 10^{-17} \leq E/N \leq 2.2 \times 10^{-16}$ V-cm²:

$$k_3(E/N) = \exp(-16.15 - (1.32 \times 10^{15} E/N))$$

and the latter expression was then linearly extrapolated (on semilog paper) to the E/N range of interest here: $0.4 - 1 \times 10^{-15}$ V-cm².

The electron pumping rate constants into the A, B and C states (k_4 , k_5 , k_6) are listed in Table 3 at three E/N values. The dominance of A and B state excitation is in accord with other Boltzmann code results in pure N_2 .⁽⁹³⁾ The quenching of $N_2(C)$ states by N_2 dominate the cascade from C to B ($k_8 = 1.5 \times 10^{-11}$ cm³/sec and $k_{10} = 2.2 \times 10^7$ sec⁻¹).⁽⁹⁴⁾ Similarly, cascade from B to A is also dominated by collisional quenching ($k_7 = 2.0 \times 10^{-12}$ cm³/sec and $k_9 = 1.1 \times 10^5$ sec⁻¹).⁽⁹⁴⁾

92. Douglas-Hamilton, D.H., J. Chem. Phys. 58, 4820 (1973).

93. Judd, O., IEEE Journal of Quantum Electronics QE-12 78, 1976.

94. Hill, R.M., Gutcheck, R.A., Huestis, D.L., Mukherjee, D. and Lorents, D.C., "Studies of E-Beam Pumped Molecular Lasers," SRI Tech. Rept. MP-74-39, Tech Rept. No. 3 Contract No. N00014-72-C-0478, Stanford Research Institute, Menlo Park, California 94025.

There are two contributions to the dissociation yield of $N(^4S)$: secondary and primary electron impact. There are two measurements of the secondary electron impact dissociation yield of N_2 . Winters⁽⁸⁴⁾ has inferred the total cross section for process (11), the dissociative excitation process (27a), and dissociative ionization process (27b)



(where N^* is an excited nitrogen atom) using a complex surface absorption experiment that required making pumping speed measurements and assuming values for the probability that N , N^+ and N^* would stick to a collection surface. These results are in surprisingly good agreement with the (more straightforward) molecular beam measurements of Niehaus.⁽⁸⁵⁾ These latter measurements detect all N atoms but suppress all N^+ ions. Zipf⁽⁹⁵⁾ has compared the data of both of these studies and his results suggest that (11) and (27a) dominate (27b). The rate constants derived from these cross-section data are displayed in Table 3. The source function for primary electron impact dissociation was obtained from the Berger and Seltzer tables⁽⁹⁰⁾ and the N_2 radiation chemistry literature⁽⁹¹⁾ in a manner analogous to ionization source function described above. The energy required to form a $N(^4S)$ atom, W_a , is 32.9 eV and $f_a \approx 0.5$ yielding an atom source function rate, S_a , equal to $2.28 \times 10^{20} J_{eb} \text{ atoms cm}^{-3} \text{ sec}^{-1}$.

There is still much disagreement as to the rate constant for the pooling reactions (12) and (13). Hays and Oskam⁽⁹⁶⁾ have measured a rate constant for total loss out of the A state, $1.4 \times 10^{-9} \text{ cm}^3/\text{sec}$, and a specific C state formation rate constant $= 2.6 \times 10^{-10} \text{ cm}^3/\text{sec}$. Stedman and Setser⁽⁹⁷⁾ and Zipf⁽⁹⁸⁾ have measured $2 \times 10^{-11} \text{ cm}^3/\text{sec}$ for a C state production rate constant and Zipf⁽⁹⁸⁾ has obtained a total loss rate constant $= 3 \times 10^{-10} \text{ cm}^3/\text{sec}$. The Stanford Research Institute kinetics

95. Zipf, E.C. and McLaughlin, R.W., Planet. Space Sci. 26, 449 (1978).
96. Hays, G.N. and Oskam, H.J., J. Chem. Phys. 59, 6088 (1973).
97. Stedman, D.H. and Setser, D.W., J. Chem. Phys. 50, 2256 (1969).
98. Zipf, E.C., Bull. Am. Phys. Soc. 10, 179 (1965).

group has discussed these various measurements and have suggested that incomplete vibrational relaxation due to low operating pressures (a few torr) may explain the variety of results.⁽⁹⁴⁾ In turn, they have derived their own set of pooling rate constants obtained in high-pressure studies of e-beam excited Ar/N₂/NO mixes (several thousand torr). We have chosen to use their values ($k_{12} = 8 \times 10^{-11}$ cm³/sec and $k_{13} \approx 2 \times 10^{-11}$ cm³/sec)⁽⁹⁴⁾ as being best representative of the conditions of interest in this study.

The quenching rate of N₂(A) by N-atoms is one of the important N₂(A) loss processes in N₂ discharges. The values of the rate constant for this process fall into two groupings: Young,⁽⁹⁹⁾ Wray,⁽¹⁰⁰⁾ and Setser⁽¹⁰¹⁾ have all obtained $k_{17} = 5 \times 10^{-11}$ cm³/sec while Thrush,⁽¹⁰²⁾ et al., and Weinreb,⁽¹⁰³⁾ et al. have obtained rate constants a factor of 10 and 100 times lower, respectively. The most definitive experiment appears to be that of Setser, who directly monitored the time dependence of both the N₂(A) state loss and N(²P) formation. These results not only confirm the Young⁽⁹⁹⁾ and Wray⁽¹⁰⁰⁾ work but also indicate that A state quenching to form the N(²P) state is the dominant loss channel. Therefore, we have chosen to use the 5×10^{-11} cm³/sec for k_{17} in these studies.

The N(²P) states are quenched by N(⁴S), electrons and N₂(X) species. The final products of the quenching processes have not been definitively identified although they must surely involve the lower N(²D) and N(⁴S) states. We assume that the ground state N(⁴S) atoms is formed based upon other N(²D) quenching evidence which indicates that the D-state quenching rate (D→S) by N₂(X) is two orders of magnitude faster than the P-state quenching rate. If P-state quenching proceeds via the D-state intermediate, then the overall rate, P→S, will be limited by the P→D rate.

99. Young, R.A. and St. John, G., J. Chem. Phys. 48, 895 (1968).

100. Wray, K.L., J. Chem. Phys. 44, 623 (1966).

101. Meyer, J.A., Setser, D.W. and Stedman, D.H., J. Phys. Chem. 74, 2238 (1970).

102. Thrush, B.A., J. Chem. Phys. 47, 3691 (1967).

103. Weinreb, M. and Mannella, G.G., J. Chem. Phys. 50, 3129 (1969).

There are four measurements of P-state quenching by $N_2(X)$: $k_{19} \leq 1 \times 10^{-16}$ cm³/sec, ⁽¹⁰⁴⁾ $k_{19} \leq 3 \times 10^{-16}$ cm³/sec, ⁽¹⁰⁵⁾ $\approx 6 \times 10^{-14}$ cm³/sec, ⁽¹⁰⁶⁾ 3×10^{-19} cm³/sec. ⁽¹⁰⁷⁾ Again, it is difficult to choose among these values. Husain et al. ⁽¹⁰⁵⁾ argue that Kaufman's result ⁽¹⁰⁶⁾ is too fast and may reflect quenching by other transient species that appear in their higher power discharge. In addition, Husain's result is a direct time resolved quenching measurement and should be reliable. We have (somewhat arbitrarily) chosen $k_{19} = 2 \times 10^{-16}$ cm³/sec based upon the average of the two values which are in close agreement.

P state quenching by $N(^4S)$ is important at high energy loadings where significant $N(^4S)$ are produced. Wayne, et al. reported a preliminary measurement $k_{18} = 1 \times 10^{-11}$ cm³/sec accurate to within a factor of two. ⁽¹⁰⁸⁾ This value was used in the present study.

An estimate of superelastic quenching of $N(^2P)$ by electrons was obtained by using the up excitation rate constant for (28)



and the detailed balance expression:

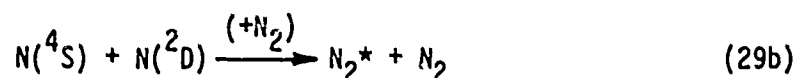
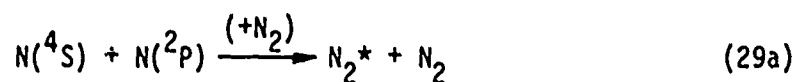
$$\frac{k_{28}}{k_{20}} = \frac{g(^2P)}{g(^4S)} e^{-\Delta E/kT_e}$$

where $\Delta E = 3.58$ eV. The rate constant k_{28} has been calculated by Ali ⁽¹⁰⁹⁾ who integrated the cross sections of Henry, et al. ⁽¹¹⁰⁾ for process (28)

104. Donovan, R.J. and Gillespie, H.M., Specialist Periodical Reports, Reaction Kinetics - Vol I, P.G. Ashmore Ed. (The Chemical Society Burlington House, London, 1975) Chapt. 2.
105. Husain, D., Kirsh, L.J. and Wiesenfeld, J.R., Faraday Discuss. Chem. Soc. No. 53, 201 (1972).
106. Lin, C.-L and Kaufman, F., J. Chem. Phys. 55, 3760 (1971).
107. Noxon, J.F., J. Chem. Phys. 36, 926 (1962).
108. Golde, M.F. and Thrush, B.A., Faraday Discuss. Chem. Soc. No. 53, 233 (1972).
109. Ali, A.W., U.S. Naval Res. Lab Plasma Dynamics Tech. Note 24 (1970); see also DNA Handbook, 2nd Ed. DNA 1948 H, p. 20-46.
110. Henry, R.J.W., Burke, P.G. and Sinfailam, A.-L., Phys. Rev. 178, 218 (1969).

over a Maxwell Boltzmann electron energy distribution. Using the detailed balance expression, we obtain $k_{20} \approx 1 - 3 \times 10^{-9} \text{ cm}^3/\text{sec}$ for the electron temperature range ($T_e \approx 1-2 \text{ eV}$) of interest here. It should be remembered that we showed in Section IV-C-2 that the Maxwell-Boltzmann electron energy distribution is only a crude approximation to the true energy distribution. Therefore, we expect all of our superelastic quenching rate constants to be somewhat in error, probably on the low side. However, the effect of the error on the kinetics is small because process (20) is not the dominant $N(^2P)$ quenching process due to the low electron density in the afterglow. We also note that the superelastic quenching of $N_2(A)$ by electrons was evaluated in a manner similar to that for k_{20} . In this case, the up-excitation rate, k_4 , was directly obtained from our Boltzmann code results. However, the use of detailed balancing still requires the assumption of a Boltzmann energy distribution. Therefore, the caveat regarding the error in k_{20} is also applicable to our value of $k_{17a} \approx 10^{-9} \text{ cm}^3/\text{sec}$.

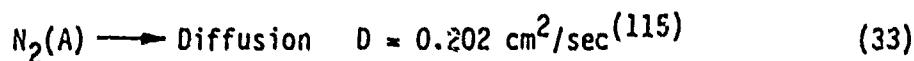
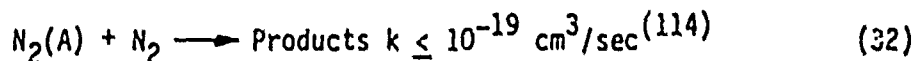
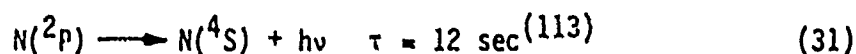
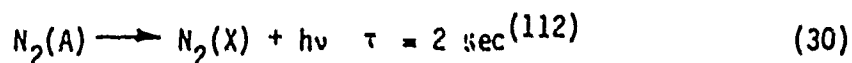
We assume that only $N(^4S)$ atoms can recombine to form N_2 via the three-body process (21), the only net $N(^4S)$ loss process in our model. We use the Leeds' group recommended value $k_{21} = 8.3 \times 10^{-34} \exp(500/T) \text{ cm}^6/\text{sec}$.⁽¹¹¹⁾ Other recombination processes such as:



are probably dominated by quenching processes, (e.g., process (18)) especially considering that (29a) and (29b) must remove even more energy than (21). This suggests the k_{29a} and k_{29b} will be even slower than k_{21} and both processes can be neglected.

Finally, we note that the following other processes can also be neglected because they are much too slow to affect significantly any of the kinetics:

111. Baulch, D L., Drysdale, D.D. and Horne, D.G., Evaluated Kinetic Data for High Temperature Reactions - Vol II, (Buttersworth and Co., London, 1973) p. 25.



at 1 atm, 300°K

4. Results

The set of coupled rate equations that describe the 21 processes in our model were numerically integrated on an IBM computer using the Gear algorithm^(116,117) a sixth order predictor-corrector method that also allows for variable integration order and variable step size. This method is usually applied to stiff sets of differential equations in which the characteristic time constants (eigenvalues) have widely differing values as is the case in the $N_2(A)$ kinetics code. For example, $N_2(A)$ state loss is controlled by $N(^4S)$ quenching which has a typical characteristic time of 2 μsec (at $J_{\text{eb}} = 10 \text{ A/cm}^2$ and $E/N = 1 \times 10^{-15} \text{ V-cm}^2$) while the characteristic time for $N(^4S)$ three-body recombination is about 460 μsec under the same conditions.

The computer program was designed to optimize the $N_2(A)$ state production relative to atom production during the e-beam pulse. This was accomplished by leaving the e-beam and discharge field on as long as the ratio, $N_2(A)/(N(^4S) + N(^2P))$, continued to increase. Once the maximum in the ratio was reached the e-beam and discharge field were shut off. Typical pumping times were of the order of 1 μsec or less for $J_{\text{eb}} = 10 \text{ A/cm}^2$ to as much as several hundred microseconds for $J_{\text{eb}} = 10 \text{ }\mu\text{A/cm}^2$.

112. Shemansky, D.E., J. Chem. Phys. 51, 689 (1969).

113. Garstang, R.H., in Aurora and Airglow, (Pergamon Press, New York, N.Y. 1956) p. 324.

114. DNA Reaction Rate Handbook, Second Edition, DNA 1948H, March 1972, Chapt. 20.

115. Zipf, E.C., J. Chem. Phys. 38, 2034 (1963).

116. Gear, C.W., Comm. ACM 14, 176 (1971).

117. Gear, C.W., Comm. ACM 14, 185 (1971).

In order to check that instabilities in the calculation were not being generated by the abrupt e-beam turnoff, several comparisons were made between a continuous integration scheme (from 10^{-17} sec to 10^{-2} sec) and a two-step integration scheme that first integrates up to the e-beam shutoff point and then uses the concentrations at the point as initial conditions for a second integration from e-beam shutoff to 10^{-2} sec. In all cases it was shown that either method gave the same results within the error limit of the code. This relative error was typically set at 10^{-6} of the maximum value of any species concentration.

Figures 31 through 36 display the computer output in graphical form for different values of J_{eb} and E/N . Of the seven species represented by the model, four were chosen to be displayed: $N_2(A)$ (closed circles), secondary electrons (open squares), $N(^4S)$ (open circles) and $N(^2P)$ (closed squares).

In general, it is seen that the temporal behavior of a given species is approximately the same irrespective of the value J_{eb} or E/N . Electron densities rise at a linear rate proportional to the source function except at high E/N and low J_{eb} where secondary ionization is important. In this case, exponential growth is observed. Steady-state electron densities, n_e , are reached if the e-beam is left on for a time long compared with the recombination time. Under no conditions did we ever observe a catastrophic growth of electron density as a result of a volumetric instability. While the electron density grows linearly in time, both $N(^4S)$ and $N_2(A)$ grow quadratically as both are produced by secondary electron impact on ground state N_2 , i.e., $dN_2(A) \propto dN(^4S) \propto n_e dt$. Likewise, $N(^2P)$ grows as t^5 since it is produced by $N(^4S)$ quenching $N_2(A)$, i.e., $dN(^2P) \propto [N_2(A)][N(^4S)] dt \propto t^2 t^2 dt$.

Once the e-beam and discharge field are shut off the electron density decays at the rate characteristic of electron ion recombination. This rate constant was taken to be the room temperature value, k_3 ($T_e = T_g = 300^\circ K$) for all the conditions studied here. In effect, we are assuming instantaneous electron cooling down to ambient temperature and negligible thermal heating. The time dependence of the recombination process is given by

$$n_e(t) = n_{e0} / (1 + k_3 n_{e0} t)$$

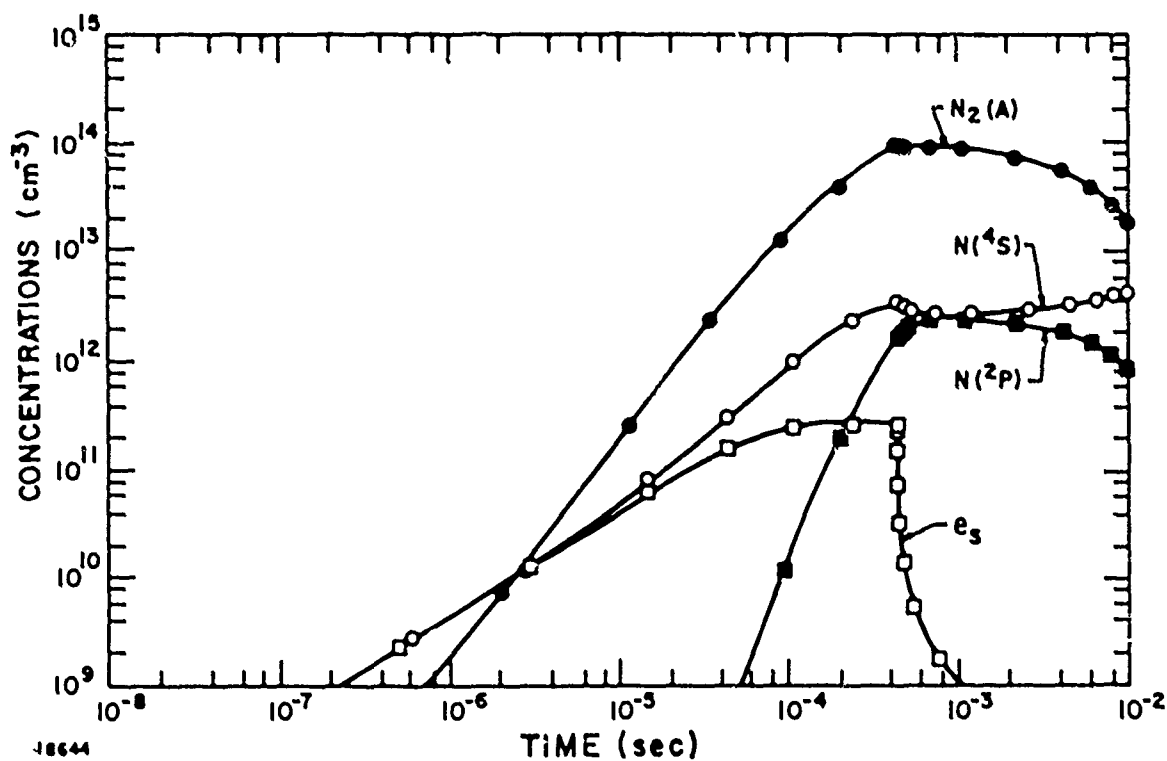


Figure 31 The Results of the $N_2(A)$ Kinetics Code at $J_{eb} = 10^{-5}$ amps/cm², $E/N = 4.1 \times 10^{-16}$ v-cm², $T = 298^\circ K$ and 1 atm N_2

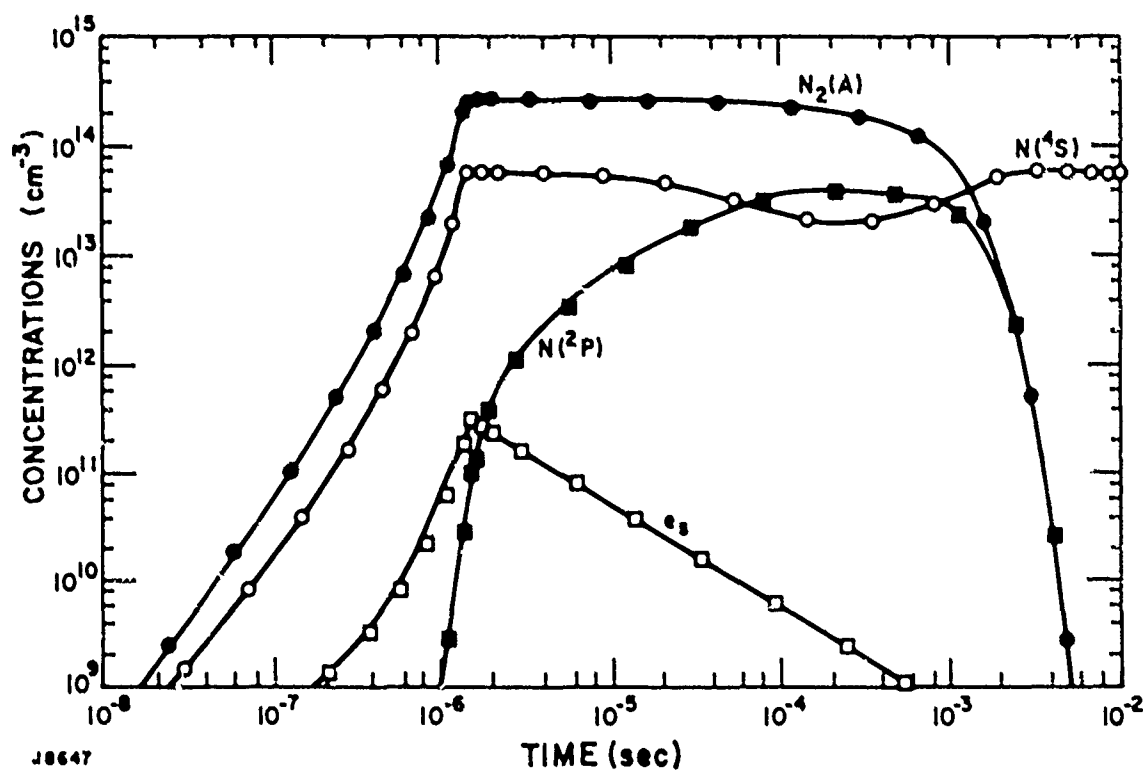


Figure 32 The Results of the N₂ (A) Kinetics Code at $J_{eb} = 10^{-5}$ amps/cm², $E/N = 1.02 \times 10^{-15}$ v-cm², $T = 298$ K and 1 atm N₂

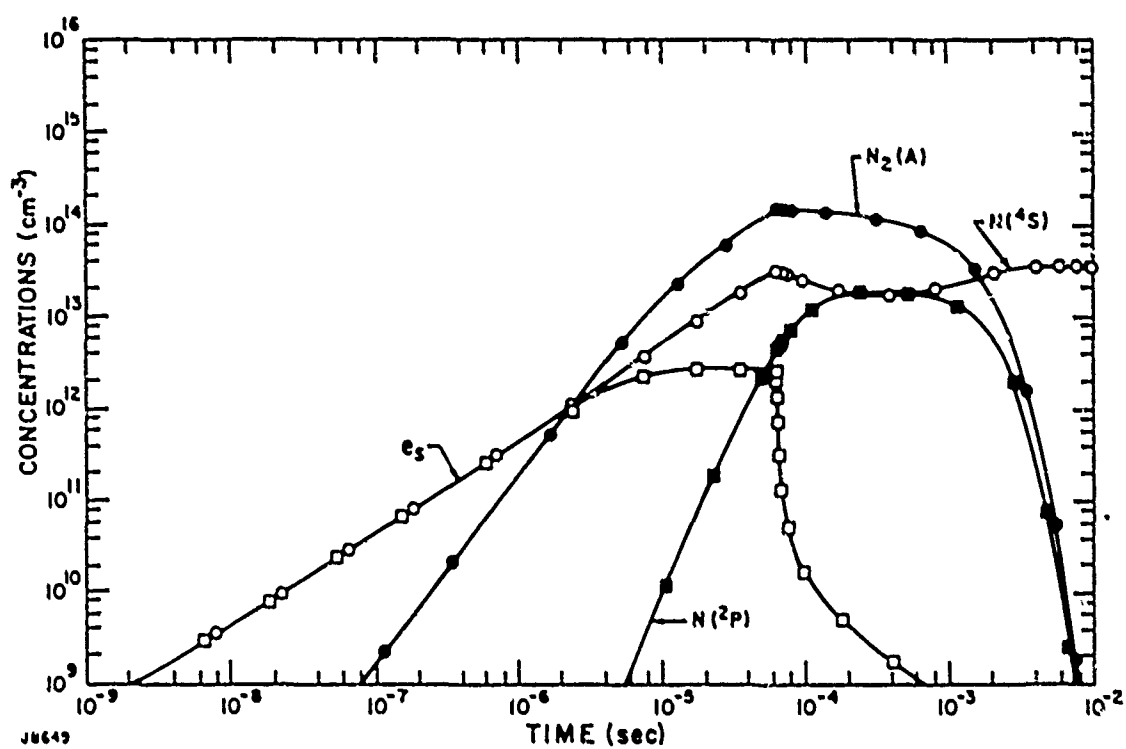


Figure 33 The Results of the N₂ (A) Kinetics Code at $J_{eb} = 10^{-3}$ amps/cm², $E/N = 4.1 \times 10^{-16}$ v-cm², $T = 298^\circ\text{K}$ and 1 atm N₂

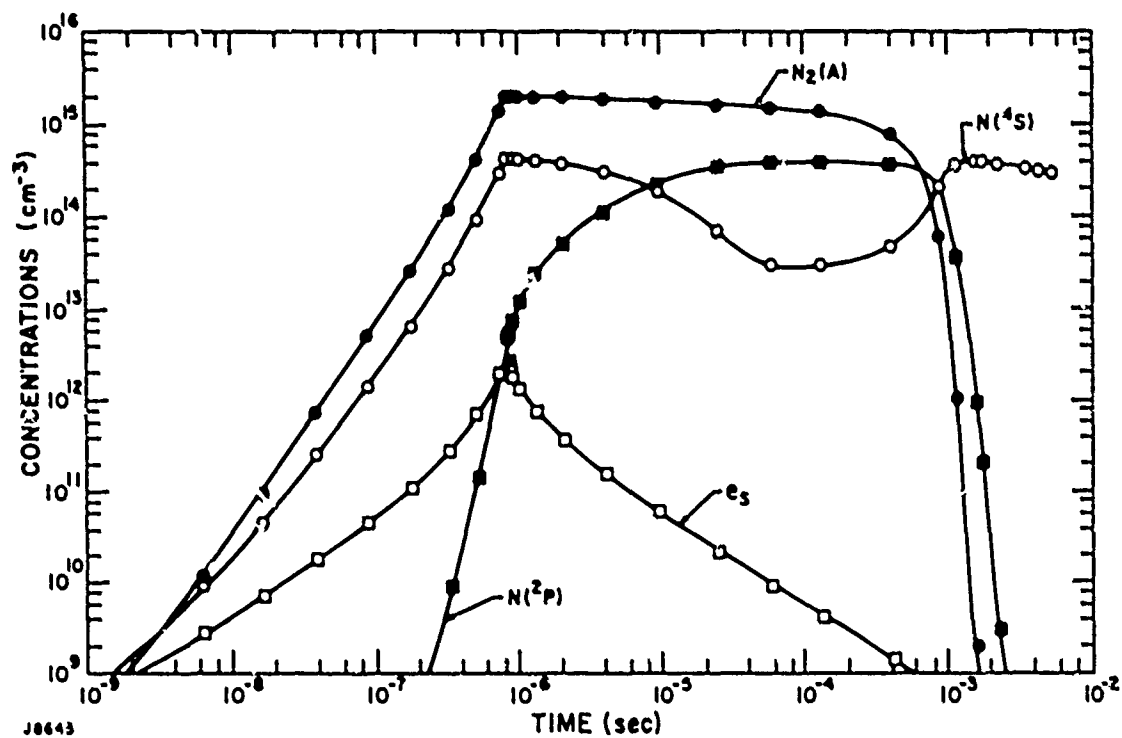


Figure 34 The Results of the N₂ (A) Kinetics Code at $J_{eb} = 10^{-3}$ amps/cm², $E/N = 1.02 \times 10^{-15}$ v-cm², $T = 298^\circ\text{K}$ and 1 atm N₂

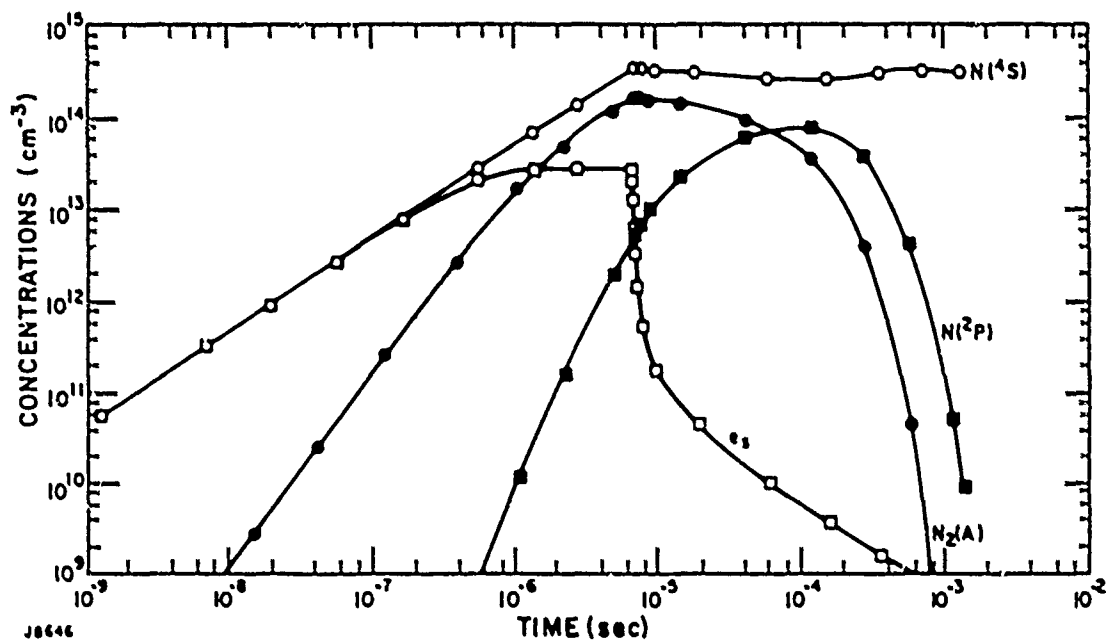


Figure 35 The Results of the N₂ (A) Kinetics Code at $J_{eb} = 10^{-1}$ amps/cm², $E/N = 4.1 \times 10^{-16}$ v-cm², $T = 298^\circ\text{K}$ and 1 atm N₂

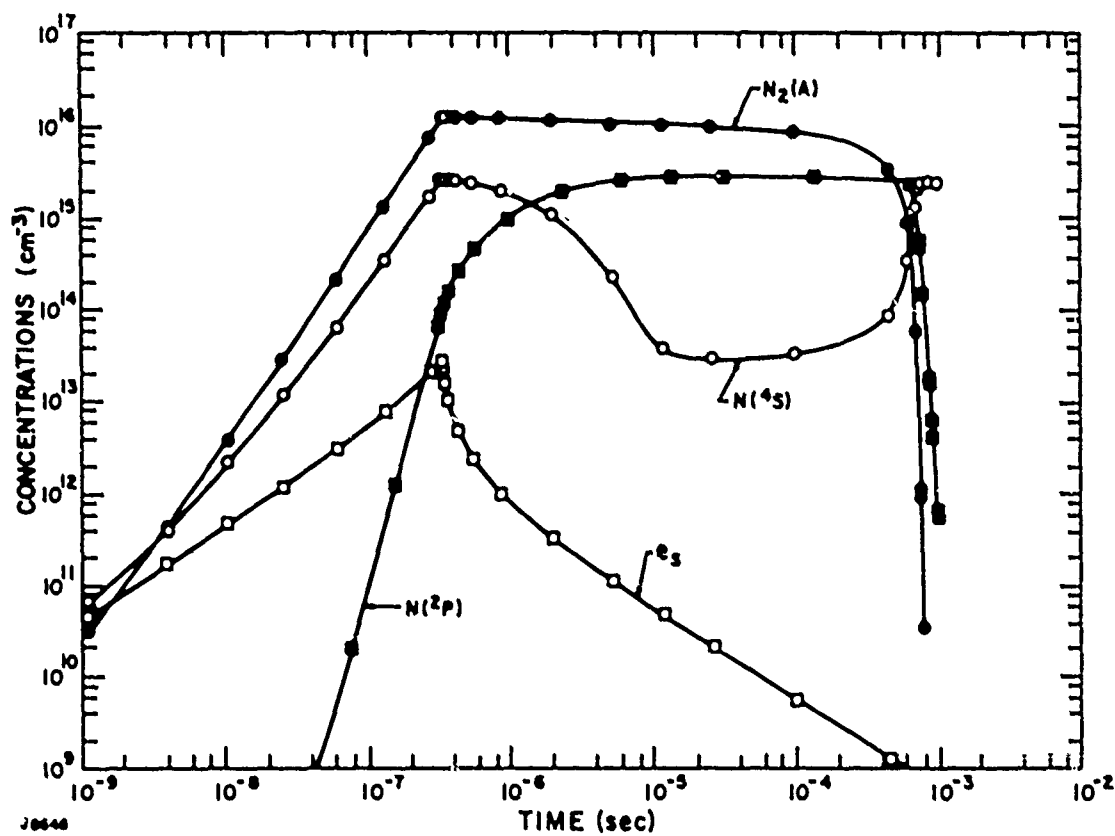


Figure 36 The Results of the N₂ (A) Kinetics Code at $J_{eb} = 10^{-1}$ amps/cm², $E/N = 1.02 \times 10^{-15}$ v-cm², $T = 298$ K and 1 atm N₂

where n_{eo} is the electron density when the e-beam is shut off. This leads to an approximate t^{-1} time dependence for $t \gg (k_3 n_{eo})^{-1}$ as can be seen in Figures 31 through 36.

A key feature of the graphical output is the rapid rate of loss of $N_2(A)$ states that typically occurs on the one-half to several millisecond time scale. It is apparent that appreciable $N_2(A)$ state density can only be obtained if A states are rapidly extracted from the discharge region on this time scale or faster. Otherwise, quenching will reduce A state population to a negligible value. In Section IV-C-6 we describe one method for extracting the A states.

The rate of loss of $N_2(A)$ states is controlled primarily by the $N(^4S)$ quenching process (17) whereas metastable ionization loss processes (14), (15) and (16) and the superelastic relaxation process (17a) play only negligible roles in the afterglow. The A state loss rate depends upon three quantities: (1) the absolute atom density at the time of e-beam shutoff, (2) the residence time, t_r , in the discharge zone and (3) the rate at which $N(^2P)$ is quenched to $N(^4S)$. Assuming for the moment one hypothetical limiting case where the $N(^2P)$ to $N(^4S)$ quenching rate is infinitely fast leads to an approximate expression for the time dependence of $N_2(A)$ in the afterglow:

$$N_2^M(t) = N_2^M(A) e^{-kNt_r}$$

where $N_2(A)$ is the A-state number density at shutoff; $k = k_{17}$; and N is the sum of $N(^4S)$ pulse $N(^2P)$ at shutoff. This expression describes a situation in which the ground state atom density can be recycled (and is effectively constant). The 2P atoms, formed in the A state quenching process, are being instantly converted back to 4S atoms which, in turn, produce more P states through A state quenching. On the other hand, if we assume a negligible $N(^2P)$ to $N(^4S)$ quenching rate, then the $N(^4S)$ population can be rapidly used up and recycling of ground-state atoms becomes impossible. In this case, $[N_2^M(A) - N(^4S)]$ net A states will be left at $t \rightarrow \infty$ if $N_2(A) \geq N(^4S)$. If $N(^4S) \geq N_2(A)$, then all A states will be lost.

In reality, the $N(^2P)$ to $N(^4S)$ quenching rate is sufficiently rapid that significant recycling of ground-state atoms occurs. Two processes dominate the 2P quenching: relaxation by $N(^4S)$, process (18), and relaxation

by molecular N_2 , process (19). Of these two, process (19) dominates except when the $N(^4S)$ density reaches $\sim 5 \times 10^{14} \text{ cm}^{-3}$. This occurs for the cases where $J_{eb} \geq 10^{-1} \text{ A/cm}^2$. Since the $^2P \rightarrow ^4S$ rate is at least 5000 sec^{-1} ($\approx 200 \text{ } \mu\text{sec}$), each 4S state can be recycled at least five times assuming a 1 msec residence time.

As a result of these considerations Table 4 presents the maximum number of A states, $N_2(A)$, produced in the discharge and its lifetime at a variety of J_{eb} and E/N values at 298°K and 1 amagat N_2 . We have also tabulated the discharge energy deposited in the gas, E_D , and the fraction, f_M , of discharge energy converted to metastable A state excitation. The former quantity is given by the expression:

$$E_D = e(E/N)N \int_0^{\infty} i dt \approx e(E/N) N V_d n_e^M \tau_{eb} / 2$$

where N is the N_2 density at one amagat, V_d is the electron drift velocity calculated from the Boltzmann code, n_e^M is the maximum secondary electron density at e-beam shutoff, τ_{eb} is the pulse time of the e-beam and discharge field, and the factor of two accounts for the assumed triangular time dependence of the discharge current, i . The quantity, f_M , is given by:

$$f_M = (N_2^M(A) \Delta E / E_D) \times 100$$

where $\Delta E = 9.87 \times 10^{-19} \text{ J}$. The e-beam energy deposited in the gas is negligible compared to the discharge energy and is neglected in calculating f_M .

The graphical output data and Table 4 indicate that the lifetimes are longer at low E/N and low J_{eb} because the absolute $N(^4S)$ density is lower for these conditions. On the other hand, it is seen that the largest values of $N_2^M(A)$ are obtained at high E/N and J_{eb} . Therefore, some trade-offs will be required to obtain optimal A state density and flux. It should be noted that these lifetimes were obtained from the first e-fold times for A state loss. For the cases where $N(^4S)$ is growing rapidly over this time scale, A state decay is not described by a single characteristic time. Instead, the temporal behavior indicated in Figures 31 through 36 should be used.

One of the key unknowns in the A state kinetics calculations is the effects of gas heating (both vibrational and translational). The kinetics

TABLE 4

KINETICS CODE RESULTS

$j_{\text{eb}}(\text{A/cm}^2)$	$E/N(\text{V-cm}^2)$	$N_2(\text{A})^{\text{MAX}}(\text{cm}^{-3})$	$\tau_{\text{H}_2}(\text{A})(\text{sec})$	$E_D(\frac{\text{J}}{\text{A}\cdot\text{cm}})$	$f_M(\%)$
10^{-5}	4.1^{-16}	8^{13}	7×10^{-3}	521	0.015
10^{-5}	6.1^{-16}	1.25^{14}	3.8×10^{-3}	29.2	0.41
10^{-5}	1.02^{-15}	3.0^{14}	9.0×10^{-4}	11	2.7
10^{-3}	4.1^{-16}	1.6^{14}	1.0×10^{-3}	780	0.02
10^{-3}	6.1^{-16}	1.0^{15}	1.4×10^{-3}	651	0.15
10^{-3}	1.02^{-15}	2^{15}	5.0×10^{-4}	49	4
10^{-1}	4.1^{-16}	1.7^{14}	1.0×10^{-4}	818	0.021
10^{-1}	6.1^{-16}	4^{15}	1.5×10^{-3}	972	0.4
10^{-1}	1.02^{-15}	1.2^{16}	3.9×10^{-4}	215	5.6
10	4.1^{-16}	1.8^{14}	65×10^{-6}	923	0.019
10	1.02^{-15}	6^{16}	4.5×10^{-4}	1090	5

$$a^N \equiv a \times 10^N$$

code described above assumes that the gas is always at 298°K and ignores any excited vibrational state effects on the rate constants. In addition, the code does not keep track of the gas temperature rise nor are temperature dependent rate constants included. These effects may be important for many of the cases shown in Table 4 where the energy deposition, E_D , will lead to as much as a 500-1000°K temperature rise. The specific heat of N_2 is about 1 J/l-atm-°K. The uncertainty arises because neither the rate of heating (at the E/N values used here) nor the temperature dependences of the important quenching processes are known. It is reasonable to expect that the heating pulse evolves on a time scale comparable to the time scale for A state extraction (~ msec). However, until more information becomes available, this uncertainty will remain.

Finally, we comment on the apparent population inversion of $N(^2P)$ with respect to $N(^4S)$ that occurs on the post e-beam time scale (see Figures 31 through 36). This effect is seen to occur whenever the e-beam production of $N_2(A)$ exceeds that of $N(^4S)$. The inversion is created because the loss of $N(^4S)$ via $N_2(A)$ quenching is faster than $N(^2P)$ quenching. The possibility of a storage laser at 3467 Å should be considered.

5. Effects on N_2 Gas Density, Initial Gas Temperature and Added Species

We discuss briefly possible modifications in the above model that could improve A state production by reducing the rate at which A states are quenched by ground state N atoms.

A substantial reduction in the initial N_2 gas density below one amagat would help by slowing down the rate of $N(^2P) \rightarrow N(^4S)$ relaxation. This would effectively lower the number of times that a $N(^4S)$ atom quencher could be recycled given a fixed residence time in the discharge zone. The limit on N_2 density reduction would occur when $N(^2P)$ relaxation becomes dominated by N atom quenching ($N(^4S) \geq 5 \times 10^{14} \text{ cm}^{-3}$). One deleterious effect of lowering the N_2 density would be the reduced rate of $N(^4S)$ three-body recombination. However, this would be negligible at low J_{eb} values where N atom loss through recombination is very slow anyway.

A substantial reduction in the initial N_2 gas temperature would accelerate the rate of N atom loss via the three-body recombination process (21). The best value for the temperature dependence of the $N(^4S)$ recombination rate constant is given by the Leeds value⁽¹¹¹⁾

$$k_{21}(T) = 8.3 \times 10^{-34} \exp(500/T) \text{ cm}^6/\text{sec}$$

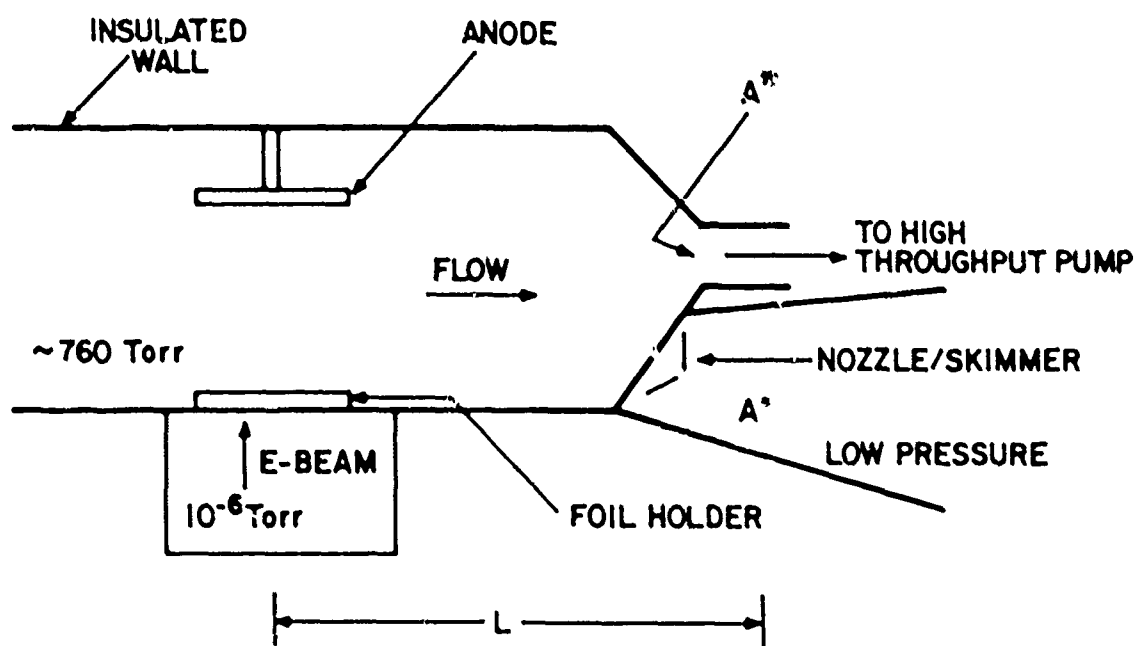
for $100^\circ\text{K} \leq T \leq 500^\circ\text{K}$ and $M = \text{N}_2$. This implies that a thirty-fold faster recombination time might be realized by dropping the ambient gas temperature from 300°K to 100°K . Unfortunately, this reduction would have the greatest impact for the high energy loading cases where the temperature rise from the discharge heating processes might wipe out any beneficial effects that accrue from the initial gas cooling.

Ideally, it would be advantageous to add small concentrations of another species which would chemically remove the N atoms. This species would have to have two properties: (1) it must react rapidly with $\text{N}(^4\text{S})$ and/or $\text{N}(^2\text{P})$, and (2) both the reactant species and any products of the reaction must be inefficient A state quenchers. The second requirement is the most difficult to achieve since it demands that reactants and products have all their electronic energy levels above the A-state or else, if there are levels at or below this level, they must be at least as metastable as $\text{N}_2(\text{A})$. At present we have not identified any likely candidates.

6. Extraction of Metastable $\text{N}_2(\text{A})$ from the Discharge Zone

$\text{N}_2(\text{A})$ formed in the e-beam sustained discharge region could be rapidly extracted from the discharge zone and formed into a supersonic molecular beam using the nozzle sampling arrangement shown schematically in Figure 37. The high throughput pump is used to generate a high flow speed in the discharge zone and to pump most of the mass flow. The nozzle then serves to sample the flow at a modest mass flow rate and form the molecular beam.

Our model calculations suggest that the lifetime of the $\text{N}_2(\text{A})$ states is of the order of 1 msec which means that the flow time from the discharge to the point A beyond the skimmer where the metastables will be used must also be of that order or less. For $L = 10 \text{ cm}$, a flow speed of 10^4 cm/sec (Mach number = 0.28 at 300°K) is required. Shock wave formation within the discharge zone can be reasonably ignored at this flow speed. Assuming that the discharge cross-sectional area is about 6 cm^2 , (comparable to the dimensions in the AERL small scale "minibang" e-beam sustained discharge device), the total mass flow rate is equal to 60 std. l/sec (127 std. cfm). Using this



J8763

Figure 37 Schematic Diagram of E-Beam Sustained Discharge Flow System for N_2 (A) Production

value and the equation of continuity, we can compute the area A^* , of the entrance hole to the high throughput pump from:⁽¹¹⁸⁾

$$A^* \rho_0 \left[\frac{\sqrt{RT_0}}{\sqrt{M}} \right] \sqrt{\gamma} \left[\frac{2}{(\gamma+1)} \right]^{(\gamma+1)/2(\gamma-1)} = 60 \text{ std. l/sec}$$

where ρ_0 is the number density at the stagnation pressure ($P_0 = 1 \text{ atm}$) and stagnation temperature ($T_0 = 298^\circ\text{K}$), M is the molecular weight of N_2 and $\gamma = C_p/C_v$ for $N_2 = 1.4$. Evaluating the above yields $A^* = 2.9 \text{ cm}^2$.

This result is in error by a few percent given that the stagnation pressure and temperature are about 5 percent higher than the values used above when the flow speed is Mach 0.28. The area of the sampling orifice, A_N , is then arbitrary and can be sized to match the appropriate pump displacement that evacuates the skimmer zone.

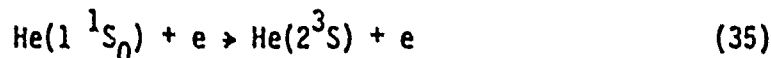
118. Hill, P.G. and Peterson, C.R., Mechanics and Thermodynamics of Propulsion, (Addison-Wesley, Reading, Mass., 1965) p. 47.

D. METASTABLE PRODUCTION FROM MAGNETIC ANNULAR ARC

Many atomic or molecular metastable production techniques rely on electron impact excitation processes to access metastable levels using either e-beams or electrical discharge sources. These methods usually require a high average electron energy in order to achieve efficient pumping. However, hot electrons can also be detrimental to the metastable production efficiency if ionization of the metastable can occur. For example, in helium, the 2^3S metastable level (~ 20 eV above the ground state) is within 5 eV of the ionization continuum. The cross section for the ionization process



is about two orders of magnitude larger than the cross section for the excitation process



at the electron energy which maximizes process (35). It is obvious, then, that metastable ionization can severely limit the ratio of metastable to ground-state densities. An alternative production method is described below which utilizes metastable formation from three-body atomic ion-electron recombination processes, which are most efficient at electron energies much below that required for metastable ionization.

We begin the discussion with a brief overview of the salient features of this method and then describe in more detail various aspects of the ionization source, electron cooling processes and the recombination processes.

The basic idea is to create a highly ionized plasma in which the electron temperature is initially high and the heavy particle temperature is low. The plasma is allowed to expand into a lower pressure stagnation region where the electrons cool via collisions with cold heavy ions and neutrals. If the electrons cool sufficiently (down to several tenths of an eV), volumetric three-body atomic ion-electron recombination of the type



will occur on a timescale fast compared to ion diffusion processes to the walls. In process (36) He^{**} represents any helium excited state. These highly excited neutrals will cascade down via a combination of radiative and collisional de-excitation processes eventually terminating in the low lying metastable states.

The plasma source is a magnetic annular arc (MAARC) also known as a plasma jet or magneto-plasma dynamic arc jet. This source is characterized by a high degree of ionization as calculated from the Saha equation:⁽¹¹⁹⁾

$$N_e = \left[N_a A \frac{g_+}{g_a} T_e^{3/2} e^{-I/kT_e} \right]^{1/2} \quad (37)$$

where

- N_e = electron number density (cm^{-3})
- N_a = ground-state atom density (cm^{-3})
- A = $6.04 \times 10^{21} \text{ cm}^{-3} - \text{eV}^{-3/2}$
- T_e = electron temperature ($^{\circ}\text{K}$)
- I = ionization potential (eV)
- g_+ = degeneracy of the ion state
- g_a = degeneracy of the atomic ground state

For example, 10 percent ionization in helium (I.P. = 24.5 eV) can be achieved with $T_e = 1.16 \text{ eV}$ for a helium density of 10^{15} cm^{-3} . However, it must be remembered that the Saha equation is applicable only for Boltzmann equilibrium distributions. The applicability of (37) to the present disequilibrium situation, in which a high electron temperature and low gas temperature are required, demands that: (1) the time scale for electron-electron equilibration, τ_{ee} , be short compared to the residence time in the arc region, and (2) the electron-ion equilibration time scale, τ_{ei} , be long compared to the residence time in the arc, i.e.,

119. Saha, M.N., Phil. Mag 40, 472 (1920).

$$\tau_{ee} = \frac{1}{N_e Q_{ee} \bar{c}_e} < \tau_{\text{FLOW}} \quad (38a)$$

$$\tau_{eI} = \frac{1}{N_e Q_{eI} \bar{c}_e} \frac{M_I}{m_e} > \tau_{\text{FLOW}} \quad (38b)$$

where

- Q_{ee} = the cross section for electron-electron scattering (cm^2)
- Q_{eI} = the cross section for electron-ion scattering (cm^2)
- \bar{c}_e = average electron speed; $1/2 m_e \bar{c}_e^2 = 3/2 kT_e$

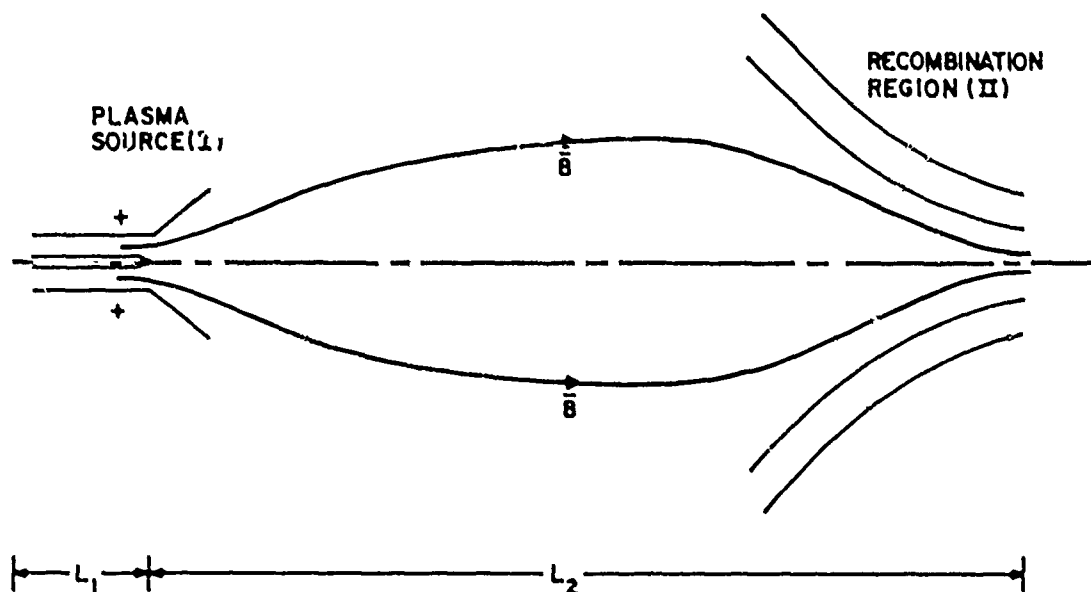
Eq. (38a) insures that there is a sufficient time to build up the high energy tail of the Boltzmann distribution which is the source of the ionization and, (38b) insures that ion heating by the electrons is slow. The cross sections, Q_{ee} and Q_{eI} can be obtained from the coulomb scattering formula:⁽¹²⁰⁾

$$Q_{ee} = Q_{eI} = \frac{4.4 \times 10^{-14} Z^4}{T_e^2} \ln \Lambda \approx \frac{4.4 \times 10^{-13}}{T_e^2} \text{ cm}^2 \quad (39)$$

for singly charged ions ($Z = 1$). Assuming $N_e = 10^{13} \text{ cm}^{-3}$ and $T_e = 1 \text{ eV}$ yields $\tau_{ee} = 4 \times 10^{-9} \text{ sec}$ and $\tau_{eI} = 3 \times 10^{-5} \text{ sec}$. Given the 10^5 cm/sec flow speed in the arc region implies that a flow dimension $L_1 < 3 \text{ cm}$ would be required to satisfy (38a) and (38b).

A schematic diagram of the source is displayed in Figure 38. The device consists of a coaxial pair of electrodes, the cathode in the center and an anode which can also serve as a nozzle. The electrons are heated in the arc region over a distance L_1 , and then are cooled as they traverse the distance L_2 . The B-field is used to stabilize the discharge and provide a means for

120. Spitzer, L., Physics of Fully Ionized Gases, 2nd Edition, Interscience Publishers (Wiley), New York, 1962.



K3718

Fig. Schematic Diagram of Electron-Ion Recombination Source

achieving a relatively large voltage in the plasma stream even when the plasma has a large conductivity. The criteria for achieving this impedance is to make $\omega_e \tau_e \geq 1$ where $\omega_e = eB/cm_e$ is the gyro frequency of the electrons and $\tau_e = 1/N_e Q_{eI} \bar{c}_e$ is the electron ion collision time for electrons which is appropriate for highly ionized plasmas. Note that τ_e is much smaller than the ion heating time, τ_{eI} . Since the magnetic field is aligned essentially parallel to the arc channel walls, and since the electrons undergo complete gyro orbits around the field lines between collisions, their mobility perpendicular to the field is reduced. The required B-field is then given by:

$$B \geq \frac{cm_e}{e} N_e Q_{eI} \bar{c}_e \quad (40)$$

For 1 eV average energy electrons in helium, $B \geq 14$ G at $N_e = 10^{13} \text{ cm}^{-3}$.

The MAARC operating voltage can be expressed by the following empirical formula:⁽¹²¹⁾

$$V = V_0 + U_c B \ell \quad (41)$$

where

V_0 = Electrode voltage drop ≈ 30 V for helium = constant.

$1/2 M_I U_c^2 = E_{\text{ionization}} \approx 25$ eV

B = Magnetic field strength (Gauss)

ℓ = radial separation between electrodes (cm)

The quantity, $1/2 M_I U_c^2$, is the ion kinetic energy set equal to the ionization energy. For helium, the value of U_c is equal to $\sim 5 \times 10^6$ cm/sec. Hence, the $U_c B \ell$ voltage drop ≈ 7.5 V when $B = 300$ G and $\ell = 1/2$ cm. The input power to the plasma is given by:

121. Patrick, R.M. and Schneiderman, A.M., Jour. AIAA 4, 283 (1966).

$$P_{iN} = N_0 V_0 E_{\text{particle}}$$

$$= (10^{15} \text{ cm}^{-3}) (10^5 \text{ cm/sec}) (1.6 \times 10^{-19} \frac{\text{J}}{\text{eV}}) (1 \text{ eV}) = 16 \text{ W}$$

The MAARC operating current, I , is given by

$$I = 16 \text{ W} / 7.5 \text{ V} = 2.1 \text{ amps}$$

The electrons will cool as they expand out of the arc (Region I) into the recombination zone (Region II). The main cooling processes are momentum transfer collisions to the cold ions, and, subsequently, the ions will lose their energy by symmetrical charge transfer reactions to the background neutrals. For efficient cooling, the time scales for electron-ion momentum transfer, τ_{ei} , and charge exchange τ_{cx} must be less than the flow time. We have previously shown that $\tau_{ei} \approx 3 \times 10^{-5} \text{ sec}$ and

$$\tau_{cx} = \frac{\lambda_{cx}}{c_I} = \frac{1}{N_{\text{He}} Q_{cx} \bar{c}} = \left[\left(\frac{1}{1 \times 10^{15} \text{ cm}^{-3}} \right) (10^{-15} \text{ cm}^2) \left(1 \times 10^5 \frac{\text{cm}}{\text{sec}} \right) \right]^{-1} \quad (42)$$

$$\approx 10 \text{ } \mu\text{sec}$$

Therefore, τ_{ei} and $\tau_{cx} < \tau_{\text{FLOW}}$ can be satisfied if the flow time is of the order of 100 μsec . This requires that for Region II $L_2 \approx 10 \text{ cm}$ in the flow dimension for a flow speed of 10^5 cm/sec .

Table 5 indicates the extent of "ideal" electron cooling assuming equipartition of the initial electron energy as calculated for several ionization levels. This is obviously only a lower limit to the true electron temperature in the recombination zone since the electrons can be heated up again using the energy liberated from the recombination processes which have been neglected in the calculations displayed here. The first column in Table 5 indicates the level of fraction ionization, the second column indicates the electron temperature, T_{ei} in the arc required by the Saha equation to reach this ionization level at the neutral density $N_a = 10^{15} \text{ cm}^{-3}$; the third column is the final electron temperature in the recombination zone obtained from

TABLE 5
EQUIPARTITION CALCULATION

N_{ei}/N_a	$T_{ei}(\text{eV})$	$T_{ef}(\text{eV})$	$\alpha(\text{cm}^6/\text{sec})$	N_{ei}	$\tau(\text{sec})$
1.0	1.45	0.725	2.3×10^{-11}	1×10^{15}	43×10^{-6}
0.5	1.35	0.47	8.4×10^{-11}	5×10^{14}	24×10^{-6}
0.1	1.16	0.13	5.4×10^{-9}	1×10^{14}	2×10^{-6}
0.01	0.96	~ 0.035	2×10^{-7}	1×10^{13}	0.5×10^{-6}

$$\frac{3}{2} N_e k T_{ei} + \frac{3}{2} N_a k T_a = \frac{3}{2} (N_e + N_a) k T_{ef} \quad (43)$$

where kT_a is the room temperature thermal energy of the ions and neutrals; the fourth column indicates the overall recombination rate constant at temperature T_{ef} using the Hinnoy-Hirschberg formula:⁽¹²²⁾

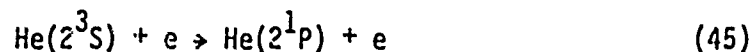
$$\alpha = 5.6 \times 10^{-27} T_e^{-9/2} N_{ei}$$

and the sixth column is the characteristic time for recombination at T_{ef} and the initial electron density N_{ei} (column 5). From the data in Table 5 it can be seen that the electrons will cool sufficiently such that the recombination time is always commensurate with or faster than the flow time (~ 100 μ sec). Therefore, it is possible to generate as much as 100 percent ionization in the arc and still cool the electrons sufficiently such that efficient volumetric recombination occurs.

The time evolution of the metastable neutral states generated from the recombination of atomic ions and electrons is a complicated dynamical process which depends critically on the competition between a number of processes. Although it is reasonable to expect that the ratio of singlet to triplet excited states will be $\sim 1/3$, the absolute fraction of metastable atoms cannot be estimated without extensive modeling. To amplify this point note that Table 5 indicates that the recombination time at high fractional ionization levels is commensurate with the electron cooling rates discussed previously. In addition both superelastic processes of the type



and spin exchange inelastic processes of the type



122. Hinnoy, E. and Hirschberg, J.G., Phys. Rev. 125, 795 (1962).

peak at low energies and thus compete with the desired recombination process. Process (44) destroys metastables directly and process (45) leads to metastable destruction via the optically allowed transition $\text{He}(2^1\text{P} \rightarrow 1^1\text{S})$.

Rather than perform the necessary modeling calculations, we have attempted to gain insight into metastable production yields using the experimental data of the Princeton stellarator group.⁽¹²³⁾ These experiments have investigated electron loss rates, electron cooling rates, electron and excited state densities in the afterglow of a highly ionized plasma produced by the pulsed stellarator source. The range of electron densities ($10^{11} \leq N_e \leq 3 \times 10^{13} \text{ cm}^{-3}$) and electron temperatures ($0.04 \text{ eV} \leq T_e \leq 1 \text{ eV}$) correspond to the conditions we expect in the MAARC generator. Although the main thrust of the Princeton work was involved with time resolved population densities in highly excited states (principal quantum number ≥ 5), some measurements for the $n = 2, 3$ and 4 levels have been obtained. These measurements indicate that although the highly excited states are in Boltzmann equilibrium at the electron temperature, the populations of the low lying states ($n = 2, 3$ and 4) are orders of magnitude below what would be expected based upon the Boltzmann factor for the high states. Using published results⁽¹²³⁾ we estimate a fractional metastable production $\sim 10^{-6} - 10^{-5}$ of the ground-state density for initial helium densities $1.5-3.0 \times 10^{13} \text{ cm}^{-3}$ and electron temperatures $\sim 0.2-0.4 \text{ eV}$.

In conclusion, it appears as though the metastable loss processes such as (44) and (45) are much faster than the processes which populate the metastable levels from the higher lying states, and that the dominant product from recombining atomic plasmas is the ground state of the atom.

123. Johnson, L.C. and Hinnov, E., Phys. Rev. 187, 143 (1969).

V. STORAGE OF METASTABLES

One can store metastables in a volume confined by material surfaces for a length of time which varies inversely with (a) the rate at which the metastables collide with the surfaces, and (b) the probability of deactivation on the surfaces. Since the latter is expected to decrease with decreasing temperature, one is led to consider storage in a cryogenic container.

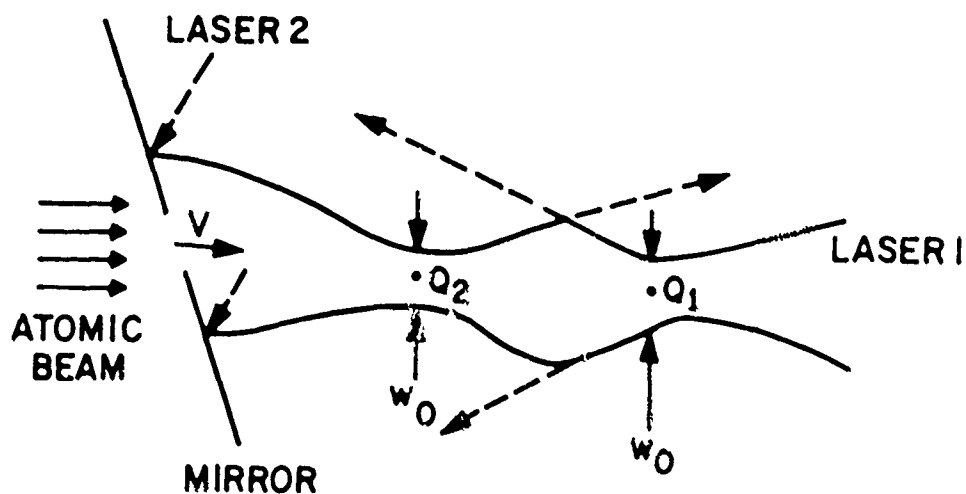
There is, however, another more speculative approach to this problem. Recently, several proposals for confining atoms and molecules with laser light have appeared in the literature.⁽¹²⁴⁻¹²⁶⁾ Ashkin, for example, estimates that 10^6 atoms/sec can be confined in a laser-beam trap of capacity $\sim 3 \times 10^7$ atoms; atoms whose velocities range between 0 and 3×10^4 cm/sec are captured in the trap.⁽¹²⁶⁾ Ashkin's trap consists of two counter-propagating TEM_{00} -mode laser beams focused to spot sizes of several μm (Figure 39). The focal spots are ~ 2 cm apart. As shown in Figure 40, a requirement is that the laser light be nearly resonant with an allowed transition of the atoms which are to be trapped.

Two mechanisms work together to confine atoms in the counter-propagating beam configuration shown in Figure 39. First, there is a net longitudinal force on an individual atom which tends to slow it down if $\omega < \omega_0$. This force may be understood from Figure 41. An atom is continuously absorbing laser light and emitting it spontaneously and isotropically. In the atomic rest frame, the light wave opposed to the atomic motion appears shifted up in frequency, while the other wave is shifted down in frequency. Since the opposing beam is thus shifted closer to the atomic resonance frequency ω_0 , an atom moving to the right absorbs more photons from it than from the co-propagating light wave and is slowed down by the net transfer of momentum. Similarly, an atom moving to the left would absorb more strongly from the right-going light wave, hence, it too would be slowed down.

124. Letokhov, V.S., Minogin, V.G. and Pavlik, D., Opt. Comm. 19, 72 (1976).

125. Letokhov, V.S. and Minogin, V.G., J. Opt. Soc. Am. 69, 413 (1978).

126. Ashkin, A., Phys. Rev. Lett. 40, 729 (1978).



K3747

Figure 39 Geometry of Ashkin's Optical Trap (Ref. 126). The atomic beam is injected into the interaction region through a hole in the mirror so that the atoms move along the propagation direction of the light. The focal point of the laser beam propagating to the left (right) is labeled Q_1 (Q_2). w_0 is the minimum spot size of the laser beams.

K3749

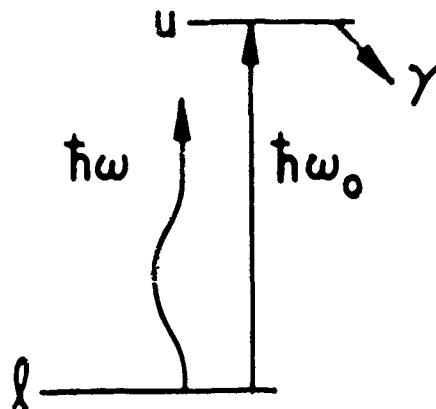
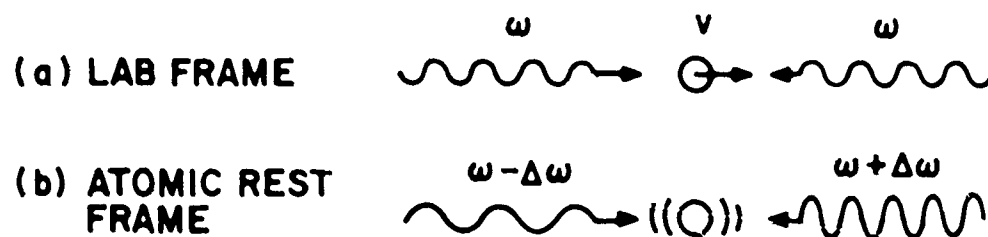


Figure 40

Energy Levels of an Atom Confined to an Optical Trap. The energy of the upper level u is $\hbar\omega_0$ higher than that of the lower level l . The upper level decays at the rate γ . The incident light has a frequency ω which is smaller than ω_0 by $\sim 50 \gamma$.

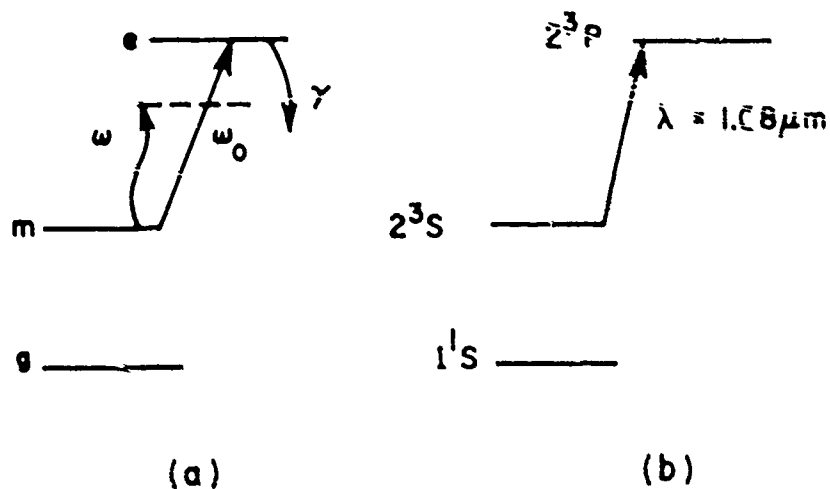


K3746

Figure 41 (a) An Atom moves to the Right at Velocity v along the Direction of Propagation of One of a Pair of Counter-Propagating Light Beams of Frequency ω .
 (b) Viewed in the Atomic Rest Frame, the Right-Going Beam Appears Downshifted, and the Left-Going Upshifted in Frequency.

The second mechanism, the ponderomotive force, confines the atom in the transverse direction, and may be understood as follows: the root-mean-square (rms) electric field of the light can exert an rms force on the atom in the same way as a static field. If the rms field is spatially uniform this force vanishes, but any nonuniform field polarizes an atom and therefore exerts a net "ponderomotive" force on the atom. It may be shown that for $\omega < \omega_0$ the sense of the force is the same as that due to a nonuniform static field, the atom being attracted to a region of higher intensity. Since the laser intensity is highest along the beam axis, the atoms are continuously attracted to this axis and the ponderomotive force exerts a stabilizing effect on the atomic confinement.

We believe that this technique may be generalized to the storage of certain metastable-state atoms and molecules. The basic idea behind such storage is that the laser should be tuned to a frequency ω slightly below the frequency ω_0 of an allowed transition between the metastable state m and an excited state e (Figure 42a). Metastable-state atoms injected into the optical trap are confined, while those atoms in other states, such as the ground state g , pass through the trap without interacting appreciably with the light. The trap thus acts as an atomic filter which confines only those atoms which are in the metastable state. A possible candidate species for such confinement is atomic He in the 2^3S state (Figure 42b), which would require a laser nearly resonant with either the $1.08\text{-}\mu\text{m}$ $2^3S\text{-}2^3P$ or the $0.389\text{-}\mu\text{m}$ $2^3S\text{-}3^3P$ transition. From the work of Ashkin,⁽¹²⁶⁾ we estimate that the required laser intensity would be $\sim 1\text{ W/cm}^2$ and the required minimum laser beam spot size $\sim 10\text{ }\mu\text{m}$. A beam of 2^3S He, for example, might require a quasi-CW laser nearly resonant with either the $1.08\text{-}\mu\text{m}$ $2^3S\text{-}2^3P$ or the $0.389\text{-}\mu\text{m}$ $2^3S\text{-}3^3P$ transition.



K3748

Figure 42 (a) Energy Levels of an Atom of Interest, Showing the Ground State g , Metastable State m , and Excited State e .
 (b) Energy Levels of He Corresponding to Those of (a).